ULTRASTRUCTURAL STUDIES OF TWO MODEL MINIMAL CELLS BY ELECTRON CRYOTOMOGRAPHY

Thesis by

Gregory P. Henderson

In Partial Fulfillment of the Requirements

for the Degree of

Doctor of Philosophy

California Institute of Technology

Pasadena, California

2007

(Defended May 2, 2007)

Acknowledgements

I would like to thank my advisor, Grant Jensen. Without his personal and professional guidance for the past five years, none of this would have been possible. I had the privilege of watching the laboratory grow from an empty floor in a new building, to a large thriving laboratory. Through it all Grant remained dedicated to being available, and providing constant encouragement.

I am indebted to my collaborators, especially Duncan Krause from the University of Georgia, Hervé Moreau from the Observatoire Océanologique, Laboratoire Arago, and Brian Palenik from Scripps Institution of Oceanography, UCSD.

I am grateful for my laboratory members. They have always been open with their advice and their friendship. I am most fortunate to have worked closely with Bingni Wen and Lu Gan.

I appreciate the time and feedback given to me by my committee: Pamela Björkman, Scott Fraser, Jared Leadbetter, and Douglas Rees.

I would also like to thank the USC/Caltech MD/PhD programs. Sandra Mosteller and Liz Ayala made sure everything ran smoothly, allowing me to focus on my education.

Abstract

While most motile bacteria propel themselves with flagella, other mechanisms have been described including retraction of surface-attached pili, secretion of polysaccharides, or movement of motors along surface protein tracks. These have been referred to collectively as forms of "gliding" motility. Despite being simultaneously one of the smallest and simplest of all known cells, *Mycoplasma pneumoniae* builds a surprisingly large and complex cell extension known as the attachment organelle that enables it to glide. Here, three-dimensional images of the attachment organelle were produced with unprecedented clarity and authenticity using state-of-the-art electron cryotomography. The attachment organelle was seen to contain a multi-subunit, jointed, dynamic motor much larger than a flagellar basal body and comparable in complexity. A new model for its function is proposed wherein inchworm-like conformational changes of its electron-dense core are leveraged against a cytoplasmic anchor and transmitted to the surface through layered adhesion proteins.

The hallmark of eukaryotic cells is their segregation of key biological functions into discrete, membrane-bound organelles. Creating accurate models of their ultrastructural complexity has been difficult in part because of the limited resolution of light microscopy and the artifact-prone nature of conventional electron microscopy. Here we explored the potential of the emerging technology electron cryotomography to produce three-dimensional images of an entire eukaryotic cell in a near-native state. *Ostreococcus tauri* was chosen as the specimen because as a unicellular picoplankton with just one copy of each organelle, it is the smallest known eukaryote and was therefore likely to yield the highest resolution images. Whole cells were imaged at various stages of the cell cycle, yielding 3-D reconstructions of complete chloroplasts, mitochondria, endoplasmic reticula, Golgi

bodies, peroxisomes, microtubules, and putative ribosome distributions *in-situ*. Surprisingly, the nucleus was seen to open long before mitosis, and while one microtubule (or two in some predivisional cells) were consistently present, no mitotic spindle was ever observed, prompting speculation that a single microtubule might be sufficient to segregate multiple chromosomes.

Table of Contents

List of Tables and Figures

Chapter 1: Introduction

Minimal Cells

Cell biology, genomics, and proteomics have flooded us with a "parts list" for cells. Genetic, structural, and biochemical studies may tell us what each part does, but rarely do these parts act in isolation. Their distribution in a cell is often non-random. Many organize into large complexes or form into complex organelles. Fully understanding and modeling the final product, a living cell, requires knowledge of how all the parts fit together. While EM is not a new technique, recent advances have given new life to the field. Improved instrumentation, automation, and sample preservation allow for the three-dimensional (3D) reconstruction of whole cells trapped in frozen-hydrated life-like states.

Understanding multi-component systems is difficult and this drives the search for model systems where the complexity is reduced while maintaining the features of interest. In this light "minimal cells," with a shrunken cell size and genome, offer obvious appeal. The parasitic bacteria *Mycoplasma pneumoniae* has one of the smallest known genomes, but preserves features of importance, including cell polarity and motility. *Ostreococcus tauri* is the smallest free-living eukaryotic known, but still contains a single copy of each major organelle, including the chloroplast. These two minimal cells were used as models to explore prokaryotic and eukaryotic ultrastructure.

Electron Microscopy and Sample Preservation

An intuitive understanding of spatial systems is best developed visually. New means to visualize biology have lead to great advances in cell biology. Four hundred years ago Anton van Leeuwenhoek invented the light microscope, and so began cell biology. Over three hundred years later, in 1931, Max Knott and Ernst Ruska invented the electron microscope. By the 1940s, EM was being used to visualize cells (Porter and Yegian, 1945). Today most of our cell ultrastructural knowledge comes from EM.

The study of cell ultrastructure and macromolecular protein complexes is heavily indebted to transmission EM, one of the few techniques that can visualize details at the 3-7 nm range. Despite its crucial importance, electrons are in many ways non-ideal for imaging biological samples. Even modest doses rapidly destroy biological material. Using a limited dose results in loss of contrast between the biological molecules and the surrounding water. In addition, for adequate electron beam penetration of the sample, without excessive inelastic scattering of the electrons, samples must be kept as thin as possible.

To overcome the dose and contrast limitations, traditional EM does not directly image the biological sample, but relies on heavy metal staining to surround molecules of interest. Samples are chemically fixed and dehydrated, allowing for the water to be replaced with a plastic resin. Samples are then sectioned and stained with heavy metals (osmium, lead, and uranium). These preparation techniques lead to alterations of the native cell ultrastructure. Sample preservation can be improved by carrying them out at low temperatures, a technique known as high-pressure freezing and freeze substitution (McDonald and Auer, 2006). By rapidly freezing the sample and not warming the sample until after it has been fixed and

embedded in resin, the cell ultrastructure has less ability to change. This leads to substantially improved membrane and protein structure.

For the investigation of biological specimens, the electron dose is the main limiting factor. Improvements in imaging, computers, and robot technology in the last two decades resulted in electron microscopes that can be automated and controlled by computers. These systems help minimize unnecessary electron beam exposure to the sample. By practically eliminating the overhead dose the sample receives, the entire dose can be used for image capture. A second major discovery was that biological samples tolerate the radiation damage from the electron beam up to an order of magnitude better at liquid nitrogen temperatures compared to room temperature (Fujiyoshi, 1998; Glaeser, 1971). Thus significantly higher doses can be used. Imaging of frozen samples can now produce a high enough signal-to-noise ratio that useful data can be recorded from the native biological structure. Today, cells can be rapidly immobilized in a frozen-hydrated, life-like state with minimal preservation artifact. Automated, climate-controlled environments, such as the Vitrobot have greatly facilitated this process (Appendix A).

Sample thickness is a second critical problem for transmission EM. Each individual image is a 2-D projection of the sample making it impossible to determine its 3-D. Tomography solves this problem. Multiple 2D projections of the same sample are taken as the specimen is incrementally rotated. A computer then recombines the images using a weighted back projection algorithm to construct a 3D model of the sample (Lucic et al., 2005a; Radermacher et al., 1992). 200–700 nm thick samples are commonly used in tomography, but for samples greater than 500 nm the resolution begins to worsen rapidly. Sample thickness is still narrow, but the new limiting factor is the electrons penetrating the

sample. Most modern tomography EMs have 300 keV accelerating voltages. This voltage will accelerate the electrons up to approximately 80% the speed of light. At lower voltages, electrons cannot adequately penetrate the sample. Using higher voltages, electrons have limited interaction with the sample and detectors have difficulty localizing the electrons. New detectors are being developed to decrease noise and allow for thicker samples to be imaged (Milazzo et al., 2005; Yonekura et al., 2006).

Cellular electron cryotomography (ECT) has combined the advantages of tomography with frozen-hydrated samples to create 3D life-like snapshots of the cells. Perhaps the most profound proof of concept for the advantages of ECT compared to conventional EM has been its ability to prove the existence of prokaryotic cytoskeletons *in vivo* (Briegel et al., 2006; Henderson and Jensen, 2006; Komeili et al., 2006; Kurner et al., 2005; Scheffel et al., 2006), something previous EM techniques have not generally been able to do with confidence. These earlier limitations had lead to the mistaken belief that these filaments were absent in bacteria. ECT has also been successfully used to reveal startling new details of macromolecular machines, including two motors used for cell motility: the bacterial flagella motor (Murphy et al., 2006), and the motor complex of *M. pneumoniae*'s attachment organelle (Chapter 2) (Henderson and Jensen, 2006). ECT is more challenging in eukaryotes. Cell size, typically far greater than one micrometer, precludes most cells from being imaged whole. Thin cellular extensions such as the leading edge of a Dictyostelium cell (Medalia et al., 2002b), the eukaryotic flagella (Nicastro et al., 2006; Sui and Downing, 2006), and nerve processes (Garvalov et al., 2006) are thin enough to be imaged. Progress is still limited on sectioning frozen-hydrated samples for ECT (Hsieh et al., 2006). To date, there are no publications on whole cell tomography of frozen-hydrated eukaryotic cells

(Chapter 3). Most tomography in eukaryotes has focused on samples that have been high-pressure frozen, embedded, and sectioned.

Mycoplasmas and the Attachment Organelle

Despite decades of ultrastructural studies on bacteria, many fundamental questions remain unanswered: How do cells maintain their shape and polarity? What roles do the cytoskeletons play? How is the genome organized and segregated? And how do different types of bacteria move? With only 700 genes, *M. pneumoniae* has but one-sixth the genes of *Escherichia coli* and is nearly 25 times smaller in volume. Nonetheless, it can be used to try to answer each of the questions above.

M. pneumoniae is the leading cause of pneumonia in older children and young adults. Mycoplasmas are characteristic in their lack of a peptidoglycan cell wall; thus *M. pneumoniae* can be pleomorphic. When moving over a surface, it will orient itself along a line with a leading head, an ellipsoid body, and a long trailing tail. The cell's most remarkable structure is its leading head, the attachment organelle. The attachment organelle mediates adhesion of the cell to a surface, and has now been shown to also mediate motility (Hasselbring and Krause, 2007), something suspected but not proven at the time of my publication. Prior to the observations by ECT (Chapter 2) the attachment organelle was known to be a membrane-bound cell extension coated by surface adhesion proteins. Internally, there is a large protein core known as the electron-dense core. The core was identified by the first EM studies, but traditional EM could do no more than resolve the core as two rods that were assumed to be identical (Hegermann et al., 2002b). Models assumed

the core was homogenous, perhaps made of one or two proteins. The core's role was assumed to be to organize the surface proteins that would mediate cell adhesion and motility. Such models were reasonable because another well-studied mobile mycoplasma, *M. mobile*, appeared to rely on its surface proteins for adhesion and motility, though these proteins lacked homologs in *M. pneumoniae*. Further research has now shown that most of the proteins involved in motility in *M. pneumoniae* are also not found in *M. mobile* (Hasselbring and Krause, 2007).

The electron-dense core is part of what has been called *M. pneumoniae*'s "cytoskeleton." Washing eukaryotic cells in a non-ionic detergent, such as Triton X-100, leaves behind the cells' cytoskeletons. By the same criteria, *M. pneumoniae* has a cytoskeleton that roughly adopts the shape of the cell body. More specifically, 5-nm filaments have been demonstrated within the cell body, sometimes associated with the proximal end of the attachment organelle (Hegermann et al., 2002b; Meng and Pfister, 1980). These filaments were demonstrated long before the more recent evidence of filaments in many other bacteria. Importantly, traditional candidate genes for cytoskeletal proteins have not been found in *M. pneumoniae* (Himmelreich et al., 1996; Regula et al., 2001). Along with the cytoskeleton, the attachment organelle itself may play a role in maintaining cell shape. Knocking out the proteins that localize to the attachment organelle leads to abnormally shaped cells (Krause and Balish, 2004).

The role of the attachment organelle in cell division is a rapidly evolving story. By 2001 it was believed that the replication of the attachment organelle preceded cell division (Seto et al., 2001). This coordination occurs despite a lack of common transcriptional regulators in M. pneumoniae (Himmelreich et al., 1996). Based upon fluorescently labeled

attachment organelle proteins and cellular DNA from fixed cells, a model was proposed. New attachment organelles were thought to form near the original one. The newly formed attachment organelle then migrated to the opposite end of the cell as the genome replicated. Once the attachment organelle reached the other side of the cell, the cell divided (Seto et al., 2001). Many structural questions can be asked about these steps: (1) Did the attachment organelle replicate by a semi-conserved splitting of the electron-dense core, or was the attachment organelle synthesized *de novo*? (2) Was there a cytoskeletal path that the new attachment organelle migrated along to reach the opposite side of the cell? (3) How were these processes coordinated with genome replication and division? Was the genome somehow physically connected to the attachment organelle?

With my publication and other subsequent publications (a combination of ECT (Chapter 2) (Henderson and Jensen, 2006; Seybert et al., 2006) and time-lapse light microscopy (Hasselbring et al., 2006a)), an answer has started to evolve. (1) New evidence now suggests that the attachment organelle forms *de novo*. First, attachment organelles form *de novo* in knockout mutants that lack an attachment organelle but subsequently form them when the missing genes are reintroduced (Krause and Balish, 2004). Second, ECT shows the two halves of the electron-dense core are non-identical. Finally, observations of fluorescently labeled proteins being added to new attachment organelles suggest *de novo* synthesis (Hasselbring *et al*., 2006a). (2) Once two attachment organelles form, they separate. ECT fails to find any structural connection between adjacent attachment organelles. Time lapse microscopy shows the original attachment organelle begins to move, pulling the cell body away from the newly formed attachment organelle, which remains non-motile and attached to the surface during the process (Hasselbring et al., 2006a). (3) No

physical connection is seen by ECT between the attachment organelle and the genome. However, the genome is notoriously difficult to visualize by EM in bacteria. That said, light microscopic data shows that most cells actually produce multiple (> 2) attachment organelles before cytokinesis, which questions a direct link between attachment organelle replication and genome replication.

Many bacteria move, but the mechanism of *M. pneumoniae*'s motility appears to be exclusive to just a small number of closely related species (*M. pneumoniae*, *M. genitalium*, and *M. gallisepticum*) (Clyde and Hu, 1986). No homologs for other bacterial motility genes have been found in *M. pneumoniae* (Himmelreich *et al*., 1996). Therefore to identify the involved proteins, screens have been set up to find mutants with cytadherence defects, and, more recently, motility defects. At this point, the role of most of the discovered proteins remains unknown.

The work prior to my publication was based upon cytadhesion mutants. Two general defects were recognized: 1) loss of adhesion surface proteins, and 2) failure to localize the adhesion proteins to the attachment organelle. The two major surface adhesion proteins are P1 and P30. Antibodies to either will block cytadherence. Similarly, loss of either protein leads to non-adherent cells, but does not affect the localization of the other adhesion molecule. P1 is believed to localize over the entire attachment organelle, while P30 is believed to localize more to the distal end (Seto and Miyata, 2003).

Three other surface proteins are B, C, and P65. P1 co-localized with proteins B and C, which are cleaved from a common 130 kDa precursor protein that is cotranscribed with P1. In *M. genitalium* and *M. gallisepticum*, the homologous precursor protein is not cleaved.

There is evidence that this precursor protein shares low-level sequence similarity to P1 and may adopt a similar conformation (Papazisi et al., 2000). Loss of protein B and C results in a failure to localize P1 and loss of cytadherence (Baseman et al., 1982). P30 co-localized with P65 but the role of P65 is unknown (Jordan et al., 2001; Seto et al., 2001; Seto and Miyata, 2003).

Failure to localize the adhesion proteins often results from abnormalities in the electron-dense core. Cells lacking either of two large proteins, HMW1 or HMW2, do not construct an electron-dense core. A third protein characterized by core defects is HMW3. Earlier EM findings showed that cells lacking HMW3 occasionally have attachment organelles where the core looks split like a "V," with the vertex pointing away from the cell body. These earlier observations of the split core and the mistaken belief that the two halves of the core were identical lead to a hypothesis that HMW3 held the two halves of the core together and loss of HMW3 lead to splitting of the core. These observations also generated a hypothesis about how the attachment organelle could replicate by dividing its core into two equal parts. More recent observations with ECT suggest that in cells lacking HMW3 the two halves of a single core do not in fact split, but instead two cores occupy the same attachment organelle (personal observation).

Work published since my paper has brought forth a new set of at least 30 proteins that affect motility (Hasselbring et al., 2006b). Many of these have no known function. Some are involved in processes like metabolism and may have only secondary effects on motility. The most startling finding was for the protein P41. Cells lacking P41 still developed the attachment organelle and could move and adhere to surfaces. Amazingly, the attachment organelle would sometimes separate from the cell body and continue moving on its own.

This conclusively demonstrated that the attachment organelle contained the motor for cell motility (Hasselbring and Krause, 2007).

While ECT of wild type *M. pneumoniae* was an important and necessary first step, a much fuller picture of the attachment organelle's structure and function will be achieved by future ECT studies of the attachment organelle and the cytadherence and motility mutants. These studies promise to localize precisely some of the proteins of the attachment organelle and to facilitate the understanding of their functions in this unique form of motility.

Eukaryote Ultrastructure

ECT has helped to show that bacteria are not "bags" of free-floating enzymes; even the simplest cells such as *M. pneumoniae* use multiple means to organize themselves. This truth is all the more evident in eukaryotic cells, where people have long appreciated the fact that the cells contain multiple organelles and a complex cytoskeleton. Knowing this is different from understanding its implications. Current techniques have seriously hampered our ability to effectively map eukaryote ultrastructure in whole cells. Classical light microscopy, for all its advantages of being able to image live cells in 3-D, is limited to ca. 200 nm resolution and 40 nm resolution for fluorescently labeled molecules (Willig et al., 2006). Shorter wavelength X-ray tomography has the promise of sub-15 nm resolution (Chao et al., 2005) but published results are of 40 nm or higher (Larabell and Le Gros, 2004; Le Gros et al., 2005). Traditional thin-sectioned EM has sufficient resolution but effectively gives only two-dimensional information. Electron tomography alone combines high resolution with 3D data. Unfortunately, it is restricted to samples less than 1000 nm thick.

To overcome this disadvantage, either thin samples must be used or thicker samples must be sectioned.

Serial sections must be done on fixed samples using current techniques. Fixed EM samples, though, have the serious disadvantage in that they undergo major shrinkage when they are under the electron beam. Samples will typically shrink 40 to 50% in the direction of the beam and 5 to 10% in the perpendicular direction (Lucic et al., 2005a); it is not clear if this shrinkage occurs uniformly or not. ECT using frozen-hydrated samples avoids this shrinkage as well as staining artifacts. But again it is severely restricted by sample thickness; serial sectioning for frozen-hydrated samples remains unavailable. Because *O. tauri* is so small, it is the only eukaryotic cell known that can be imaged whole by ECT throughout its entire life cycle. *O. tauri* is thus a powerful model for the study of whole eukaryote cell ultrastructure.

Other examples of whole cell tomography are very limited. X-ray tomography has been used to generate 60 nm resolution tomograms of frozen-hydrated *Saccharomyces cerevisiae* (Larabell and Le Gros, 2004). The cells were 5 μm in diameter, far thicker than can be imaged by electron tomography. In addition, multiple cells could be imaged rapidly to provide better statistics. However at 60 nm resolution, structures like the endoplasmic reticulum and the mitochondria could not be differentiated. Higher resolution EM tomograms of whole cells using serial sections is a feat that has rarely been done. In March of this year, a paper appeared on serially sectioned embedded fission yeast, *Schizosaccharomyces pombe* (Hoog et al., 2007). Though the paper focused on interphase microtubules, they reported that one of the cells had been completely reconstructed by combining multiple 250 nm sections. Gathering data from serial sections is time intensive.

Having only one or two reconstructions of cells significantly limits our knowledge of whole cell ultrastructure. Not only do individual cells vary, but also the ultrastructure varies in response to the environment (Mannella, 2006a, b) and cell cycle (discussed in Chapter 3).

Generally, tomography of eukaryotes has been limited to individual organelles or sections through cells. These works have provided important functional insight into organelles and sub-organellar structure such as the mitochondrion (Mannella, 2006a; Nicastro et al., 2000), chloroplast (Shimoni et al., 2005), nucleus-embedded nuclear pore complex (Beck et al., 2004), and the cytoskeleton (Hoog et al., 2007; Medalia et al., 2002a). In contrast, organelles such as the endoplasmic reticulum and Golgi body (Ladinsky et al., 1999; Storrie and Nilsson, 2002) have only been studied piecemeal by EM because they cannot be readily purified and are extremely large.

For a detailed look at the role of EM in the study of sub-cellular structure, the example of the mitochondria is illustrative. The earliest EM images of mitochondria were thin-sectioned. These erroneously gave rise to a "baffle model" in which the inner membrane of the mitochondria was assumed to fold inward like the baffles of an accordion into wide-open compartments. As technology improved, electron tomography was used on thick sections cut from high-pressure frozen and embedded sections. These showed the cristae to be connected to the inner membrane through narrow junctions, not wide-open enfoldings. The cristae shapes were pleomorphic, varying from tubular to lamellar depending on the environment the mitochondria were in (Frey and Mannella, 2000). This led to new models of the cristae as being local environments connected to the inter-membrane space through junctions that limited diffusion. Still, the use of chemical fixation resulted in the inner and outer membrane looking rough and uneven. It was not until ECT was used on

isolated mitochondria that the inner and outer membranes were shown to be smooth and parallel. Additional features were found including wider crista junctions and new interconnections between the cristae (Nicastro et al., 2000). Since effects like widening of the crista junctions are thought to occur in apoptosis (Scorrano et al., 2002), it remains unclear whether the ECT observations were physiological or an artifact of isolating the mitochondria from the cells.

An *in vivo* model of frozen-hydrated mitochondria would eliminate any artifacts from organelle isolation. It would also open the door to ask new questions through tomography. One could probe whether the mitochondria had any set positional relations to other organelles and what were the underlying structural bases for these relations. One could also observe how these relations changed during the cell cycle. The cell cycle is often discussed in terms of the changes the nucleus and the genome undergo, but every organelle must replicate and partition itself during cell division. This process cannot easily be observed at the ultrastructural level with current techniques.

Electron tomography of eukaryotes is a challenging field, but modeling cellular physiology and pathophysiology relies on ultrastructural details. Improvements in techniques will drive this area. Cryosectioning (Hsieh et al., 2006) and focused ion beam milling (Marko et al., 2006) may one day make routine the imaging of frozen-hydrated sections of cells and tissues. *O. tauri* will continue to play a key role though because of its simple cellular organization and its ability to be imaged whole. *O. tauri* is becoming a well-developed system for the analysis of the cell cycle and will hopefully be amenable for future genetic manipulation. These two properties of *O. tauri* will enable systematic high-

resolution ultrastructural analyses of a *bona fide* eukaryote in fundamentally important cellular states.

Personal Contributions

I joined Dr. Jensen's laboratory at its very beginning and began working on mycoplasmas and *O. tauri*. Chapter 2 summarizes my work with ECT on *M. pneumoniae*. I was the sole student responsible for this work. The project evolved out of an effort to characterize *M. genitalium*, at the time the smallest and simplest known cell. I decided to focus on the attachment organelle and proposed to switch to *M. pneumoniae* where more work had been done. I arranged to attend a conference in Athens, Georgia, where I was able to establish collaborations with Dr. Krause and arranged to obtain samples of *M. pneumoniae*. Since then I have secured other *M. pneumoniae* mutants to work with. I learned how to culture them and prepare samples. I set up the necessary bio-safety level two precautions with the help of Dr. Dias. I prepared all samples. Data was taken by either myself or with the assistance of Dr. Tivol. I did all the reconstruction and segmentation. I drafted the paper and all figures. Dr. Jensen revised the paper. I submitted the paper and helped craft replies to the reviewers' comments. I also created the cover figure for that issue of *Molecular Microbiology*. I have traveled to three meetings to present this work, including giving an oral presentation at the 16th International Congress of the International Organization for Mycoplasmology in England. Under Dr. Jensen's supervision, I peer-reviewed a paper from another laboratory on *M. pneumoniae*'s attachment organelle and reviewed a grant proposal on mycoplasmas for the NIH.

Chapter 3 summarizes my work on whole cell tomography of *O. tauri* throughout its cell cycle. I began working on this project at the onset of joining the lab. I learned how to optimally grow and work with the cells and visited the laboratories of Dr. Moreau (France) and Dr. Palenik (San Diego) to work with *O. tauri* and *O. lucimarinus* respectively. I worked with flow cytometry to try to select the smallest cells possible. I learned conventional EM fixation and sectioning at the Caltech transmission electron microscopy facility and I traveled to Berkeley with Dr. Jensen to perform high-pressure freezing with Dr. McDonald. Undergraduate Bingni Wen worked under my guidance in a project to attempt to isolate organelles from *O. tauri*. Most of the ECT data was collected one year ago, at which time I began working with a new post-doc, Dr. Lu Gan. Dr. Gan helped culture the cells and imaged the cells by light microscopy. I prepared most of the ECT samples and collected most of the data on the EM. Dr. Gan helped with the reconstruction of the data. I prepared data for Dr. Jane Ding to run the necessary programs on the Caltech supercomputer to search *O. tauri* for ribosomes by template matching. I wrote the majority of the paper, though Dr. Gan wrote the section on the nuclear pore complex and a portion of the section on the chloroplast. He created figures two and seven while I prepared the other figures and the movie. Dr. Gan also revised the paper multiple times. The final paper was revised by Dr. Jensen, and will be submitted to *PLoS Biology*.

Appendix A is a protocol paper written by Dr. Iancu. I along with many other laboratory members contributed our experiences in using the Vitrobot (FEI) for frozen-hydrated sample preparation. I also helped revise the paper.

References

Baseman, J.B., Cole, R.M., Krause, D.C., and Leith, D.K. (1982) Molecular basis for cytadsorption of *Mycoplasma pneumoniae*. *J Bacteriol* 151: 1514-1552.

Beck, M., Forster, F., Ecke, M., Plitzko, J.M., Melchior, F., Gerisch, G., Baumeister, W., and Medalia, O. (2004) Nuclear pore complex structure and dynamics revealed by cryoelectron tomography. *Science* 306: 1387-1390.

Briegel, A., Dias, D.P., Li, Z., Jensen, R.B., Frangakis, A.S., and Jensen, G.J. (2006) Multiple large filament bundles observed in Caulobacter crescentus by electron cryotomography. *Mol Microbiol* 62: 5-14.

Chao, W., Harteneck, B.D., Liddle, J.A., Anderson, E.H., and Attwood, D.T. (2005) Soft X-ray microscopy at a spatial resolution better than 15 nm. *Nature* 435: 1210-1213.

Clyde, W.A., Jr., and Hu, P.C. (1986) Antigenic determinants of the attachment protein of Mycoplasma pneumoniae shared by other pathogenic Mycoplasma species. *Infect Immun* 51: 690-692.

Frey, T.G., and Mannella, C.A. (2000) The internal structure of mitochondria. *Trends Biochem Sci* 25: 319-324.

Fujiyoshi, Y. (1998) The structural study of membrane proteins by electron crystallography. *Adv Biophys* 35: 25-80.

Garvalov, B.K., Zuber, B., Bouchet-Marquis, C., Kudryashev, M., Gruska, M., Beck, M., Leis, A., Frischknecht, F., Bradke, F., Baumeister, W., Dubochet, J., and Cyrklaff, M. (2006) Luminal particles within cellular microtubules. *J Cell Biol* 174: 759-765.

Glaeser, R.M. (1971) Limitations to significant information in biological electron microscopy as a result of radiation damage. *J Ultrastruct Res* 36: 466-482.

Hasselbring, B.M., Jordan, J.L., Krause, R.W., and Krause, D.C. (2006a) Terminal organelle development in the cell wall-less bacterium Mycoplasma pneumoniae. *Proc Natl Acad Sci U S A* 103: 16478-16483.

Hasselbring, B.M., Page, C.A., Sheppard, E.S., and Krause, D.C. (2006b) Transposon mutagenesis identifies genes associated with Mycoplasma pneumoniae gliding motility. *J Bacteriol* 188: 6335-6345.

Hasselbring, B.M., and Krause, D.C. (2007) Cytoskeletal protein P41 is required to anchor the terminal organelle of the wall-less prokaryote Mycoplasma pneumoniae. *Mol Microbiol* 63: 44-53.

Hegermann, J., Herrmann, R., and Mayer, F. (2002) Cytoskeletal elements in the bacterium Mycoplasma pneumoniae. *Naturwissenschaften* 89: 453-458.

Henderson, G.P., and Jensen, G.J. (2006) Three-dimensional structure of Mycoplasma pneumoniae's attachment organelle and a model for its role in gliding motility. *Mol Microbiol* 60: 376-385.

Himmelreich, R., Hilbert, H., Plagens, H., Pirkl, E., Li, B.C., and Herrmann, R. (1996) Complete sequence analysis of the genome of the bacterium *Mycoplasma pneumoniae*. *Nucleic Acids Res.* 24: 4420.

Hoog, J.L., Schwartz, C., Noon, A.T., O'Toole, E.T., Mastronarde, D.N., McIntosh, J.R., and Antony, C. (2007) Organization of interphase microtubules in fission yeast analyzed by electron tomography. *Dev Cell* 12: 349-361.

Hsieh, C.E., Leith, A., Mannella, C.A., Frank, J., and Marko, M. (2006) Towards high-resolution three-dimensional imaging of native mammalian tissue: electron tomography of frozen-hydrated rat liver sections. *J Struct Biol* 153: 1-13.

Jordan, J.L., Berry, K.M., Balish, M.F., and Krause, D.C. (2001) Stability and Subcellular Localization of Cytadherence-Associated Protein P65 in *Mycoplasma pneumoniae*. *J Bacteriol* 183: 7387-7391.

Komeili, A., Li, Z., Newman, D.K., and Jensen, G.J. (2006) Magnetosomes are cell membrane invaginations organized by the actin-like protein MamK. *Science* 311: 242-245.

Krause, D.C., and Balish, M.F. (2004) Cellular engineering in a minimal microbe: structure and assembly of the terminal organelle of *Mycoplasma pneumoniae*. *Mol Microbiol* 51: 917-924.

Kurner, J., Frangakis, A.S., and Baumeister, W. (2005) Cryo-electron tomography reveals the cytoskeletal structure of Spiroplasma melliferum. *Science* 307: 436-438.

Ladinsky, M.S., Mastronarde, D.N., McIntosh, J.R., Howell, K.E., and Staehelin, L.A. (1999) Golgi structure in three dimensions: functional insights from the normal rat kidney cell. *J Cell Biol* 144: 1135-1149.

Larabell, C.A., and Le Gros, M.A. (2004) X-ray tomography generates 3-D reconstructions of the yeast, saccharomyces cerevisiae, at 60-nm resolution. *Mol Biol Cell* 15: 957-962.

Le Gros, M.A., McDermott, G., and Larabell, C.A. (2005) X-ray tomography of whole cells. *Curr Opin Struct Biol* 15: 593-600.

Lucic, V., Forster, F., and Baumeister, W. (2005) Structural studies by electron tomography: from cells to molecules. *Annu Rev Biochem* 74: 833-865.

Mannella, C.A. (2006a) Structure and dynamics of the mitochondrial inner membrane cristae. *Biochim Biophys Acta* 1763: 542-548.

Mannella, C.A. (2006b) The relevance of mitochondrial membrane topology to mitochondrial function. *Biochim Biophys Acta* 1762: 140-147.

Marko, M., Hsieh, C., Moberlychan, W., Mannella, C.A., and Frank, J. (2006) Focused ion beam milling of vitreous water: prospects for an alternative to cryo-ultramicrotomy of frozen-hydrated biological samples. *J Microsc* 222: 42-47.

McDonald, K.L., and Auer, M. (2006) High-pressure freezing, cellular tomography, and structural cell biology. *Biotechniques* 41: 137, 139, 141 passim.

Medalia, O., Weber, I., Frangakis, A.S., Nicastro, D., Gerisch, G., and Baumeister, W. (2002a) Macromolecular architecture in eukaryotic cells visualized by cryoelectron tomography. *Science* 298: 1209-1213.

Medalia, O., Weber, I., Frangakis, A.S., Nicastro, D., Gerisch, G., and Baumeister, W. (2002b) Macromolecular architecture in eukaryotic cells visualized by cryoelectron tomography. *Science* 298: 1209-1213.

Meng, K.E., and Pfister, R.M. (1980) Intracellular structures of *Mycoplasma pneumoniae* revealed after membrane removal. *J Bacteriol* 144: 390-399.

Milazzo, A.C., Leblanc, P., Duttweiler, F., Jin, L., Bouwer, J.C., Peltier, S., Ellisman, M., Bieser, F., Matis, H.S., Wieman, H., Denes, P., Kleinfelder, S., and Xuong, N.H. (2005) Active pixel sensor array as a detector for electron microscopy. *Ultramicroscopy* 104: 152-159.

Murphy, G.E., Leadbetter, J.R., and Jensen, G.J. (2006) In situ structure of the complete Treponema primitia flagellar motor. *Nature* 442: 1062-1064.

Nicastro, D., Frangakis, A.S., Typke, D., and Baumeister, W. (2000) Cryo-electron tomography of neurospora mitochondria. *J Struct Biol* 129: 48-56.

Nicastro, D., Schwartz, C., Pierson, J., Gaudette, R., Porter, M.E., and McIntosh, J.R. (2006) The molecular architecture of axonemes revealed by cryoelectron tomography. *Science* 313: 944-948.

Papazisi, L., Troy, K.E., Gorton, T.S., Liao, X., and Geary, S.J. (2000) Analysis of Cytadherence-Deficient, GapA-Negative *Mycoplasma gallisepticum* Strain R. *Infect Immun* 68: 6643-6649.

Porter, K.R., and Yegian, D. (1945) Some Artifacts Encountered in Stained Preparations of Tubercle Bacilli: II. Much Granules and Beads. *J Bacteriol* 50: 563-575.

Regula, J.T., Boguth, G., Gorg, A., Hegermann, J., Mayer, F., Frank, R., and Herrmann, R. (2001) Defining the mycoplasma 'cytoskeleton': the protein composition of the Triton X-100 insoluble fraction of the bacterium *Mycoplasma pneumoniae* determined by 2-D gel electrophoresis and mass spectrometry. *Microbiology* 147: 1045-1057.

Scheffel, A., Gruska, M., Faivre, D., Linaroudis, A., Plitzko, J.M., and Schuler, D. (2006) An acidic protein aligns magnetosomes along a filamentous structure in magnetotactic bacteria. *Nature* 440: 110-114.

Scorrano, L., Ashiya, M., Buttle, K., Weiler, S., Oakes, S.A., Mannella, C.A., and Korsmeyer, S.J. (2002) A distinct pathway remodels mitochondrial cristae and mobilizes cytochrome c during apoptosis. *Dev Cell* 2: 55-67.

Seto, S., Layh-Schmitt, G., Kenri, T., and Miyata, M. (2001) Visualization of the attachment organelle and cytadherence proteins of *Mycoplasma pneumoniae* by immunofluorescence microscopy. *J Bacteriol* 183: 1621-1630.

Seto, S., and Miyata, M. (2003) Attachment Organelle Formation Represented by Localization of Cytadherence Proteins and Formation of the Electron-Dense Core in Wild-Type and Mutant Strains of Mycoplasma pneumoniae. *J Bacteriol* 185: 1082-1091.

Seybert, A., Herrmann, R., and Frangakis, A.S. (2006) Structural analysis of Mycoplasma pneumoniae by cryo-electron tomography. *J Struct Biol* 156: 342-354.

Shimoni, E., Rav-Hon, O., Ohad, I., Brumfeld, V., and Reich, Z. (2005) Three-dimensional organization of higher-plant chloroplast thylakoid membranes revealed by electron tomography. *Plant Cell* 17: 2580-2586.

Storrie, B., and Nilsson, T. (2002) The Golgi apparatus: balancing new with old. *Traffic* 3: 521-529.

Sui, H., and Downing, K.H. (2006) Molecular architecture of axonemal microtubule doublets revealed by cryo-electron tomography. *Nature* 442: 475-478.

Willig, K.I., Kellner, R.R., Medda, R., Hein, B., Jakobs, S., and Hell, S.W. (2006) Nanoscale resolution in GFP-based microscopy. *Nat Methods* 3: 721-723.

Yonekura, K., Braunfeld, M.B., Maki-Yonekura, S., and Agard, D.A. (2006) Electron energy filtering significantly improves amplitude contrast of frozen-hydrated protein at 300kV. *J Struct Biol* 156: 524-536.

Chapter 2: Three-dimensional structure of *Mycoplasma pneumoniae*'s attachment organelle and a model for its role in gliding motility

Gregory P. Henderson and Grant J. Jensen*

Division of Biology, California Institute of Technology, Pasadena, California

* Corresponding Author. Mail address: Caltech Division of Biology, 1200 E. California Blvd., Pasadena, CA 91125. Phone: (626) 395-8827. Fax: (626) 395-5730. E-mail: jensen@caltech.edu.

Published in *Molecular Microbiology* 2006 Apr; 60(2): 376-385 (Blackwell Publishing)

doi:10.1111/j.1365-2958.2006.05113.x

The definitive version is available at www.blackwell-synergy.com

Abstract

While most motile bacteria propel themselves with flagella, other mechanisms have been described including retraction of surface-attached pili, secretion of polysaccharides, or movement of motors along surface protein tracks. These have been referred to collectively as forms of "gliding" motility. Despite being simultaneously one of the smallest and simplest of all known cells, *Mycoplasma pneumoniae* builds a surprisingly large and complex cell extension known as the attachment organelle that enables it to glide. Here, three-dimensional images of the attachment organelle were produced with unprecedented clarity and authenticity using state-of-the-art electron cryotomography. The attachment organelle was seen to contain a multi-subunit, jointed, dynamic motor much larger than a flagellar basal body and comparable in complexity. A new model for its function is proposed wherein inchworm-like conformational changes of its electron-dense core are leveraged against a cytoplasmic anchor and transmitted to the surface through layered adhesion proteins.

Key Words

Mycoplasma pneumoniae, attachment organelle, prokaryotic cytoskeleton, electron cryomicroscopy, cell motility

Introduction

The mycoplasmas are simultaneously the smallest and simplest of known cells. Volumes can be ~ 25 times smaller than *Escherichia coli* (Biberfeld and Biberfeld, 1970), and their genomes can be limited to only several hundred genes (Fraser et al., 1995; Himmelreich et al., 1996). Despite the pressures that drove them to such minimization, amazingly, some construct a complex structure at their tips called the attachment organelle whose predicted mass is greater than that of a vertebrate nuclear pore complex! In *M. pneumoniae* this attachment organelle is essential for cytadherence (Baseman et al., 1982; Morrison-Plummer et al., 1986) and motility (Balish et al., 2003; Hasselbring et al., 2005; Seto et al., 2005a), but the mechanisms are unknown.

Various types of motility have been described in prokaryotes. While the most common type is flagellar, a number of non-flagellar, so-called "gliding" forms of movement also exist. The "twitching" motility of *Pseudomonas aeruginosa* and the "social" motility of *Myxococcus xanthus* are effected by cells extending and retracting surface-attached type IV pili (Mattick, 2002). Filamentous cyanobacteria and the "adventurous" motility of *M. xanthus* rely on the secretion of polysaccharide slime (McBride, 2001). *Flavobacterium johnsoniae* is thought to move by a treadmilling mechanism involving surface protein that move along tracks on the cell surface (McBride, 2001). Even among the motile mycoplasmas, various forms of motility appear to exist. *Mycoplasma mobile* relies on three large surface proteins (Seto et al., 2005b; Uenoyama et al., 2004; Uenoyama and Miyata, 2005), but these proteins lack clear homologs in other motile mycoplasma species such as *Mycoplasma genitalium* and *M. pneumoniae* (Miyata, 2005). Instead, these organisms'

motility appears to depend on the attachment organelle, which therefore probably underlies an entirely unique and interesting form of gliding motility.

M. pneumoniae causes bronchitis and atypical pneumoniae in humans by binding to the respiratory epithelium using surface proteins localized by the attachment organelle. Adhesion P1 (169 kDa) and accessory protein P30 (30 kDa) are necessary for this adhesion (Morrison-Plummer et al., 1986) and for cell motility (Hasselbring et al., 2005; Seto et al., 2005a). Specifically P30 has been proposed to serve as a link between the force generation mechanism and the surface adhesion proteins (Hasselbring et al., 2005). Other surface proteins include protein B (90 kDa) and protein C (40 kDa), which help to localize P1 (Baseman et al., 1982). Proteins P65 and the HMWs1-3 are associated with the organelle, but their spatial arrangements and functions are unknown (Krause and Balish, 2004). A massive protein assembly over 220 nm long and 50 nm thick known as the "electron-dense core" occupies the center of the attachment organelle (Biberfeld and Biberfeld, 1970; Wilson and Collier, 1976). Current characterizations of the core describe it as two uniform, striated rods separated by a thin gap (Hegermann et al., 2002; Meng and Pfister, 1980). A distal enlargement of the core has been referred to as the terminal button. The proximal end of the electron-dense core has been proposed to connect to a so-called “wheel-like complex” thought to be composed of two rings of proteins that connect to radial spokes connecting to the membrane (Hegermann et al., 2002). In both the attachment organelle and the cytoplasm, 5 nm fibers have been reported (Gobel et al., 1981; Meng and Pfister, 1980).

Studying the macromolecular structures in *M. pneumoniae* has proven difficult. Methods for genetic manipulation are still developing. Light microscopy is limited to resolving the relative positions of labeled proteins along the length of the cell. While

electron microscopy has the resolving power to visualize large protein complexes, traditional plastic-embedding methods have obscured important details. Electron cryotomography (ECT) is an emerging technique that can produce three-dimensional images of intact cells no thicker than about half a micron, in a life-like, "frozen-hydrated" state (Lucic et al., 2005). Here, we have used ECT to image the attachment organelle of *M. pneumoniae* with unprecedented clarity and authenticity. It was seen to be composed of at least eleven distinct protein structures surrounded by a curious electron-lucent area and a membrane studded with organized surface proteins. Based on these results, we propose a model for its role in a new form of gliding motility.

Results

Location of the electron-dense core within a cell. Twelve imaged *M. pneumoniae* cells were reconstructed (Fig. II-1) containing a total of nineteen attachment organelles (Fig II-2). The attachment organelles were marked by co-localization of an electron-dense core beneath the membrane, an electron-lucent area surrounding the core, and packed surface proteins. As expected from previous work, we found cells where the electron-dense core protruded out away from the body of the cell within a membranous finger-like extension (Fig. II-2a-i). With our population of cells, however, nearly half of the cells had the electron-dense core fully internalized into the cell's body, lying next to the cell membrane with only the head of the terminal button maintaining contact with the membrane (Fig. II-2j-n).

Membrane proteins. Surface proteins were found to form tightly packed rows ~ 5.5 nm thick on the extracellular surface of the attachment organelle (component "A" of the

schematic in Fig. II-2 and highlighted in Fig. II-3). These rows localized over the terminal button and extended down the attachment organelle over the electron-lucent areas. Another layer of proteins was seen immediately adjacent to the membrane inside the cell (component "B," pointed to specifically in Fig. II-4a).

Electron-dense core. The distal end of the electron-dense core has been called the terminal button. Here, the terminal button was seen to be composed of at least three parts. Most distally, there was an arched patch of discrete globular proteins (component "C," pointed to specifically in Fig. II-4a) that appeared to contact the inner layer of peripheral membrane proteins. More proximally the terminal button contained two nodules (components "D" and "E") with a gap between them perpendicular to the axis of the core (Fig. II-4b). The two nodules did not appear to be completely separated, but instead were probably connected at points around their edges. The more proximal nodule (component "E") made contact with one of the rods of the electron-dense core. Two parallel rods of different thicknesses and lengths made up the majority of the core, and these were both bent ~ 150° just proximal to their midpoint (Fig. II-5a). The outer rod (components "F" and "H") was thicker and varied in thickness from 13 to 31 nm. It was also longer, and was the one that eventually made contact with the terminal button. The thinner rod (components "G" and "I") appeared along the inner curvature and was ~ 8 nm in width. Between these two rods was a gap of ~ 7 nm (Fig. II-5b). The morphology of both the thick and thin rods changed after the bend. After careful study of the structure in three dimensions, it was seen that distal to the bend both rods (components "F" and "G") were discretely segmented like a vertebral column with gaps perpendicular to the axis of the core; proximal to the bend (components "I" and "H"), the rods were continuous (Fig. II-5c). There were about twelve segments plus one

or two additional segments in the thick rod that formed the connection with the terminal button. While the core was clearly made of two rods with multiple segments each, extensive contacts were also apparent which presumably explain how the core maintains its integrity even through partial purification. To investigate these contacts a computational "fill" tool was used to identify all the voxels with a density above a certain threshold that touched one another in the region of the core (Fig. II-5d). When these voxels were rendered with a single surface (Fig. II-5e), numerous connections between individual segments and the two rods were seen. In total, the cores (components "C"-"I") measured ~ 255 nm in length, and their volumes corresponded to a molecular weight of > 200 MDa.

Bowl complex. A shallow bowl-like complex was observed proximal to the core in some, but not all of the attachment organelles (component "K," highlighted in Fig. II-6). This bowl complex capped the core, but the distance and angle between the two varied (see also Fig. II-9 and its discussion below). Contrary to an earlier report, which described it as "wheel-like" (Hegermann et al., 2002), no spokes radiating perpendicular to the core axis were observed. A new density (component "J"), however, was seen connecting the bowl complex to the electron-dense core.

Electron-lucent area. Every core was surrounded by a curious electron-lucent area, irrespective of whether the attachment organelle protruded from the cell body or was internalized. Even though no barrier such as a protein wall or membrane was visible, large complexes such as ribosomes were clearly excluded from this region, which extended from component "C" to components "H" and "I." Again in contrast to an earlier report (Hegermann et al., 2002), no filamentous connections were found between the shaft of the electron-dense core and the membrane.

Replication of the attachment organelle. Approximately half (five out of twelve) of the observed cells had two electron-dense cores (see for example Fig. II-7), and one cell had three. The cores were found separated by various distances, including at opposite ends of the cell (Fig. II-1). No structural connections were seen between electron-dense cores within the same cell. In the cells where the attachment organelles protruded out away from the cell body and there were multiple cores, their proximal ends came nearest to each other, as this geometry requires. In contrast and not seen before, in the cells where there were multiple and internalized cores, the terminal buttons sometimes came nearest to each other. In the cell with three cores, two of the cores were close and formed a "V" shape, abutting near the bowl complex and diverging towards the terminal button. The third core was more distant, and its terminal button pointed towards the distal ends of the other two. In the cells with multiple cores, bowl complexes were always seen with at least one but not necessarily all cores.

Cytoskeleton filaments. Previous studies on *M. pneumoniae* have often looked at the structure that remains after solubilizing the cell membrane with the detergent Triton X-100, and have repeatedly reported that 5 nm filaments were associated with the core (Gobel et al., 1981; Hegermann et al., 2002; Meng and Pfister, 1980). Loose bundles of ~ 5 nm diameter filaments were also seen here in three cells (Fig. II-8), but were not visibly connected to the core. Instead they were only seen where the cell body narrowed as it stretched across the supporting carbon film.

Discussion

Earlier preparative techniques of plastic-embedding and detergent removal of the membrane left the structural details of the attachment organelle uncertain because these methods disrupted native conditions and probably introduced artifacts. Here, cells were plunge-frozen and imaged in an intact, frozen-hydrated and therefore near-native state. The cells we imaged were mostly unattached to any surface and had been dislodged from the culture flask before they were applied to the EM grid. This may explain why some of the cells were more pleomorphic than the rod-shapes seen before, and why some of the electron-dense cores were internalized rather than protruding from the main cell body. Nevertheless in all cases the electron-dense core was seen to be attached to the membrane by the terminal button, surrounded by an electron-lucent area, and accompanied by rows of surface proteins.

We found that the native attachment organelle is an enormous, complex, conformationally flexible molecular machine composed of at least eleven distinct regions. Previous observations of split electron-dense cores (Hegermann et al., 2002; Willby and Krause, 2002) led to the hypothesis that cores replicate through a semi-conservative mechanism, where the two rods of the core separate and each serves as a template to rebuild a partner (Krause and Balish, 2004). Our observations did not specifically support this model, since the two rods of the core are not identical and no cores were observed with only one rod, even when the cores were in close proximity and had presumably just replicated.

While some information is available about the localization of proteins P1, B, C, P65, P30, and HMW1-3, the structural clues gathered here were insufficient to assign them to specific components. We can conclude, however, that the surface proteins are densely packed and must work as complexes, since the densities seen were too large to be individual

proteins. The identity of the cytoskeletal filaments is particularly interesting. Of the known bacterial cytoskeletal proteins, only FtsZ (MPN 317) has been recognized in *M. pneumoniae*. Other potential candidates include EF-Tu (MPN 665), which has been shown to form filaments *in vitro* (Beck et al., 1978); and DnaK (MPN 434, also known as Hsp70), which has been characterized as a protein chaperone but is structurally homologous to actin (Flaherty et al., 1991). Interestingly, DnaK was also shown to be associated with P1 by chemical cross-linking (Layh-Schmitt et al., 2000). Since each of these three candidate filament-forming proteins is near ubiquitous in prokaryotes, knowledge of their potentially filamentous nature and arrangement *in vivo* here could have widespread implications.

Why would one of the smallest and simplest of all cells construct an organelle with such a fantastic size and complexity? While the attachment organelle is known to be required for adhesion (Morrison-Plummer et al., 1986), this may only require localization of key surface proteins, and would by itself hardly require such a sophisticated structure. We considered the possibility that the two-rod core could be like a harpoon or crossbow, where one rod advanced with respect to the other to press against or puncture host cells. Nothing like this has ever been seen, however, in thin-section EM images of *M. pneumoniae* attached to tracheal epithelium (Wilson and Collier, 1976). Metabolic functions such as substrate channeling or histone-like DNA-organizing functions also seem unlikely.

Building on (1) published evidence suggesting that the attachment organelle is where the motive force in these cells is generated (Hasselbring et al., 2005; Seto et al., 2005a), (2) mutational data showing that the core itself is required for motility (Balish et al., 2003; Balish and Krause, 2005), and (3) our observations here of the complexity and conformational flexibility of the core, we propose that *the core itself is the molecular motor*

that produces movement. We suggest a model in which the electron-dense core undergoes inchworm-like conformational changes that push the tip of the cell forward in small steps. Starting with surface proteins at the tip bound to a substrate and the core fully extended, the core may cyclically contract by bending at its various joints and/or minimizing the gaps between its segments, and then spring back to full length. When it springs back to full length, the bowl complex may provide leverage and resistance, like a paddle against water, especially if in fact the cytoplasmic filaments do indeed attach to it as suggested earlier (but not seen here, although if filaments bent rapidly they could have escaped our detection) and further gel the adjacent cytoplasm. Extension of the core would then require new membrane to "roll" down from above in front of the terminal button, attracting a new plaque of surface adhesion proteins that might prevent regression. As the cell advanced and earlier contacts moved towards the rear, they might weaken and release, perhaps through loss of the organization originally imposed on them by other elements of the attachment organelle like the layer of submembrane proteins seen here (component "B").

One attractive aspect of this model is that it could explain the otherwise mysterious electron-lucent area. Patterned beating of the core could clear the area of large macromolecules leaving only smaller molecules and water, just as any shaking tends to separate objects with different properties. This would be true regardless of whether the core was internalized within the cell body or protruding in a finger-like extension, just as we saw here. Published pictures of *M. penetrans,* however, argue against this explanation. *M. penetrans* is a relative of *M. pneumoniae,* which also apparently excludes large macromolecules from its tip, but it lacks an analogous core. More specifically and in contrast to our results here, *M. penetrans*' tip has been described as filled with densely

packed fine granules (Lo et al., 1992; Neyrolles et al., 1998). Until this structure is also imaged in its native state by ECT, conclusive comparisons are probably premature. In the absence of any membrane or protein boundary, an alternative explanation is that some sort of gel could actually be responsible for excluding large macromolecules in both species.

The core motility model also offers an explanation for the size and complexity of the core, the solid bowl complex, and the organized rows of proteins both inside and outside the membrane. The motility of the attachment organelle might be important for cell division. The attachment organelle has been seen to replicate, migrate to opposite sides of pre-divisional cells, and then stay at the forefront of the daughter cells as they separate (Seto et al., 2001). It may actually pull the daughter cells apart. The bacterial genome may also attach to the organelle, perhaps via the bowl complex, to ensure chromosome segregation (Seto et al., 2001).

In an effort to identify conformational flexibility within the attachment organelle in support of our model, we found three types of evidence: (1) the spacing between the segments of the electron-dense core and also the nodules of the terminal button were variable, like an accordion; (2) sometimes all the segments were straight, sometimes they were curved inwards, and sometimes they were curved outwards; and (3) the position and orientation of the bowl complex varied (Fig. II-9). Because the cells were unattached to any surface when imaged, however, these conformational changes may not be associated with those that occur during gliding motility. If our model is correct, we would also have expected larger variations as well. Perhaps they exist, but are so short-lived that none were captured and imaged here.

Other models of motility were considered. Current models for the motility of *M. mobile* propose that individual surface proteins cyclically stroke a surface, propelling the cell like the feet of a centipede (Uenoyama et al., 2004). While these proteins are localized to an elongated extension of the cell similar to the attachment organelle of *M. pneumoniae,* they are excluded from its tip (Uenoyama and Miyata, 2005). No homologs to these proteins have been found in *M. pneumoniae* (Miyata, 2005) and *M. mobile* does not appear to have either an electron-dense core or an electron-lucent area (Shimizu and Miyata, 2002). If the mechanisms in the two organisms were nevertheless similar, one wonders what would justify the size and complexity of the electron-dense core and explain the electron-lucent area. A conveyor-belt model for track-based motility (McBride, 2001) also seems discordant with our observations here because no array of structural links were seen between the shaft of the core and the rows of membrane proteins.

Our proposed model makes testable predictions. First, it predicts that the gliding motility in *M. pneumoniae* should be incremental with at least a roughly characteristic step size. Second, unlike strictly structural proteins, some component of the core must consume energy. Third, directed movement would require that the core contact a surface through adhesion proteins in a surrounding membrane (i.e., isolated cores might "twitch," but not move forward steadily, and isolated membranes with their surface proteins would be motionless). Fourth, in contrast to individual surface proteins of current *M. mobile* models which would remain fixed relative to the tip, individual adhesion proteins labeled here would cycle from the tip of the attachment organelle towards the rear, then release the surface and diffuse back up to the front. More work is needed to identify the proteins that form each component and to test these predictions.

Experimental Procedures

Cultivation conditions. Wild-type *M. pneumoniae*, cell strain M129 (Lipman et al., 1969), was cultured for 2-3 days in 10 mL SP-4 medium at 37° C in a plastic culture flask (25 cm^2) (Tully et al., 1977). Cells were then scraped off the culture flask and concentrated by centrifugation (10,000 x g for 3 min).

Electron cryotomography. Concentrated *M. pneumoniae* were applied to glow-discharged Quantifoil (SPI Supplies) or lacy carbon (Ted Pella, Inc.) grids previously treated with 10-nm gold fiducial markers. Excess liquid was removed and the samples were plunge-frozen in liquid ethane using a Vitrobot (FEI). Maintaining the samples at liquid nitrogen temperature throughout the experiment, the grids were loaded into "flip-flop" tilt rotation holders and loaded into a 300 kV, FEG, G2 Polara transmission EM (FEI). Image series were acquired at half- to three-degree intervals, tilting the sample between roughly -62° to +62°, using the predictive UCSF tomography software package (Zheng et al., 2004). All images were zero-loss filtered with a slit-width of 20 eV. For some cells the grid was rotated 90° between a first and second tilt-series (Iancu et al., 2005). Images were acquired under low-dose conditions 10 to 30 μm underfocus and with a magnification such that after the energy filter, each pixel on the CCD represented between 0.56 and 0.82 nm on the specimen plane.

Image analysis. Images were aligned using gold fiducial markers. Single-axis tilt-series were reconstructed by weighted back-projection and dual-axis tilt-series were merged using IMOD (Mastronarde, 1997). Reconstructions were denoised using non-linear anisotropic diffusion (Frangakis and Hegerl, 2001), distributed across the network of lab workstations

with the Peach system (Leong et al., 2005). Images were produced using IMOD or the Amira software package (Mercury Computer Systems, Inc.). All the images shown were denoised except for those in Fig. II-1.

Acknowledgements

This work was supported in part by NIH grant P01 GM66521 to GJJ, DOE grant DE-FG02-04ER63785 to GJJ, a Searle Scholar Award to GJJ, and gifts to Caltech from the Ralph M. Parsons Foundation, the Agouron Institute, and the Gordon and Betty Moore Foundation. We thank Duncan C. Krause of the University of Georgia for providing *M. pneumoniae* M129, for repeated discussions, for sharing unpublished data, and for his reading of the manuscript.

References

Balish, M.F., Santurri, R.T., Ricci, A.M., Lee, K.K., and Krause, D.C. (2003) Localization of *Mycoplasma pneumoniae* cytadherence-associated protein HMW2 by fusion with green fluorescent protein: implications for attachment organelle structure. *Mol Microbiol* **47**: 49-60.

Balish, M.F., and Krause, D.C. (2005) Mycoplasma attachment organelle and cell division. In *Mycoplasmas molecular biology pathogenicity and strategies for control.* Blanchard, A., and Browning, G. (eds.). Wymondham: Horizon Bioscience, pp. 189-237.

Baseman, J.B., Cole, R.M., Krause, D.C., and Leith, D.K. (1982) Molecular basis for cytadsorption of *Mycoplasma pneumoniae*. *J Bacteriol* **151**: 1514-1552.

Beck, B.D., Arscott, P.G., and Jacobson, A. (1978) Novel properties of bacterial elongation factor Tu. *Proc Natl Acad Sci U S A* **75**: 1250-1254.

Biberfeld, G., and Biberfeld, P. (1970) Ultrastructural features of *Mycoplasma pneumoniae*. *J Bacteriol* **102**: 855-861.

Flaherty, K.M., McKay, D.B., Kabsch, W., and Holmes, K.C. (1991) Similarity of the three-dimensional structures of actin and the ATPase fragment of a 70-kDa heat shock cognate protein. *Proc Natl Acad Sci U S A* **88**: 5041-5045.

Frangakis, A.S., and Hegerl, R. (2001) Noise reduction in electron tomographic reconstructions using nonlinear anisotropic diffusion. *J Struct Biol* **135**: 239-250.

Fraser, C.M., Gocayne, J.D., White, O., Adams, M.D., Clayton, R.A., Fleischmann, R.D., et al. (1995) The minimal gene complement of *Mycoplasma genitalium*. *Science* **270**: 397-404.

Gobel, U., Speth, V., and Bredt, W. (1981) Filamentous structures in adherent *Mycoplasma pneumoniae* cells treated with nonionic detergents. *J Cell Biol* **91**: 537-543.

Hasselbring, B.M., Jordan, J.L., and Krause, D.C. (2005) Mutant analysis reveals a specific requirement for protein P30 in *Mycoplasma pneumoniae* gliding motility. *J Bacteriol* **187**: 6281-6289.

Hegermann, J., Herrmann, R., and Mayer, F. (2002) Cytoskeletal elements in the bacterium *Mycoplasma pneumoniae*. *Naturwissenschaften* **89**: 453-458.

Himmelreich, R., Hilbert, H., Plagens, H., Pirkl, E., Li, B.C., and Herrmann, R. (1996) Complete sequence analysis of the genome of the bacterium *Mycoplasma pneumoniae*. *Nucleic Acids Res* **24**: 4420.

Iancu, C.V., Wright, E.R., Benjamin, J., Tivol, W.F., Dias, D.P., Murphy, G.E., et al. (2005) A "flip-flop" rotation stage for routine dual-axis electron cryotomography. *J Struct Biol.* **151**: 288.

Krause, D.C., and Balish, M.F. (2004) Cellular engineering in a minimal microbe: structure and assembly of the terminal organelle of *Mycoplasma pneumoniae*. *Mol Microbiol* **51**: 917-924.

Layh-Schmitt, G., Podtelejnikov, A., and Mann, M. (2000) Proteins complexed to the P1 adhesin of *Mycoplasma pneumoniae*. *Microbiology* **146**: 741-747.

Leong, P.A., Heymann, J.B., and Jensen, G.J. (2005) Peach: a simple Perl-based system for distributed computation and its application to cryo-EM data processing. *Structure* **13**: 505.

Lipman, R.P., Clyde, W.A., Jr., and Denny, F.W. (1969) Characteristics of virulent, attenuated, and avirulent *Mycoplasma pneumoniae* strains. *J Bacteriol* **100**: 1037-1043.

Lo, S.-c., Hayes, M.M., Tully, J.G., Wang, R.Y.-H., Kotani, H., Pierce, P.F., et al. (1992) *Myoplasma penetrans* sp. nov., from the urogenital tract of patients with AIDS. *Int. J. Syst Bacteriol* **42**: 357-364.

Lucic, V., Forster, F., and Baumeister, W. (2005) Structural studies by electron tomography: from cells to molecules. *Annu Rev Biochem* **74**: 833-865.

Mastronarde, D.N. (1997) Dual-axis tomography: an approach with alignment methods that preserve resolution. *J Struct Biol* **120**: 343.

Mattick, J.S. (2002) Type IV pili and twitching motility. *Annu Rev Micobiol* **56**: 289-314.

McBride, M.J. (2001) Bacterial gliding motility: multiple mechanisms for cell movement over surfaces. *Annu Rev Micobiol* **55**: 49-75.

Meng, K.E., and Pfister, R.M. (1980) Intracellular structures of *Mycoplasma pneumoniae* revealed after membrane removal. *J Bacteriol* **144**: 390-399.

Miyata, M. (2005) Gliding motility of mycoplasmas: the mechanism cannot be explained by current biology. In *Mycoplasmas molecular biology pathogenicity and strategies for control*. Blanchard, A., and Browning, G. (eds.). Wymondham: Horizon Bioscience, pp. 137-163.

Morrison-Plummer, J., Leith, D.K., and Baseman, J.B. (1986) Biological effects of anti-lipid and anti-protein monoclonal antibodies on *Mycoplasma pneumoniae*. *Infect Immun* **53**: 398-403.

Neyrolles, O., Brenner, C., Prevost, M.-C., Fontaine, T., Montagnier, L., and Blanchard, A. (1998) Identification of two glycosylated components of *Mycoplasma penetrans*: a surface-exposed capsular polysaccharide and a glycolipid fraction. *Microbiology* **144**: 1247-1255.

Seto, S., Layh-Schmitt, G., Kenri, T., and Miyata, M. (2001) Visualization of the attachment organelle and cytadherence proteins of *Mycoplasma pneumoniae* by immunofluorescence microscopy. *J Bacteriol* **183**: 1621-1630.

Seto, S., Kenri, T., Tomiyama, T., and Miyata, M. (2005a) Involvement of P1 adhesin in gliding motility of *Mycoplasma pneumoniae* as revealed by the inhibitory effects of antibody under optimized gliding conditions. *J Bacteriol* **187**: 1875-1877.

Seto, S., Uenoyama, A., and Miyata, M. (2005b) Identification of a 521-kilodalton protein (Gli521) involved in force generation or force transmission for *Mycoplasma mobile* gliding. *J Bacteriol* **187**: 3502-3510.

Shimizu, T., and Miyata, M. (2002) Electron microscopic studies of three gliding mycoplasmas, *Mycoplasma mobile*, *M. pneumoniae*, and *M. gallisepticum*, by using the freeze-substitution technique. *Curr Microbiol* **44**: 431-434.

Tully, J., Whitcomb, R., Clark, H., and Williamson, D. (1977) Pathogenic mycoplasma: cultivation and vertebrate pathogenicity of a new spiroplasma. *Science* **195**: 892-894.

Uenoyama, A., Kusumoto, A., and Miyata, M. (2004) Identification of a 349-kilodalton protein (Gli349) responsible for cytadherence and glass binding during gliding of *Mycoplasma mobile*. *J Bacteriol* **186**: 1537-1545.

Uenoyama, A., and Miyata, M. (2005) Identification of a 123-kilodalton protein (Gli123) involved in machinery for gliding motility of *Mycoplasma mobile*. *J Bacteriol* **187**: 5578-5584.

Willby, M.J., and Krause, D.C. (2002) Characterization of a *Mycoplasma pneumoniae* hmw3 mutant: implications for attachment organelle assembly. *J Bacteriol* **184**: 3061-3068.

Wilson, M.H., and Collier, A.M. (1976) Ultrastructural study of *Mycoplasma pneumoniae* in organ culture. *J Bacteriol* **125**: 332-339.

Zheng, Q.S., Braunfeld, M.B., Sedat, J.W., and Agard, D.A. (2004) An improved strategy for automated electron microscopic tomography. *J Struct Biol* **147**: 91-101.

Figures

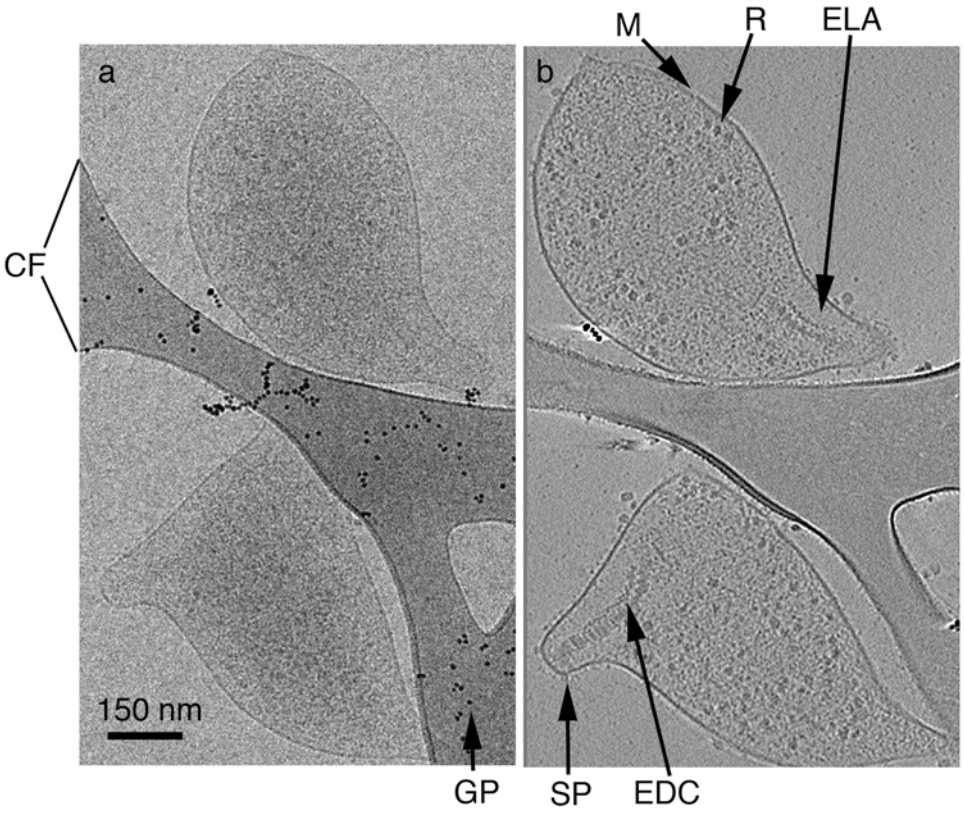

Figure II-1. Electron micrograph and tomographic reconstruction of a dividing *M. pneumoniae* cell. a) An example untilted projection image from the tilt-series of a single frozen-hydrated cell. The cell appears about to divide and is stretched over the carbon film of the grid. b) A 15 nm central slice through the three-dimensional reconstruction of the same cell perpendicular to the beam. Individual macromolecular complexes are visible, including the cell's two electron-dense cores. (These cores appear again in Fig. II-2f and e). CF–carbon film, EDC–electron-dense core, ELA–electron-lucent area, GP–gold particle, M–membrane, R–ribosome like particle, SP–surface proteins

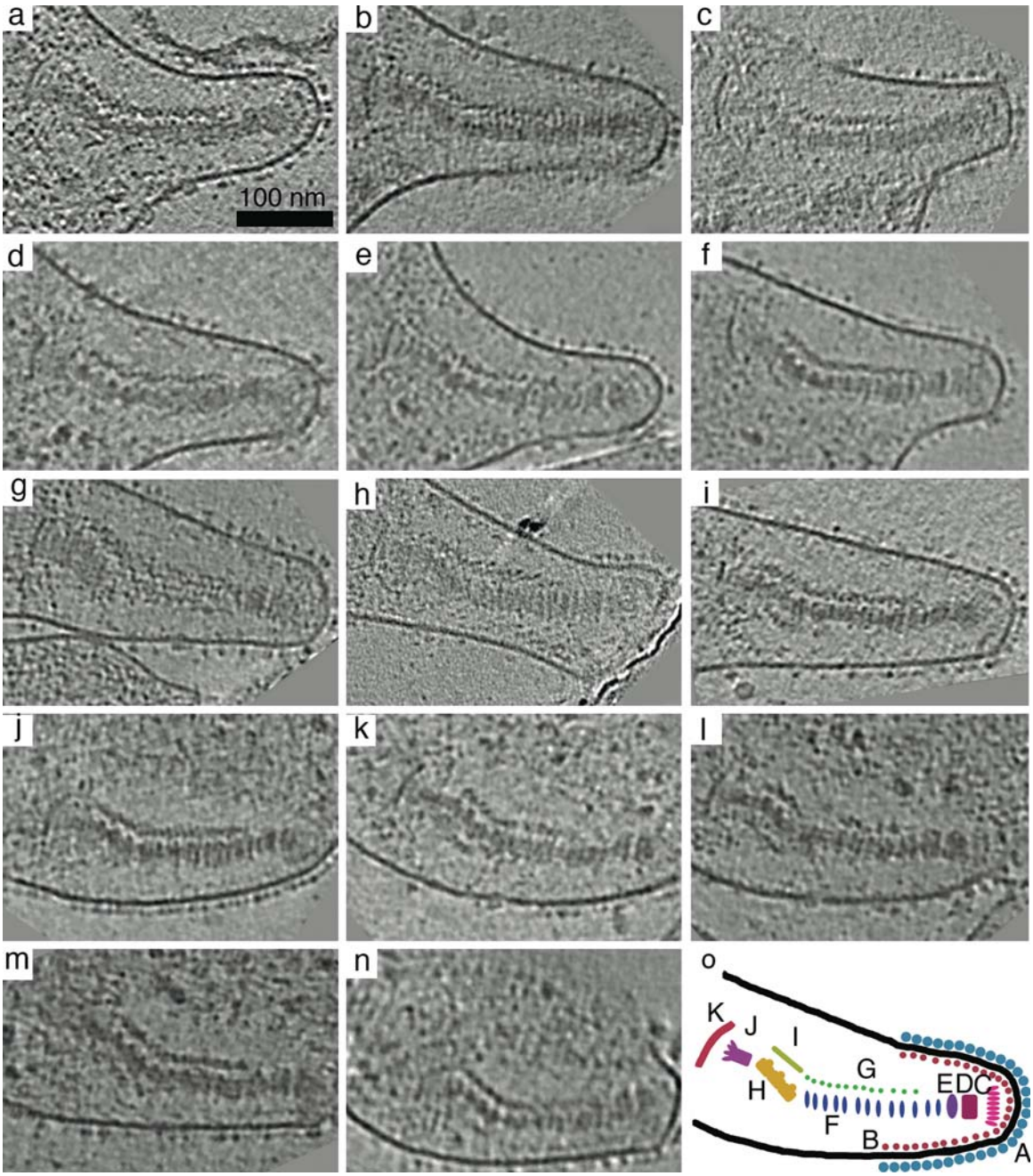

Figure II-2. Montage of attachment organelles and schematic. Each image represents a 10.7 to 22.4 nm thick slice through a tomogram oriented to expose the thick and thin rods of the electron-dense core. (Five additional cores were considered in the analysis but are not shown here.) a-i) Cores that protruded from the body of the cell within a membrane-enclosed, finger-like extension. j-n) Internalized cores. o) Schematic of the attachment organelle with components labeled for subsequent reference

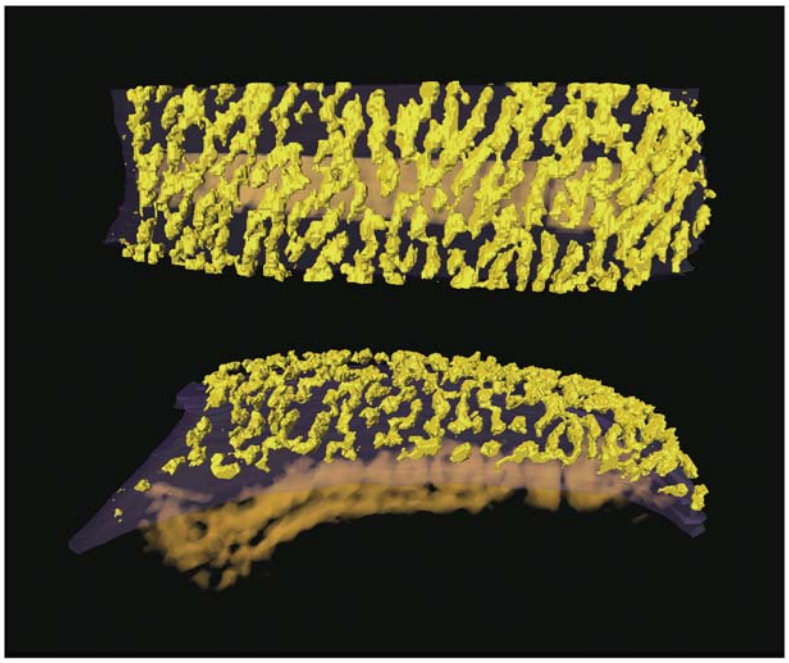

Figure II-3. Extracellular surface proteins. Two views of the attachment organelle pictured in Fig. II-2j are shown, tilted with respect to each other. The extracellular surface proteins were automatically segmented with a simple density threshold and surface-rendered in yellow. The membrane below was manually segmented and surface-rendered in purple. The electron-dense core was volume-rendered in orange. Because the views are three-dimensional with perspective, no scale bar is included.

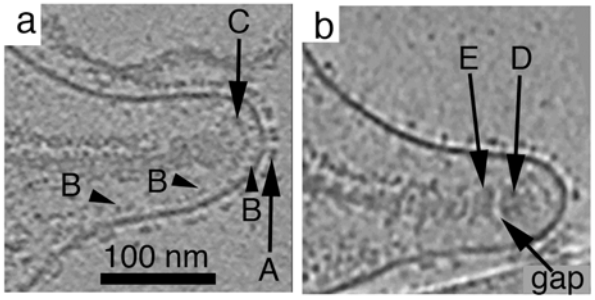

Figure II-4. Membrane proteins and terminal button. Slices through two different attachment organelles are shown and marked to highlight the membrane protein layers "A" and "B" and the three components of the terminal button "C"–"E" (the organelles in (a) and (b) are the same as those shown in Figs. II-2a and e, respectively). Capital letters–components as labeled in Fig. II-2o

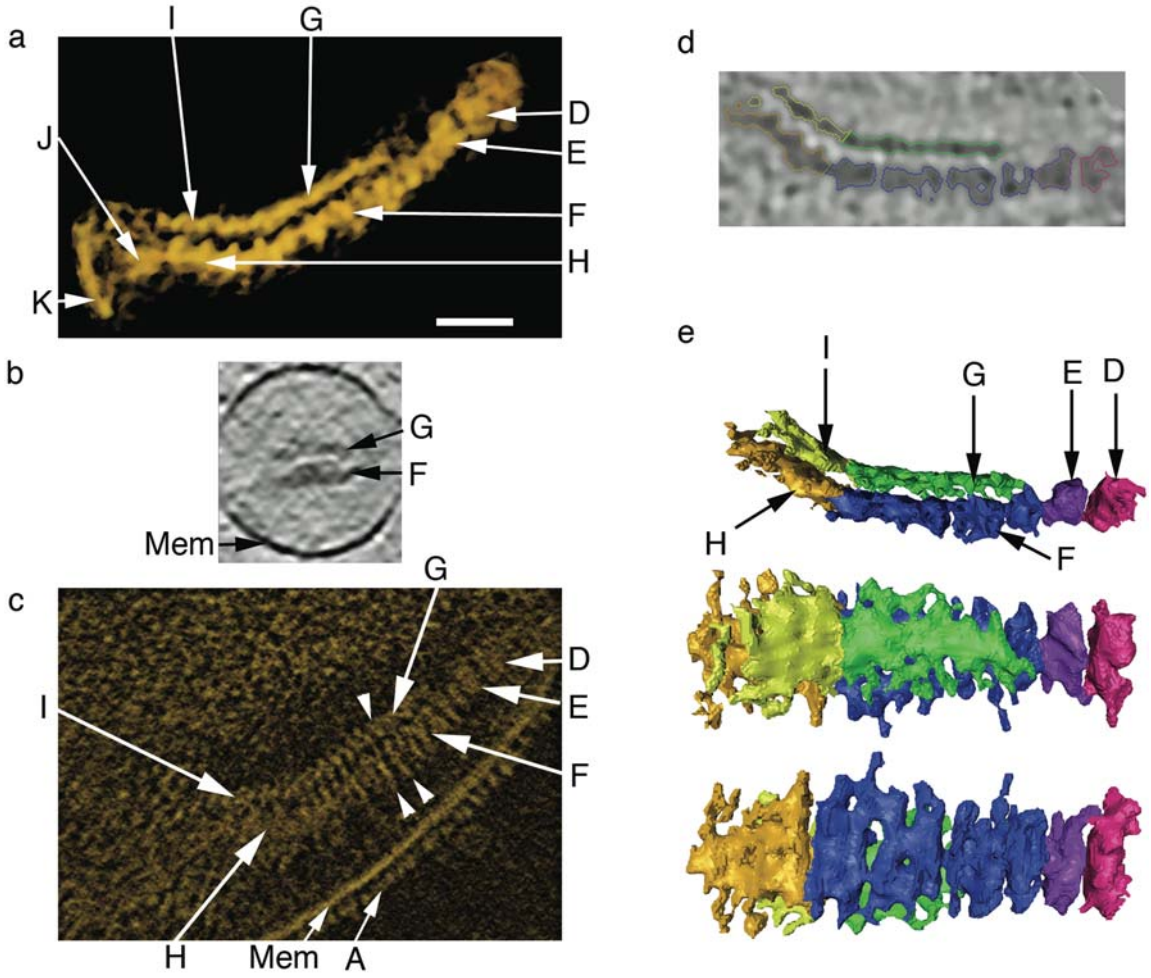

Figure II-5. Electron-dense core. a) Volume rendering of the electron-dense core and bowl complex shown in Fig. II-2a, with components labeled. b) Cross-section of the core shown in Fig. II-2i perpendicular to the long axis of the rods at a point distal to the bend. c) A thin section through the attachment organelle shown in Fig. II-2j, minimally denoised and volume rendered to highlight the fine structure of the core's distinct segments (arrowheads). d) Cross section of the same attachment organelle after further denoising and automatic segmentation with a "fill" tool to generate a surface. e) Surface rendering, rotated and color-coded as in Fig. II-2o to give a sense of the gross structure from different views. Note that the structure will appear slightly elongated from the "top" and "bottom" views due to the missing wedge of data in electron tomography. Mem–membrane

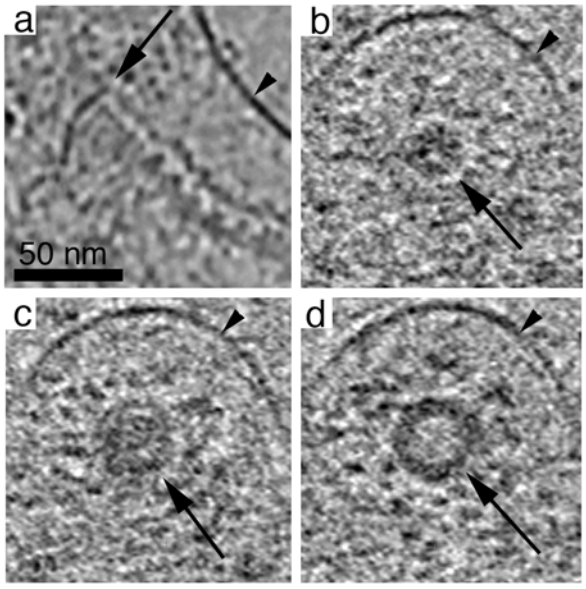

Figure II-6. Bowl complex. a) "Sagittal" section through the bowl complex and the proximal end of the electron-dense core shown in Fig. II-2e. b-d) "Coronal" 1.6 nm sections (roughly perpendicular to the axis of the core) through the bowl complex at different positions, starting at the bottom of the bowl and moving up to its rim. Arrows point to the bowl complex, while arrowheads point to the cell membrane.

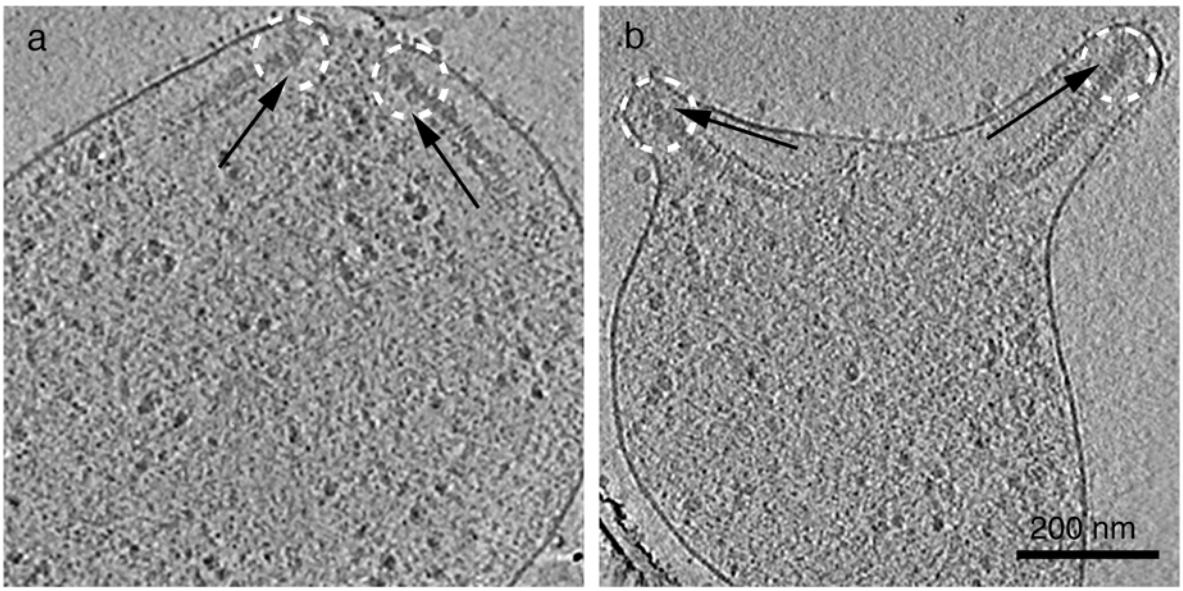

Figure II-7. Multiple electron-dense cores. Two cells with multiple electron-dense cores are shown where the terminal buttons (highlighted with white dotted circles) are oriented either towards (a) or away (b) from each other. The black arrows point from the bowl complex to the terminal button alongside the thin rods. The organelles in (a) and (b) are the same as those shown in Fig. II-2l and m and Fig. II-2b and c, respectively.

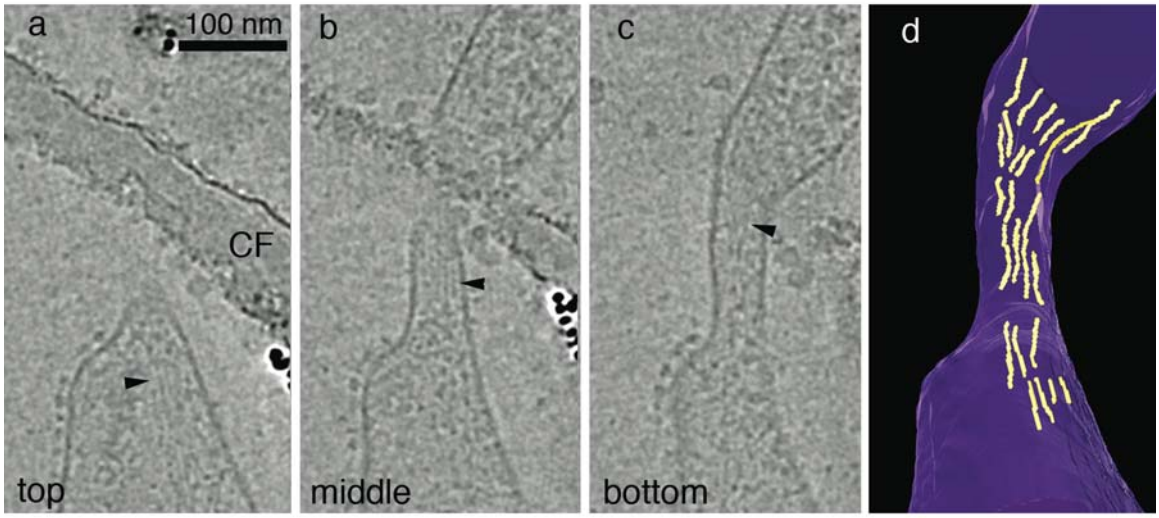

Figure II-8. Cytoskeleton filaments. a-c) Serial sections through a tomogram of one cell showing a bundle of 5 nm filaments running through a point of cell narrowing. Arrowheads point to the fiber bundle. d) Selective, manual, three-dimensional segmentation of some of the fibers (yellow). The membrane has been rendered purple. CF–carbon film

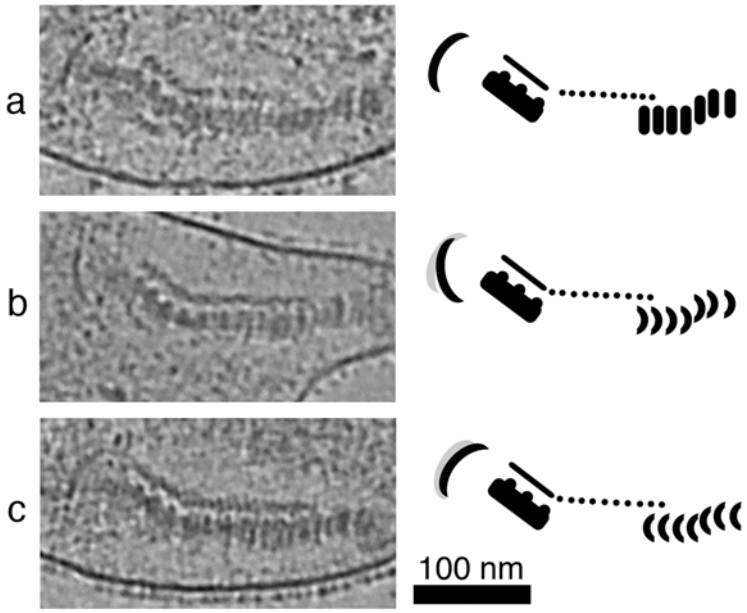

Figure II-9. Evidence of conformational changes. The attachment organelles from Fig. II-2k, f, and j are shown to the left of corresponding schematics highlighting conformational differences. The relative position of the first bowl complex is overlaid on the later two schematics as a grey shadow. For clarity the bowl complex is shown moving relative to a stable core, though the opposite, a stable bowl complex and mobile core, may be more likely.

3-D Ultrastructure of *O. tauri*:

Electron Cryotomography of an Entire Eukaryotic Cell

Gregory P. Henderson, Lu Gan, and Grant J. Jensen*

Division of Biology, California Institute of Technology, Pasadena, CA

Running Title: 3-D Ultrastructure of *Ostreococcus tauri*

* Corresponding Author. Mail address: Caltech Division of Biology, 1200 E. California Blvd., Pasadena, CA 91125. Phone: (626) 395-5730. Fax: (626) 395-5730. E-mail: jensen@caltech.edu.

Abstract

The hallmark of eukaryotic cells is their segregation of key biological functions into discrete, membrane-bound organelles. Creating accurate models of their ultrastructural complexity has been difficult in part because of the limited resolution of light microscopy and the artifact-prone nature of conventional electron microscopy. Here we explored the potential of the emerging technology electron cryotomography to produce three-dimensional images of an entire eukaryotic cell in a near-native state. *Ostreococcus tauri* was chosen as the specimen because as a unicellular picoplankton with just one copy of each organelle, it is the smallest known eukaryote and was therefore likely to yield the highest resolution images. Whole cells were imaged at various stages of the cell cycle, yielding 3-D reconstructions of complete chloroplasts, mitochondria, endoplasmic reticula, Golgi bodies, peroxisomes, microtubules, and putative ribosome distributions *in-situ*. Surprisingly, the nucleus was seen to open long before mitosis, and while one microtubule (or two in some predivisional cells) were consistently present, no mitotic spindle was ever observed, prompting speculation that a single microtubule might be sufficient to segregate multiple chromosomes.

Abbreviations

3-D, three-dimensional; ECT, electron cryotomography; ER, endoplasmic reticulum; NE, nuclear envelope; NPC, nuclear pore complex.

Introduction

The history of cell biology has been punctuated by major advances in imaging technologies. Following the invention of the electron microscope in the early 1930s, what we would now call the "conventional" specimen preparation methods of chemical fixation, dehydration, plastic-embedding, sectioning, and staining were developed to allow the visualization of biological material. While producing some artifacts, these methods have been profoundly successful, filling our textbooks with information about the structure and positions of cell walls, internal membranes, cytoskeletal filaments, and even large cytoplasmic particles like ribosomes. High-pressure freezing/freeze substitution fixation techniques have since improved specimen preservation (McDonald and Auer, 2006).

Recent technological developments have created the opportunity to realize two major improvements: imaging cells in three dimensions (3-D) and in nearly-native states. Cells can be imaged in 3-D through tomography (Lucic et al., 2005), a technique wherein specimens are imaged iteratively while being incrementally tilted around one or two axes. Full 3-D reconstructions of the sample can then be calculated. Computationally stacking such 3-D reconstructions of serial (thick) sections has made it possible to reconstruct even large regions of fixed cells (Hoog et al., 2007). With conventional sample preparation methods, however, image contrast arises from heavy metal salts surrounding cross-linked molecules held in place by a resin support. It has now also become possible to image non-chemically-fixed cells in a more nearly native state through plunge-freezing. Plunge-freezing preserves cells in a life-like, "frozen-hydrated" state free of stains and with minimal artifacts (Dubochet et al., 1988). Electron cryotomography

(ECT) combines these two advances to produce 3-D reconstructions of nearly-native biological material to "molecular" resolution (Grimm et al., 1997).

Because of multiple scattering, however, images of samples thicker than about 500 nm are difficult to interpret. Thus previous ECT work has focused on purified macromolecules, viruses, small prokaryotic cells (Jensen and Briegel, 2007), purified organelles (Nicastro et al., 2000), or cell peripheries (Medalia et al., 2002; Subramaniam and Milne, 2004), but the potential insight that might come from examining whole eukaryotic cells by ECT has not yet been realized because they are too thick. To this end methods are being developed to either cryosection frozen-hydrated tissues (Al-Amoudi et al., 2004) or focused-ion-beam mill thin slabs (Marko et al., 2007) suitable for tomography. Here we have taken an alternative approach by identifying and imaging the smallest known eukaryotic cell, *Ostreococcus tauri*.

O. tauri is a unicellular green alga (a "picoplankton") with only a single mitochondrion, chloroplast, and Golgi body (Chrétiennot-Dinet et al., 1995). It has been reported to be less than a micron in diameter, and because of its small size and presumed simplicity, it has been put forward as a model eukaryotic organism (Derelle et al., 2006). Nevertheless when *O. tauri*'s 12.6 megabase nuclear genome was sequenced (Derelle et al., 2006), it was found to have more genes (~ 8,200) than *Saccharomyces cerevisiae* (~ 6,600). These genes are distributed on 20 linear chromosomes. The Prasinophyceae lineage to which *O. tauri* belongs represents an early branch from the green lineage that includes the land plants (Courties et al., 1998; Yoon et al., 2004). Unlike other model plants *O. tauri* has only one copy of each class of cyclin-dependent kinases and cyclins (Robbens et al., 2005), making it a powerful system to study the cell cycle without

concerns of genetic redundancy. *O. tauri*'s cell cycle can be partially synchronized by growing the cells in a twelve hour light-and-dark cycle and further synchronization can be achieved pharmacologically (Farinas et al., 2006). Because of its small size, it may be the only eukaryotic cell known that can be effectively imaged intact throughout its entire life cycle by ECT.

Here we present ECT reconstructions of intact *O. tauri* cells frozen at different stages throughout the cell cycle. In addition to providing new insights into the ultrastructure of chloroplasts, mitochondria, endoplasmic reticula (ER), Golgi bodies, peroxisomes, microtubules, and the distribution of large macromolecular complexes, *O. tauri* presented a number of surprises, including a nuclear envelope (NE) that was open throughout most of the cell cycle, an unusually shaped ER, and a rough ER that was confined to the outer nuclear membrane. Perhaps most intriguingly, only one or two microtubules were ever observed in individual cells, suggesting that single microtubules might be sufficient to segregate multiple chromosomes. The Results and Discussion are presented one after another together for each topic below to improve the flow of the text, but a Conclusion has been added to place the whole work in context.

Results and Discussion

Cell Growth and Synchronization

Cells were obtained from a strain of *O. tauri* isolated from the Thau lagoon (France) (Courties et al., 1994). *O. tauri*'s growth was synchronized using a twelve-

hour-light, twelve-hour-dark cycle that resulted in an average of one cell division per day. A previous study found that under these growth conditions, cells at the dark-to-light transition were in the mid-G_1 phase of the cell cycle. Cells at the light-to-dark transition were found in various stages of the cell cycle including approximately 50% in early G_1, 10% in late G_1, 25% in S, and 15% in G_2/M (Farinas et al., 2006).

Sample Preservation Strategies

Cells from liquid cultures were prepared for EM using three different preparation methods: conventional fixation and embedding, high-pressure freezing/freeze-substitution fixation, and plunge-freezing (Figure III-S1). Conventional EM fixation revealed most membranes, but the membrane structures were badly distorted and any further details were difficult to resolve and/or poorly reproducible. High-pressure frozen specimens had markedly improved membrane preservation, especially in the chloroplast, but macromolecular complexes were not resolved. Further, because of stain and the generally high-density of the plastic-embedded samples, sections thick enough to contain entire cells could not be imaged. Thus reconstructing an entire cell would have required multiple serial sections. Plunge-frozen cells were imageable intact and exhibited good ultrastructural preservation, including readily resolvable ribosome-like particles, microtubules, and smooth cellular membranes. Moreover, plunge-freezing was both more consistently successful and significantly faster than high-pressure freezing, allowing a large number of whole cells to be imaged, and a more comprehensive survey of *O. tauri* ultrastructure to be obtained. The plunge-frozen cells were, however, at the limit of useful thickness for ECT (500 – 800 nm), so data could not be collected at tilt

angles greater than ~ 55–60˚ and the resolution of the reconstructions was correspondingly anisotropic.

Data Recorded

Cultures at both the dark-to-light and light-to-dark transitions were plunge-frozen. Samples were first surveyed in the EM to investigate the cell sizes and morphologies present. Cells were almost always round, and were seen to vary in diameter continuously from 1 to 2 μ on every grid, but cells were generally larger at the light-to-dark transition. In many of the cells frozen at the light-to-dark transition, it was possible to see in the surveys that the organelles were dividing. Full tilt-series of 52 cells were then recorded. Most of these were chosen because they were especially thin, which results in higher resolution reconstructions, or because they had visibly dividing organelles, but some were chosen almost randomly to broaden coverage of the cell cycle. The reconstructed cells were classified into two groups, "non-dividing" and "predivisional," based on whether or not their organelles were visibly dividing (Figure III-1). Of the 23 reconstructed cells taken from the dark-to-light transition, all but one were non-dividing, consistent with their being in G_1 as predicted by Farinas et al., 2006. Of the 29 reconstructed cells taken from the light-to-dark transition, 4 were non-dividing and 25 were predivisional.

Cell shape and content

While the limited tilt range decreased the resolution perpendicular to the grid, it was nevertheless clear that the frozen-hydrated cells were not spherical. Instead they

were rather flattened, ranging from 1.1 to 2.1 μm in diameter and 0.5 to 0.8 μm in thickness. The more flattened surfaces are referred to herein as the "top" and "bottom" of the cells, depending on their orientation on the grid, but there were no consistent structural features that indicated any functional distinction. The diameters and flatness observed here were consistent with earlier reports (Chrétiennot-Dinet et al., 1995), but to check whether surface tension flattened the cells beyond their normal state, cell shapes were also investigated by phase and differential interference contrast light microscopy of free-floating live cells. Free-floating cells also had flat profiles, but exhibited more complex morphologies with bends and depressions as if they were quite flexible (Figure III-2). Thus while the flattened morphology is natural, suspending the cells in thin fluid films across circular holes on an EM likely promoted a more round and simple shape.

All cells imaged by ECT contained a single mitochondrion, Golgi body, and chloroplast. Each cell also contained a nucleus with one to three discernable nuclear pore complexes (NPCs), a smooth ER, and a variety of vesicles that could not be identified. The non-dividing cells had a single peroxisome and microtubule, but some predivisional cells had two copies of each. The rough ER was limited only to the outer NE. One unusual cell had an oval shape with two terminal membrane-bound cell extensions (Figure III-1E-F). This cell was thinner than the others, had the long axis of the chloroplast turned ninety degrees relative to the long axis of the nucleus, and had giant holes in the NE.

Cellular Organization

The organization of the non-dividing cells was remarkably consistent. The largest organelles — the chloroplast and nucleus — resided in opposing semi-circular halves of the cell. The other organelles (mitochondrion, peroxisome, ER, Golgi body, vesicles) rested between them (Figure III-3). The nucleus and chloroplast pressed so closely to the plasma membrane that macromolecular complexes like ribosomes were sterically excluded. While the mitochondrion did not appear to have a fixed location and the chloroplast rested opposite the nucleus, the nuclear envelope (NE) appeared to organize the rest of the organelles. The outer nuclear membrane was contiguous with sheets of ER that were found to run parallel to the plasma membrane and around co-localized granules. The Golgi body was always found close to the nucleus. A single microtubule could be found in contact with the NE, near the top or bottom of the cell. The peroxisome, a large single-membrane vesicle known to be present in all eukaryotic cells, occupied the central region of the cell between the nucleus and the chloroplast (discussed later).

Six of the best reconstructed cells were used to estimate the volumes and surface areas of key organelles. These six (shown in Figure III-3) were chosen because they were among the thinnest cells and because they were imaged along two orthogonal axes, a practice that minimizes the effects of the missing wedge of data in ECT (Iancu et al., 2005). All six came from the dark-to-light transition. These presumably underwent cell division at the beginning of the 12-hour dark period, entered G_1, and then grew minimally due to lack of light. The average cell volume and surface area was 0.91 ± 0.07 μm^3 and 8.3 μm^2, respectively. The chloroplasts, nuclei, and mitochondria were the largest three organelles, occupying 47 ± 3, 17 ± 2, and $2.7 \pm 0.4\%$ of the cell volume, respectively.

The cytoplasm around the organelles occupied another 29±2% of the cell and granules and other vesicles occupied the remainder of the volume. In these thinnest of cells, the distribution of organellar volumes was remarkably consistent.

The predivisional class of cells was distinguished by four ultrastructural differences: (1) The most obvious difference was the partial division of the chloroplast along a line approximately perpendicular to the boundary between the nucleus and chloroplast, setting up an apparent roughly two fold-symmetric division plane (Figure III-1C-D, 5C, 5D, and 6C). In most of the predivisional cells (62%), there was a space between the chloroplast and the plasma membrane filled with either ribosome-like complexes or the mitochondria (Figure III-4A), as if the forces positioning the chloroplast immediately next to the membrane in G_1 were weakened. (2) The nucleus was no longer oval. In some cases the nucleus was wedge-shaped, protruding into the middle of the dividing chloroplast (Figure III-1C-D). In twelve other cases (46%) the NE formed extensions that streamed above/below the chloroplast, sometimes accompanied by the Golgi body or microtubule (Figure III-4A-B). (3) Whereas in G_1 the mitochondrion appeared to be randomly positioned, in dividing cells at least part of it consistently crossed the apparent division plane. In some cases it seemed to be straddling the division plane (Figure III-1C-D), in others it was elongated as if at least one edge were being drawn to the division plane (Figure III-4C). (4) The oval storage granules lined up in a symmetric "V" shape across the division plane pointing towards the chloroplast with the tip of the "V" located at the cell's center (Figure III-5D).

Chloroplasts

The chloroplast was the largest organelle and since it was also one of the most dense, its internal structure was the most difficult to resolve. Due to the missing wedge artifact, thylakoid grana that may have been present at the top and bottom of the chloroplast could not be resolved. In the midsection, grana composed of three disks (six membranes) hugged the inner chloroplast membrane and sometimes extended into the middle of the chloroplast as broad sheets without connecting stroma-like thylakoid structures (Figure III-5A-B). Because the lumens of the two outer disks (about 7 nm across) were consistently wider than that of the central disk, the grana had a sandwich-like appearance: the "top" and "bottom" membranes of the stack stood apart from the inner four, which were packed so tightly that they were often hard to distinguish. The grana thylakoids terminated at the poles of the long axis of the chloroplast (Figure III-5 A-B), but the connectivity of the individual membranes and the details of the presumed organizing scaffold were unclear. No connections or vesicles between the grana thylakoids and the inner chloroplast membrane were seen.

The chloroplasts contained two distinct classes of granules. Each chloroplast had multiple dark and very nearly spherical granules (Figure III-5, white arrowheads) and a single larger granule that manifested electron beam damage artifacts (bubbling) much earlier than the rest of the cell (Figure III-5, white arrows). Radiation-sensitive granules have also been reported in the gram-negative bacterium *Caulobacter crescentus*, and were found to be carbon-rich (Comolli and Downing, 2005). The “bubbled” granule was seen stretched across the division plane in dividing chloroplasts, as expected for the starch granule, which was previously shown to exist as one copy that grew and divided

(Ral et al., 2004). The onset of bubbling in the granule occurred at ~ 100 electrons/Å^2, since in the cases of those cells where dual-axis tilt-series were recorded, reconstructions obtained from just the first half of the data (the first tilt ~ 80 electrons/Å^2) did not show bubbling. (The higher total doses were used, however, because they led to reconstructions with more interpretable detail, indicating that the perturbations to the rest of the cellular ultrastructure caused by bubbling in the presumed starch granule were minor in comparison to the advantages of higher dose.) The chloroplasts divided along the apparent cellular division plane (Figure III-5C-D, 6C). Each half of dividing chloroplasts contained a portion of the presumed starch granule and at least one dark granule. No completely divided chloroplasts were observed, suggesting that cell division quickly followed the termination of chloroplast division.

In agreement with the likely evolutionary relationship between chloroplasts and cyanobacteria, the ultrastructure of the *O. tauri* chloroplasts was reminiscent of cyanobacteria. Both thylakoid systems are comprised almost exclusively of grana (Nevo et al., 2007; van de Meene et al., 2006), positioned near the inner chloroplast membrane and near the analogous plasma membrane in cyanobacteria. The chloroplasts also appeared to replicate like cyanobacteria, since their thylakoids were present before division and must have been pinched off at the nascent poles. In contrast, higher plant chloroplasts mature from progenitor proplastids that lack differentiated internal membranes.

Traditional models depict the lumens of thylakoid disks as discreet from the lumen between the chloroplast's inner and outer membranes (Vothknecht and Westhoff, 2001). A recent tomogram of a higher-plant chloroplast supports this traditional

"detached" thylakoids model (Shimoni et al., 2005). Van de Meene et al., showed a cyanobacteria's thylakoid contacting the inner plasma membrane, however, but the nature of the connection could not be determined (van de Meene et al., 2006). Here *O. tauri* thylakoids appeared detached, but unfortunately the complete chloroplast could not be clearly observed, transient events might not have been captured, and the details of the presumed organizing scaffolding could not be resolved. No transport mechanisms for bringing required lipids to a growing thylakoid, such as vesicles between the inner membrane and thylakoid stacks, were detected.

Nuclei

Higher eukaryotes undergo open mitosis, resulting in the partial or complete breakdown of the NE. The onset of mitosis is marked by NE breakdown, NPC disassembly, and mitotic spindle formation. The NE re-forms on the chromosomes during metaphase and completely closes after telophase (Drummond et al., 2006). In contrast, model lower eukaryotes like yeast undergo closed mitosis, in which the NE remains intact. Our reconstructions reveal that *O. tauri*'s NEs are almost always open, and other mitotic events differ substantially from traditional models.

Throughout the cell cycle the NE had gaps hundreds of nanometers in diameter (Figure III-6B, arrows). In fact only one cell was observed with an apparently closed NE (Figure III-6A). This small cell was taken from a culture at the light-to-dark transition, and its non-dividing organelles implied that it must have just divided and was in early G_1. This cell could have had gaps in the top and bottom of the NE, but we could not verify this due to the effects of the missing wedge. Other cells imaged that were also

presumably in early G_1 were found to have an open NE. The openings in the NE consistently faced the cytoplasmic space between the nucleus and the chloroplast; the regions facing the plasma membrane were generally closed. In certain rare cases, the nucleus was almost completely unbounded by NE (Figure III-6C and 1E). In these cells large fragments of NE were seen along the borders of a recognizably dense nucleoplasm, implying that the nucleoplasm is gel-like and able to retain its unique composition.

Near the plasma membrane, the outer and inner NE membranes were too close to be resolved. Elsewhere, these membranes were spaced between 18 and 100 nm apart. NPCs were present (discussed below). As noted previous, in 42% of the predivisional cells, protrusions of the nucleus streamed over the top of the chloroplast (Figure III-4A-B). Unfortunately no internal structures (like heterochromatin, nuclear lamina, or condensed chromosomes) were recognized.

Many higher eukaryotes undergo NE breakdown during mitosis, so the fact that a cell can have a NE with large gaps is reasonable. Nevertheless *O. tauri*'s NE appeared to be open during most of the cell cycle (from the beginning to the end of the light cycle). This is significant because presumably, the nucleus must be closed in order to establish the Ran nucleo-cytoplasmic gradient, which shuttles cargo in and out of the nucleus via the NPCs. The NE had such large gaps that the role of the NPCs is unclear, although they remained embedded in the NE fragments. Perhaps certain molecules like mRNAs require regulated transport and so are specifically targeted to the NPC. Despite being open, at least many of the nuclei must have been transcriptionally and translationally active since the cells were in the exponential growth phase and ribosomes consistently decorated parts of the NE.

Previously published EM images of *O. tauri* do not suggest the existence of gaps in the NE (Farinas et al., 2006). With conventional EM, however, in some cases membranes can be severely distorted and each image generally shows just a thin section through the nucleus (Figure III-S1). Because ECT offers 3-D views of near-native structures, the gaps were quite clear.

Nuclear Pore Complexes

NPCs within the NE were identified as ~ 80 nm diameter rings of high electron density, bordered by a region of the NE where the outer and inner membranes merged (Figure III-7). Each cell had one to three visible NPCs, but there may have been additional NPCs within the top or bottom faces of the nuclei that were not recognized because of the missing wedge. As mentioned earlier, the nuclei were immediately adjacent to the plasma membrane, but the NPCs were never found facing that membrane. Instead, the NPCs were found in regions of the NE exposed to the cell's interior, but the mechanisms localizing the NPCs remain unclear. In the four best resolved NPCs, the average "outer" diameter of the rings (where the outer and inner bilayers of the NE could no longer be distinguished, Figure III-7, solid lines) was 81±4 nm. The average "inner" diameter of the high-density ring (Figure III-7, dashed lines) was 48±8 nm; the greater variance being due perhaps to the uncertainty in locating the inner boundary. Other internal densities were seen which may represent cargo, “transporters,” or luminal spoke rings (Akey and Radermacher, 1993).

While these may be the first measurements of NPCs *in vivo*, or of plant or algal NPCs in any state, the *O. tauri* NPCs observed here were smaller (81 nm) than those

from *Dictyostelium* (125 nm), *Xenopus* (100 nm), or *Saccharomyces* (100 nm) (Beck et al., 2004; Stoffler et al., 2003; Yang et al., 1998). Unfortunately the resolution was insufficient to detect the symmetry, as was done for isolated *Dictyostelium* nuclei (Beck et al., 2004), so it is unclear whether the smaller size results from smaller or fewer constituent proteins. Compared to the *Dictyostelium* NE (the only other intact nucleus imaged by cryotomography), which has such a high concentration of NPCs (~ 45 / μm^2) that they exhibit local hexagonal packing (Beck et al., 2004; Yang et al., 1998), *O. tauri* NE had a much lower NPC concentration (~ 1 / μm^2).

Mitochondria

Each cell had a single mitochondrion. The mitochondria were generally oval (Figure III-8), but were frequently deformed when situated adjacent to other organelles. In some dividing cells the mitochondria were elongated (Figure III-4C) or constricted in their center (Figure III-1C-D). The inner and outer membranes were smooth rather than corrugated as sometimes observed by traditional EM (Perkins et al., 1997). While the spacing between the inner and outer membrane was generally ~ 12 nm (Figure III-8C-D), it was sometimes significantly greater (top of Figure III-8B), or so small that the inner and outer membranes appeared to touch (Figure III-8E). The mitochondria positioned near the thinner edges of cells were the best resolved and exhibited both lamellar and tubular cristae, typically with one or two junctions with the inner membrane (arrowheads in Figure III-8B-D). These crista junctions were circular or slot-shaped and ranged in size from 15–55 nm. The spacing between the two membranes of the cristae was also 15

nm or greater. In some mitochondria (40%), multiple (4-10) dark granules with complex shapes were observed in the matrix (Figure III-8A-B).

Electron tomographic reconstructions of mitochondria have already discredited the baffle model of membrane folding, where cristae were proposed to fold in much like the bellows of an accordion. Instead, both isolated and *in-situ* mitochondria have been shown to have tubular and laminar cristae that connect to the inner membrane by circular or slot-shaped crista junctions (Mannella et al., 1994; Nicastro et al., 2000). Our observations in *O. tauri* add to this body of literature and highlight the consistency of mitochondrial ultrastructure. Notwithstanding the evolutionary pressures that shrunk *O. tauri* and its mitochondria, the arrangement of its cristae has essentially not changed. This strengthens the idea that the structure of the cristae plays an important role in oxidative phosphorylation, including the possibility that it creates local environments separated by bottlenecks of restricted diffusion (Mannella et al., 2001; Mannella, 2006a, b).

Endoplasmic Reticula

Sheets and tubes of membranes branching off the NE were identified as ER (Figure III-6B, white arrowheads). The inter-membrane spacing within each ER sheet ranged from 14 nm to 80 nm. The ER tubes had diameters of ~ 14 nm — a value much smaller than the 25–100 nm typically described for smooth ER (Shibata et al., 2006; Staehelin, 1997). Interestingly, some ER sheets were perforated by the dark oval granules (Figure III-6B and 9). Other structures looked just like the ER, but connections to the NE were not found. These consisted of sheets that were found adjacent to the

plasma membrane and at the four regions that projected extra-cellular filaments, as discussed later (Figure III-13B, arrows).

Current descriptions of ER ultrastructure assert the notions that (1) the lumens of different ER sheets are interconnected with each other and with the NE lumen, and (2) rough ER forms sheets and all other ER (smooth ER) is tubular (Shibata et al., 2006; Staehelin, 1997). *O. tauri*'s ER differed in both these characteristics. While some ER tubes and sheets appeared to be contiguous with the NE, others had no observable connection. Rapid fission and fusion of membranes can make compartments functionally interconnected, like the Golgi body's many cisternae, but our "snapshots" of flash-frozen cells suggest that some ER compartments are physically isolated at least part of the time. Less likely but still possibly, connections might have existed but were not observed due to the missing wedge artifact or limits in resolution. Surprisingly, while clusters of ribosome-like particles were found on the cytoplasmic face of the outer nuclear membrane, no ribosome-decorated ER (rough ER) could be found. This contradicts earlier speculations that ribosomes are necessary to maintain the ER's flat shape (Shibata *i*, 2006; Voeltz et al., 2006).

Golgi bodies

Golgi bodies were identified as stacks of flat, membranous cisternae positioned next to the nucleus and usually extending towards the chloroplast. No cell had more than one Golgi body, but in some cells (23%, including both non-dividing and predivisional) no Golgi body was found, probably because it was positioned in such a way that the missing wedge artifacts made it impossible to recognize. In mammalian cells the Golgi

body disperses prior to cell division (Gaietta et al., 2006); here the Golgi was frequently observed in predivisional *O. tauri*.

In *O. tauri*, the Golgi bodies typically consisted of five uniformly spaced cisternae (Figure III-10A-B). Some Golgi bodies exhibited up to seven cisternae, but the extra cisternae were often not consistently spaced or appeared as if they were beginning to leave (Figure III-10C, dark blue). The NE was used to determine cis to trans direction because the resolution was insufficient to resolve the protein coats on the vesicles that are normally used to determine the Golgi polarity. Most cisternae were roughly disk shaped (Figure III-10A-B), but more elongated cisternae were also seen (Figure III-10C). All were slightly curved. The cisterna nearest the nucleus was consistently the smallest, with a diameter and volume of about 150 nm and 5 x 10^{-8} pL, respectively. Its concave (cis) surface faced towards the nucleus. The middle three cisternae were larger, measuring 200 nm in diameter and 7.5 x 10^{-8} pL in volume. The trans-cisterna was 200 nm in diameter and thinner, having a volume similar to the cis-cisterna. None of the cisternae were connected.

The origins and destinations of vesicles in the Golgi are of considerable interest (Storrie and Nilsson, 2002). From the nucleus outwards, occasionally vesicles were seen budding out of the NE towards the cis cisternae (8% of cells). There were also free-standing vesicles observed between the NE and cis cisternae. The tubular vesicles in front of the cis-surface (Figure III-10, light blue) might have been the fusion of two or more NE-derived vesicles that formed a vesicular tubular cluster. Vesicles were not seen between cisternae, but they were frequently present along the sides of the stacks. The trans-cisterna often abutted the chloroplast, leaving no room for vesicles trans to the

cisterna. No vesicles were ever found trans to the Golgi body, but the trans-cisterna often had an appearance of slipping off the stack (Figure III-10A-B, green cisternae), and occasionally had an additional cisterna beyond it (Figure III-10C, dark blue cisterna). Vesicles were not observed between the Golgi body and the non-nuclear ER.

These observations are consistent with the maturation model of Golgi body transport, but the lack of trans vesicles is surprising. Some of the vesicles along the side of the Golgi body could have originated from the trans surface and moved off to the side, sterically deflected by the chloroplast. It may also be possible that instead of having many small trans vesicles, here at least Figure III-10C suggests that the entire trans-cisternae (dark blue) is one transport vesicle. Many cells rely on microtubules to transport Golgi associated vesicles (Caviston and Holzbaur, 2006), but as in *Schizosaccharomyces pombe* (Hoog et al., 2007), no microtubules were ever found contacting the Golgi body or its neighboring vesicles. Perhaps other, smaller cytoskeletal filaments were present to guide vesicles but were not resolved in our reconstructions.

Vesicles

A variety of vesicles were seen. The most numerous type (1-10 or more per cell) were pleomorphic, typically ~200 nm diameter, and occurred in clusters sometimes configured as a "V" in predivisional cells (Figure 1, 3, 4, 5, 9). Their high internal density prevented us from determining if there was a surrounding membrane. Presumably these are some type of storage granule. Smaller vesicles were also seen whose size and random locations suggest they could have been involved in transport. In addition to these storage and transport vesicles, all the cells (n = 52) contained at least

one characteristically low-density, nearly spherical, second type of vesicle surrounded by a single membrane (Figure III-3B and F, 9) measuring 166 ± 20 nm in diameter. Some dividing cells had two. Remarkably, these special vesicles were almost always in contact with both the chloroplast and the nucleus (Figure III-9), even when they were found far from the main body of the nucleus. In these cases they were found touching long, thin extensions of the NE streaming over the chloroplast (Figure III-4A), suggesting connections to both the NE and chloroplast. Because (i) peroxisomes have been described as single-membraned vesicles, (ii) small *O. tauri* cells are likely to need one and only one peroxisome but multiple storage granules, and (iii) *Ostreococcus* genomes contain peroxisomal genes (Palenik et al.), these vesicles were assumed to be peroxisomes. As dividing peroxisomes were never seen, perhaps *O. tauri* only produces peroxisomes *de novo* (Hoepfner et al., 2005; Mullen and Trelease, 2006; Purdue and Lazarow, 2001).

Microtubules

Most *O. tauri* cells had a single, hollow, tubular structure 24±1 nm wide and 200–700 nm long assumed here to be a microtubule. The microtubule always rested between the outer nuclear membrane and the plasma membrane against one of the "top" or "bottom" flat faces of the cell (Figure III-3, purple rods). Both ends of the microtubule were open and blunt (Figure III-11, arrowheads). The microtubules were slightly curved and near one end the shaft made contact with the NE, but the resolution was insufficient to discern whether bridging proteins connected the two (Figure III-11B, insert). There was neither an obvious microtubule organizing center nor a flared or capped end to

conclusively identify the minus or plus end, respectively. It is possible that the microtubules are organized similarly to those of higher plants, in which the minus end interacts closely with the NE (as discussed later).

Surprisingly, none of the cells exhibited a mitotic spindle, even though many stages of division were seen, and microtubules were consistently resolved in our reconstructions. Unlike metazoans and yeast, plants lack a structurally distinct microtubule organizing center, but their NEs do organize mitotic spindles that segregate their chromosomes (Stoppin et al., 1994). Three of the reconstructed *O. tauri* cells had two microtubules, and in one of these cells they were partially embedded within the open nucleus (the cell in Figure III-6C, though the microtubules are not present in the slice shown), but because *O. tauri* has 20 independent linear chromosomes (Derelle et al., 2006), a canonical mitotic spindle would have been expected to have more than 40 microtubules. While it is possible that in *O. tauri* the spindle appears so transiently that by chance none of the 26 predivisional cells reconstructed here contained one, its absence suggests the intriguing possibility that some evolutionary pressure (like size minimization) has caused *O. tauri* to adapt a novel mechanism for chromosome segregation. Perhaps the twenty pairs of chromosomes are segregated one at a time by the two mitotic microtubules. Alternatively, the chromosomes may be physically linked during mitosis and be co-segregated.

Ribosome-like complexes

The cytoplasm contained many discrete large macromolecular complexes, which were presumably mostly ribosomes. The cytoplasms of three non-dividing cells (D, E,

and F in Figure III-3) were searched by cross-correlation for ribosome-like particles using a low-pass-filtered ribosome model as template. Visual inspection of the search results using different thresholds showed the search had located large protein complexes within the cytoplasm, but as expected, there was no clear cutoff in the distribution of cross-correlation coefficients that could distinguish between ribosomes and other large particles (Figure III-S2). Moreover, because the peak-search algorithm excluded adjacent peaks closer together than a ribosome diameter, clustered complexes were not accurately parsed. Nevertheless because a threshold of the top 500 picks clearly excluded many large protein complexes and a threshold of 2000 clearly included many smaller complexes (Figure III-12A), we conclude that there were very roughly about 1250 ribosomes per cell. In comparison, exponentially growing *Saccharomyces cerevisiae* cells have ~ 200,000 ribosomes each (Warner, 1999). Since *S. cerevisiae* cells have up to 150 times more cytoplasm than *O. tauri* (Johnston et al., 1979; Zadrag et al., 2006), the concentration of ribosomes in these cells is approximately the same. In *O. tauri*, the ribosomes appeared to be uniformly distributed within the cytoplasm (Figure III-12B).

Plasma Membrane Extensions and Surface Proteins

Three cells (6%) exhibited a bulge containing multiple 5 nm diameter filaments (Figure III-13A) near sheets of ER. Two other much longer plasma membrane extensions were observed at opposite poles of an unusual cell (Figure III-1E-F). One extension was at least 585 nm long (continued to the edge of the reconstructed area) and contained two internal filaments while the other was much shorter and contained a "Y" shaped inner vesicle protruding into the extension. Large proteins were also seen

decorating the outer surface of cells (Figure III-13B). While these various specializations likely mediate contacts with other cells or substrates, their functions and mechanisms are of course at this point unclear.

Conclusion

Despite application of all the best imaging technologies available, many fundamentally important aspects of eukaryotic ultrastructure remain elusive (including for instance, as a single example, the higher-order structure of chromatin). This study demonstrated that the emerging technique ECT can reveal the detailed ultrastructure of at least the smallest known eukaryotic cell, *O. tauri*, in an intact and near-native state. While ECT has already been applied to purified mitochondria and nuclei (Beck et al., 2004; Nicastro et al., 2000), here they were seen in their cellular context along with structures that cannot be isolated (like the Golgi). Because *O. tauri* is becoming an increasingly well-developed model system as a simple plant and "minimal" eukaryotic cell, systematic high-resolution ultrastructural analysis by ECT as done here (but also of cells stalled in specific states and interesting mutants) will likely provide key insights into the organization of cells and the molecular mechanisms responsible. As examples, here we have seen that in G_1, the nucleus and chloroplast sit opposite one another, and this may simply be because they are the largest bodies within the size-minimizing cell. While the mitochondrion seems to position itself randomly, the other major organelles appear to be organized by their relationship to the NE. The chloroplast exhibited its own division plane, and thus must possess its own segregation machinery for its internal features.

Nevertheless the resolution was limited in both space and time. As one benchmark example, while microtubules were easily resolved here, actin filaments were not, though that has been possible in other thinner specimens (Briegel et al., 2006; Henderson and Jensen, 2006; Komeili et al., 2006; Kurner et al., 2005; Medalia et al., 2002; Scheffel et al., 2006). Thus it remained unclear, for instance, what the molecular mechanisms were that established the division plane or segregated the different copies of each organelle. While future technological advances in both instrumentation and specimen preparation can be expected to improve the situation soon (Jensen and Briegel, 2007), it is unclear now which of *O. tauri*'s eukaryotic secrets will be the most interesting! Our original hope of visualizing undisturbed chromatin and mitosis in molecular detail, for instance, has been replaced by intrigue over the possibility that *O. tauri* may have remarkable and unique adaptations, since the nuclear envelope was wide open throughout most of the cell cycle and neither condensed chromosomes nor a mitotic spindle were ever seen. While it is possible that these expected features exist so briefly that we simply missed them in our sampling of 52 frozen cells, it is also possible that *O. tauri* will reveal significantly simplified mitotic mechanisms.

Materials and methods

Cell growth. *Ostreococcus tauri* strain OTH95 (RCC 745 from the Roscoff Culture Collection) was grown in f/2 medium (Guillard, 1975) made with Sigma Sea Salt to 36% salinity. Cells were grown at a constant 20 °C with gentle, 60 RPM agitation on a rotary shaker in a cycle of twelve hours of light and twelve hours of dark.

Traditional Fixation. *O. tauri* cells were harvested during early and mid exponential growth phase, and concentrated by 5,000 RCF centrifugation. The cell pellet was then mixed with a 1% glutaraldehyde made up in filtered ocean water. The cells were re-centrifuged, washed twice with cacodylate buffer, and fixed in 1% OsO4 for 30 minutes. The cells were re-washed twice with cacodylate buffer, washed with 30% ethanol for 10 minutes, and then mixed with 30% ethanol and 4% uranyl acetate for 20 minutes. Finally cells were then successively dehydrated with a series of ethanol washes and embedded in Epon.

High-pressure fixation and freeze substitution. Cells were harvested by centrifugation as above. The cell pellet was high pressure-frozen in a BAL-TEC HPM 010 freezer (BAL-TEC, Liechtenstein). The samples were freeze substituted with 1% osmium tetroxide and 0.1% uranyl acetate in acetone using an EM AFS (Leica, Vienna). Samples were held at - 90°C for 18 hours, warmed to -25 °C at a rate of 5 °C/hr, held at -25 °C for 12 hours, then warmed to room temperature at a rate of 5 °C/hr. The samples were then rinsed in pure acetone, infiltrated and embedded in Epon-Araldite resin.

Plunge Freezing. Cells were harvested by centrifugation as above, then resuspended, and combined with 10 nm gold fiducial markers. This sample was applied to glow-discharged R 2/2 Quantifoil grids (SPI Supplies), excess media was removed by a single 1 s blot (-4 mm offset, 1 s drain time), and vitrified by plunging into liquid ethane in a Vitrobot (FEI) (Iancu et al., 2006).

Electron cryotomography. Plunge-frozen grids were loaded into "flip-flop" tilt rotation holders (Iancu et al., 2005) and imaged in a 300 keV, FEG, G2 Polara transmission electron microscope (FEI) equipped with an energy filter (Gatan). Throughout loading and imaging, samples were cooled with liquid nitrogen (Wright et al., 2006). Sequentially tilted, energy-filtered (slit width 20 eV) images of individual cells were collected automatically using either the UCSF tomography (Zheng et al., 2004) or Leginon software packages (Suloway et al., 2005) in 2˚ increments up to +/- ~56-60˚ along either one (36 cells) or two (16 cells) axes (Iancu et al., 2005) at 18,000x magnification, resulting in a CCD pixel size of 1.2 nm. The cumulative dose for each tilt series was 165 $e^-/Å^2$.

Image processing. Images were aligned using the gold fiducials and three-dimensional reconstructions were calculated and visualized using the IMOD software package (Mastronarde, 1997). Reconstructions were denoised using thirty cycles of non-linear anisotropic diffusion with parameter lambda = 0.3 (Frangakis and Hegerl, 2001) using Bsoft (Heymann and Belnap, 2006) and the Peach distributed-computing system (Leong et al., 2005). Denoised 3-D reconstructions were manually segmented using the Amira

software package (Mercury Computer System, Inc.) on a Wacom Cintiq 21UX display. Volume and surface area estimates of the segmented volumes were also made using Amira. Cross-correlation searches were done using the MolMatch software (Frangakis et al., 2002) and an appropriately scaled and low pass-filtered cryo-EM reconstruction of a ribosome (Spahn et al., 2001) as template. Cytoplasmic peaks were ranked based upon cross-correlation coefficients and then displayed using Amira.

Acknowledgements

We thank Hervé Moreau (Observatoire Océanologique, Laboratoire Arago) and Brian Palenik (Scripps Institution of Oceanography) for helping us obtain and work with *O. tauri* cultures and for reading the manuscript, Kent L. McDonald (U.C. Berkeley) for help high-pressure freezing, Wolfgang Baumeister's group (Max Planck Institute for Biochemistry) for the most current version of the MolMatch software, Andrea Manuell for discussions on the chloroplast, Christian Suloway (Caltech) for assistance with Leginon, and Jane Ding (Caltech) for help running the cross-correlation search on the supercomputer. This work was supported in part by NIH grants R01 AI067548 and PO1 GM66521 and DOE grant DE-FG02-04ER63785 to GJJ, a Searle Scholar Award to GJJ, the Beckman Institute at Caltech, and gifts to Caltech from the Gordon and Betty Moore Foundation and Agouron Institute. Lu Gan was supported by a fellowship from the Damon Runyon Cancer Research Foundation (DRG-1940-07).

References

Akey, C.W., and Radermacher, M. (1993) Architecture of the Xenopus nuclear pore complex revealed by three-dimensional cryo-electron microscopy. *J Cell Biol* **122**: 1-19.

Al-Amoudi, A., Chang, J.J., Leforestier, A., McDowall, A., Salamin, L.M., Norlen, L.P., Richter, K., Blanc, N.S., Studer, D., and Dubochet, J. (2004) Cryo-electron microscopy of vitreous sections. *Embo J* **23**: 3583-3588.

Beck, M., Forster, F., Ecke, M., Plitzko, J.M., Melchior, F., Gerisch, G., Baumeister, W., and Medalia, O. (2004) Nuclear pore complex structure and dynamics revealed by cryoelectron tomography. *Science* **306**: 1387-1390.

Briegel, A., Dias, D.P., Li, Z., Jensen, R.B., Frangakis, A.S., and Jensen, G.J. (2006) Multiple large filament bundles observed in Caulobacter crescentus by electron cryotomography. *Mol Microbiol* **62**: 5-14.

Caviston, J.P., and Holzbaur, E.L. (2006) Microtubule motors at the intersection of trafficking and transport. *Trends Cell Biol* **16**: 530-537.

Chrétiennot-Dinet, M.J., Courties, C., Vaquer, A., Neveux, J., Claustre, H., Lautier, J., and Machado, M.C. (1995) A new marine picoeucaryote: Ostreococcus tauri gen. et sp. nov. (Chlorophyta, Prasinophyceae). *Phycologia* **34**: 285-292.

Comolli, L.R., and Downing, K.H. (2005) Dose tolerance at helium and nitrogen temperatures for whole cell electron tomography. *J Struct Biol* **152**: 149-156.

Courties, C., Vaquer, A., Troussellier, M., Lautier, J., Chrétiennot-Dinet, M.-J., Neveux, J., Machado, C., and Claustre, H. (1994) Smallest eukaryotic organism. *Nature* **370**: 255.

Courties, C., Perasso, R., Chrétiennot-Dinet, M.J., Gouy, M., Guillour, L., and Troussellier, M. (1998) Phylogenetic Analysis and Genome Size of Ostreococcus tauri (Chlorophyta, Prasinophyceae). *J Phycology* **34**: 844-849.

Derelle, E., Ferraz, C., Rombauts, S., Rouze, P., Worden, A.Z., Robbens, S., Partensky, F., Degroeve, S., Echeynie, S., Cooke, R., Saeys, Y., Wuyts, J., Jabbari, K., Bowler, C., Panaud, O., Piegu, B., Ball, S.G., Ral, J.P., Bouget, F.Y., Piganeau, G., De Baets, B., Picard, A., Delseny, M., Demaille, J., Van de Peer, Y., and Moreau, H. (2006) Genome analysis of the smallest free-living eukaryote Ostreococcus tauri unveils many unique features. *Proc Natl Acad Sci U S A* **103**: 11647-11652.

Drummond, S.P., Rutherford, S.A., Sanderson, H.S., and Allen, T.D. (2006) High resolution analysis of mammalian nuclear structure throughout the cell cycle: implications for nuclear pore complex assembly during interphase and mitosis. *Cana J Physiol Pharmacol* **84**: 423-430.

Dubochet, J., Adrian, M., Chang, J.J., Homo, J.C., Lepault, J., McDowall, A.W., and Schultz, P. (1988) Cryo-electron microscopy of vitrified specimens. *Q Rev Biophys* **21**: 129-228.

Farinas, B., Mary, C., de O Manes, C.L., Bhaud, Y., Peaucellier, G., and Moreau, H. (2006) Natural Synchronisation for the study of cell division in the green unicellular alga Ostreococcus tauri. *Plant Mol Biol* **60**: 277-292.

Frangakis, A.S., and Hegerl, R. (2001) Noise reduction in electron tomographic reconstructions using nonlinear anisotropic diffusion. *J Struct Biol* **135**: 239-250.

Frangakis, A.S., Bohm, J., Forster, F., Nickell, S., Nicastro, D., Typke, D., Hegerl, R., and Baumeister, W. (2002) Identification of macromolecular complexes in cryoelectron tomograms of phantom cells. *Proc Natl Acad Sci U S A* **99**: 14153-14158.

Gaietta, G.M., Giepmans, B.N., Deerinck, T.J., Smith, W.B., Ngan, L., Llopis, J., Adams, S.R., Tsien, R.Y., and Ellisman, M.H. (2006) Golgi twins in late mitosis revealed by genetically encoded tags for live cell imaging and correlated electron microscopy. *Proc Natl Acad Sci U S A* **103**: 17777-17782.

Grimm, R., Barmann, M., Hackl, W., Typke, D., Sackmann, E., and Baumeister, W. (1997) Energy filtered electron tomography of ice-embedded actin and vesicles. *Biophys J* **72**: 482-489.

Guillard, R.R. (1975) Culture of phytoplankton for feeding marine invertebrates. In *Culture of marine invertebrate animals*. Smith, W., and Chanley, M. (eds.). New York, New York: Plenum Publishing Corporation, pp. 29-53.

Henderson, G.P., and Jensen, G.J. (2006) Three-dimensional structure of Mycoplasma pneumoniae's attachment organelle and a model for its role in gliding motility. *Mol Microbiol* **60**: 376-385.

Heymann, J.B., and Belnap, D.M. (2006) Bsoft: Image processing and molecular modeling for electron microscopy. *J Struct Biol* **157**: 3-18.

Hoepfner, D., Schildknegt, D., Braakman, I., Philippsen, P., and Tabak, H.F. (2005) Contribution of the endoplasmic reticulum to peroxisome formation. *Cell* **122**: 85-95.

Hoog, J.L., Schwartz, C., Noon, A.T., O'Toole, E.T., Mastronarde, D.N., McIntosh, J.R., and Antony, C. (2007) Organization of interphase microtubules in fission yeast analyzed by electron tomography. *Dev Cell* **12**: 349-361.

Iancu, C.V., Wright, E.R., Benjamin, J., Tivol, W.F., Dias, D.P., Murphy, G.E., Morrison, R.C., Heymann, J.B., and Jensen, G.J. (2005) A "flip-flop" rotation stage for routine dual-axis electron cryotomography. *J Struct Biol* **151**: 288-297.

Iancu, C.V., Tivol, W.F., Schooler, J.B., Dias, D.P., Henderson, G.P., Murphy, G.E., Wright, E.R., Li, Z., Yu, Z., Briegel, A., Gan, L., He, Y., and Jensen, G.J. (2006) Electron cryotomography sample preparation using the Vitrobot. *Nat Protoc* **1**: 2813-2819.

Jensen, G.J., and Briegel, A. (2007) How electron cryotomography is opening a new window onto prokaryotic ultrastructure. *Curr Opin Struct Biol* **17**: 260-267.

Johnston, G.C., Ehrhardt, A., Lorincz, A., and Carter, B.L. (1979) Regulation of cell size in the yeast Saccharomyces cerevisiae. *J Bacteriol* **137**: 1-5.

Komeili, A., Li, Z., Newman, D.K., and Jensen, G.J. (2006) Magnetosomes are cell membrane invaginations organized by the actin-like protein MamK. *Science* **311**: 242-245.

Kurner, J., Frangakis, A.S., and Baumeister, W. (2005) Cryo-electron tomography reveals the cytoskeletal structure of Spiroplasma melliferum. *Science* **307**: 436-438.

Leong, P.A., Heymann, J.B., and Jensen, G.J. (2005) Peach: a simple Perl-based system for distributed computation and its application to cryo-EM data processing. *Structure* **13**: 505-511.

Lucic, V., Forster, F., and Baumeister, W. (2005) Structural studies by electron tomography: from cells to molecules. *Annu Rev Biochem* **74**: 833-865.

Mannella, C.A., Marko, M., Penczek, P., Barnard, D., and Frank, J. (1994) The internal compartmentation of rat-liver mitochondria: tomographic study using the high-voltage transmission electron microscope. *Microsc Res Tech* **27**: 278-283.

Mannella, C.A., Pfeiffer, D.R., Bradshaw, P.C., Moraru, I.I., Slepchenko, B., Loew, L.M., Hsieh, C., Buttle, K., and Marko, M. (2001) Topology of the mitochondrial inner membrane: dynamics and bioenergetic implications. *IUBMB Life* **52**: 93-100.

Mannella, C.A. (2006a) Structure and dynamics of the mitochondrial inner membrane cristae. *Biochim Biophys Acta* **1763**: 542-548.

Mannella, C.A. (2006b) The relevance of mitochondrial membrane topology to mitochondrial function. *Biochim Biophys Acta* **1762**: 140-147.

Marko, M., Hsieh, C., Schalek, R., Frank, J., and Mannella, C. (2007) Focused-ion-beam thinning of frozen-hydrated biological specimens for cryo-electron microscopy. *Nat Methods* **4**: 215-217.

Mastronarde, D.N. (1997) Dual-axis tomography: an approach with alignment methods that preserve resolution. *J Struct Biol* **120**: 343-352.

McDonald, K.L., and Auer, M. (2006) High-pressure freezing, cellular tomography, and structural cell biology. *Biotechniques* **41**: 137-143.

Medalia, O., Weber, I., Frangakis, A.S., Nicastro, D., Gerisch, G., and Baumeister, W. (2002) Macromolecular architecture in eukaryotic cells visualized by cryoelectron tomography. *Science* **298**: 1209-1213.

Mullen, R.T., and Trelease, R.N. (2006) The ER-peroxisome connection in plants: development of the "ER semi-autonomous peroxisome maturation and replication" model for plant peroxisome biogenesis. *Biochim Biophys Acta* **1763**: 1655-1668.

Nevo, R., Charuvi, D., Shimoni, E., Schwarz, R., Kaplan, A., Ohad, I., and Reich, Z. (2007) Thylakoid membrane perforations and connectivity enable intracellular traffic in cyanobacteria. *EMBO J* **26**: 1467-1473.

Nicastro, D., Frangakis, A.S., Typke, D., and Baumeister, W. (2000) Cryo-electron tomography of neurospora mitochondria. *J Struct Biol* **129**: 48-56.

Palenik, B., Grimwood, J., Aerts, A., Rouze, P., Salamov, A., Putnam, N., Dupont, A., Jorgensen, R., Derelle, E., Rombauts, G., Zhuo, K., Otillar, R., Merchant, S.S., Podell, S., Gaasterland, T., Napoli, C., Gendler, K., Manuell, K., Tai, V., Vallon, O., Piganeau, G., Jancek, F., Heijde, M., Jabbari, K., Bowler, C., Lorh, L., Robbens, S., Werner, G., Dubchak, I., Pazour, G.J., Ren, Q., Paulsen, I., Delwiche, P., Schmutz, J., Rokhsar, D., Van de Peer, Y., Moreau, H., and Grigoriev, I.V. The tiny eurkaryote Ostreococcus provides genomic insights into the paradox of plankton speciation. *Proc Natl Acad Sci U S A*.

Perkins, G., Renken, C., Martone, M.E., Young, S.J., Ellisman, M., and Frey, T. (1997) Electron tomography of neuronal mitochondria: three-dimensional structure and organization of cristae and membrane contacts. *J Struct Biol* **119**: 260-272.

Purdue, P.E., and Lazarow, P.B. (2001) Peroxisome biogenesis. *Annu Rev Cell Dev Biol* **17**: 701-752.

Ral, J.P., Derelle, E., Ferraz, C., Wattebled, F., Farinas, B., Corellou, F., Buleon, A., Slomianny, M.C., Delvalle, D., d'Hulst, C., Rombauts, S., Moreau, H., and Ball, S. (2004) Starch division and partitioning. A mechanism for granule propagation and maintenance in the picophytoplanktonic green alga Ostreococcus tauri. *Plant Physiol* **136**: 3333-3340.

Robbens, S., Khadaroo, B., Camasses, A., Derelle, E., Ferraz, C., Inze, D., Van de Peer, Y., and Moreau, H. (2005) Genome-wide analysis of core cell cycle genes in the unicellular green alga Ostreococcus tauri. *Mol Biol Evol* **22**: 589-597.

Scheffel, A., Gruska, M., Faivre, D., Linaroudis, A., Plitzko, J.M., and Schuler, D. (2006) An acidic protein aligns magnetosomes along a filamentous structure in magnetotactic bacteria. *Nature* **440**: 110-114.

Shibata, Y., Voeltz, G.K., and Rapoport, T.A. (2006) Rough sheets and smooth tubules. *Cell* **126**: 435-439.

Shimoni, E., Rav-Hon, O., Ohad, I., Brumfeld, V., and Reich, Z. (2005) Three-dimensional organization of higher-plant chloroplast thylakoid membranes revealed by electron tomography. *Plant Cell* **17**: 2580-2586.

Spahn, C.M., Beckmann, R., Eswar, N., Penczek, P.A., Sali, A., Blobel, G., and Frank, J. (2001) Structure of the 80S ribosome from Saccharomyces cerevisiae--tRNA-ribosome and subunit-subunit interactions. *Cell* **107**: 373-386.

Staehelin, L.A. (1997) The plant ER: a dynamic organelle composed of a large number of discrete functional domains. *Plant J* **11**: 1151-1165.

Stoffler, D., Feja, B., Fahrenkrog, B., Walz, J., Typke, D., and Aebi, U. (2003) Cryo-electron tomography provides novel insights into nuclear pore architecture: implications for nucleocytoplasmic transport. *J Mol Biol* **328**: 119-130.

Stoppin, V., Vantard, M., Schmit, A.C., and Lambert, A.M. (1994) Isolated plant nuclei nucleate microtubule assembly: the nuclear surface in higher plants has centrosome-like activity. *Plant Cell* **6**: 1099-1106.

Storrie, B., and Nilsson, T. (2002) The Golgi apparatus: balancing new with old. *Traffic* **3**: 521-529.

Subramaniam, S., and Milne, J.L. (2004) Three-dimensional electron microscopy at molecular resolution. *Annu Rev Biophys Biomol Struct* **33**: 141-155.

Suloway, C., Pulokas, J., Fellmann, D., Cheng, A., Guerra, F., Quispe, J., Stagg, S., Potter, C.S., and Carragher, B. (2005) Automated molecular microscopy: the new Leginon system. *J Struct Biol* **151**: 41-60.

van de Meene, A.M., Hohmann-Marriott, M.F., Vermaas, W.F., and Roberson, R.W. (2006) The three-dimensional structure of the cyanobacterium Synechocystis sp. PCC 6803. *Arch Microbiol* **184**: 259-270.

Voeltz, G.K., Prinz, W.A., Shibata, Y., Rist, J.M., and Rapoport, T.A. (2006) A class of membrane proteins shaping the tubular endoplasmic reticulum. *Cell* **124**: 573-586.

Vothknecht, U.C., and Westhoff, P. (2001) Biogenesis and origin of thylakoid membranes. *Biochim Biophys Acta* **1541**: 91-101.

Warner, J.R. (1999) The economics of ribosome biosynthesis in yeast. *Trends Biochem Sci* **24**: 437-440.

Wright, E.R., Iancu, C.V., Tivol, W.F., and Jensen, G.J. (2006) Observations on the behavior of vitreous ice at approximately 82 and approximately 12 K. *J Struct Biol* **153**: 241-252.

Yang, Q., Rout, M.P., and Akey, C.W. (1998) Three-dimensional architecture of the isolated yeast nuclear pore complex: functional and evolutionary implications. *Mol Cell* **1**: 223-234.

Yoon, H.S., Hackett, J.D., Ciniglia, C., Pinto, G., and Bhattacharya, D. (2004) A molecular timeline for the origin of photosynthetic eukaryotes. *Mol Biol Evol* **21**: 809-818.

Zadrag, R., Kwolek-Mirek, M., Bartosz, G., and Bilinski, T. (2006) Relationship between the replicative age and cell volume in Saccharomyces cerevisiae. *Acta Biochim Pol* **53**: 747-751.

Zheng, Q.S., Braunfeld, M.B., Sedat, J.W., and Agard, D.A. (2004) An improved strategy for automated electron microscopic tomography. *J Struct Biol* **147**: 91-101.

Figures

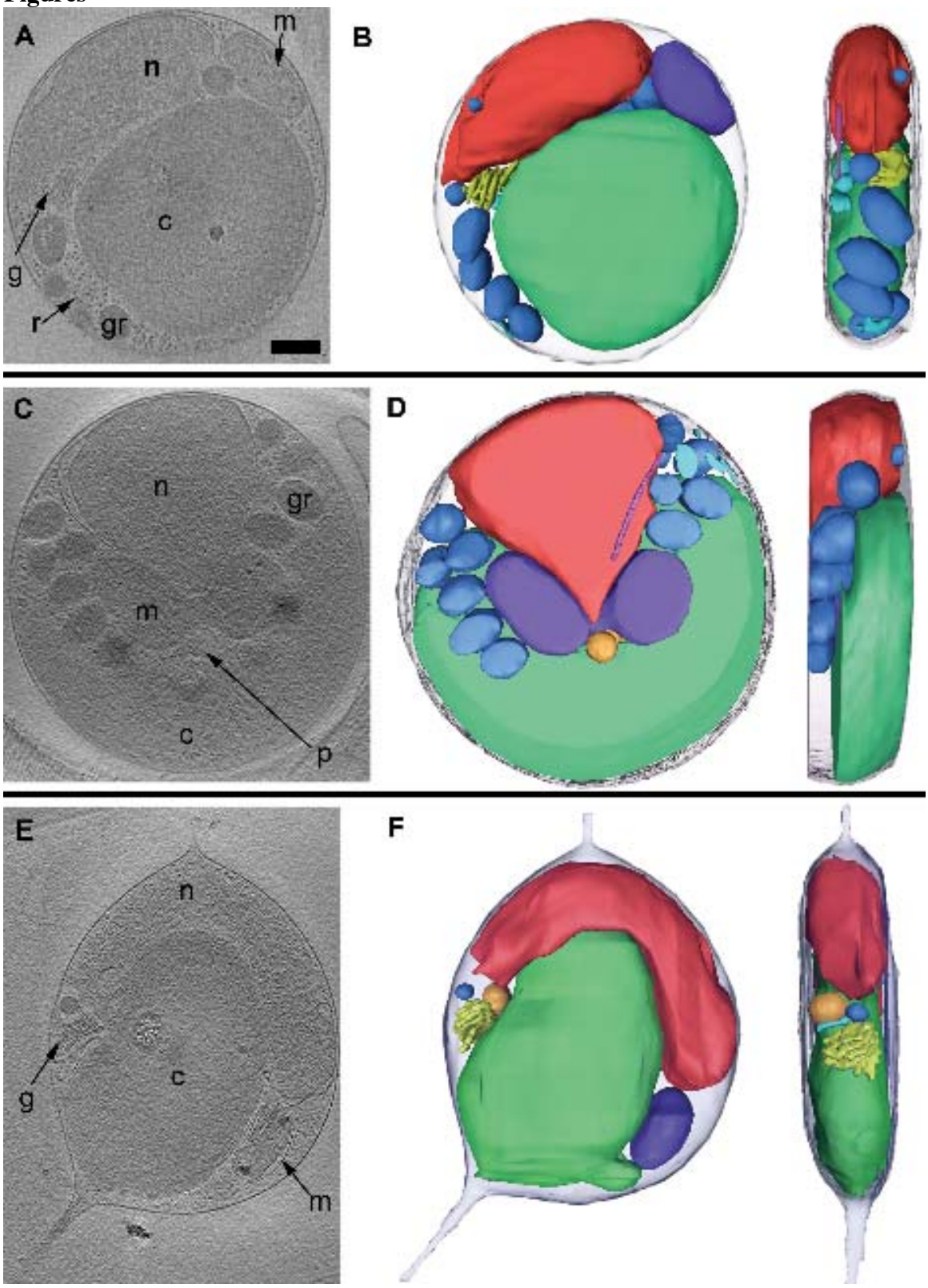

Figure III-1. Cross-sections and 3-D segmentations of *O. tauri* cells. Each row shows a single slice (A 21.6-nm; B 36-nm; C 9.6-nm) through the middle (left) and a manually segmented model (two perpendicular views, right) of one particular cell: (A, B) a non-dividing cell harvested at the dark-to-light transition; (C, D) a dividing cell harvested at the light-to-dark transition; (E, F) an unusual cell with a different internal organization and two membrane-bound cell extensions. Here and below the letters and colors identify nuclei (n, red), chloroplasts (c, green), mitochondria (m, dark purple), Golgi bodies (g, yellow), peroxisomes (p, orange), granules (gr, dark blue), inner membranes including ER (er, light blue), microtubules (light purple), and ribosome-like particles (r). Because the dividing cell shown in panels C and D was especially thick, only its middle region was segmentable. scale bar 250 nm

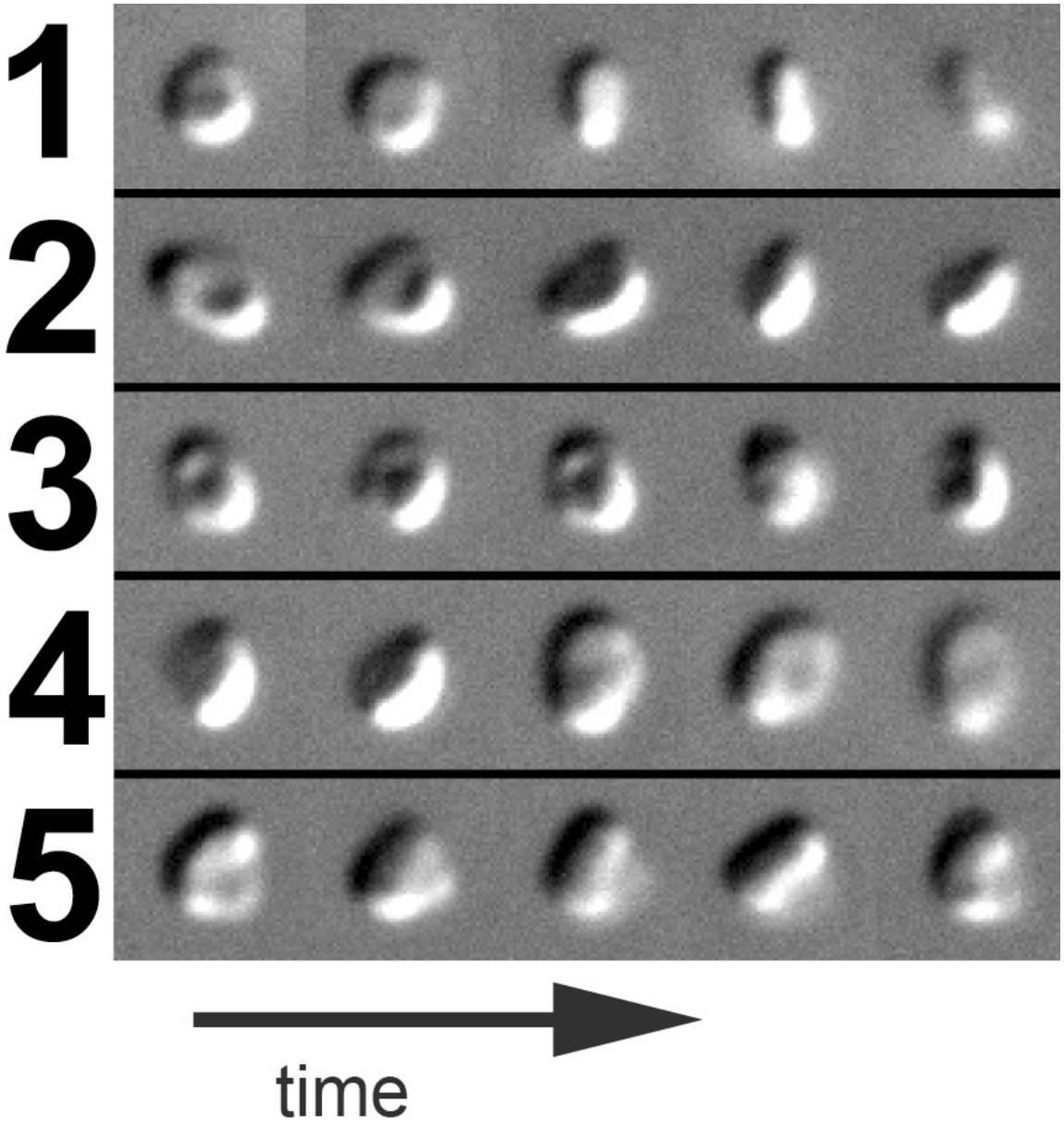

Figure III-2. Light microscope images of free-floating *O. tauri.* Sequential DIC images of five representative cells (1-5) tumbling freely in sea water culture medium after six hours growth in light are shown from left to right, demonstrating their disk-like shape.

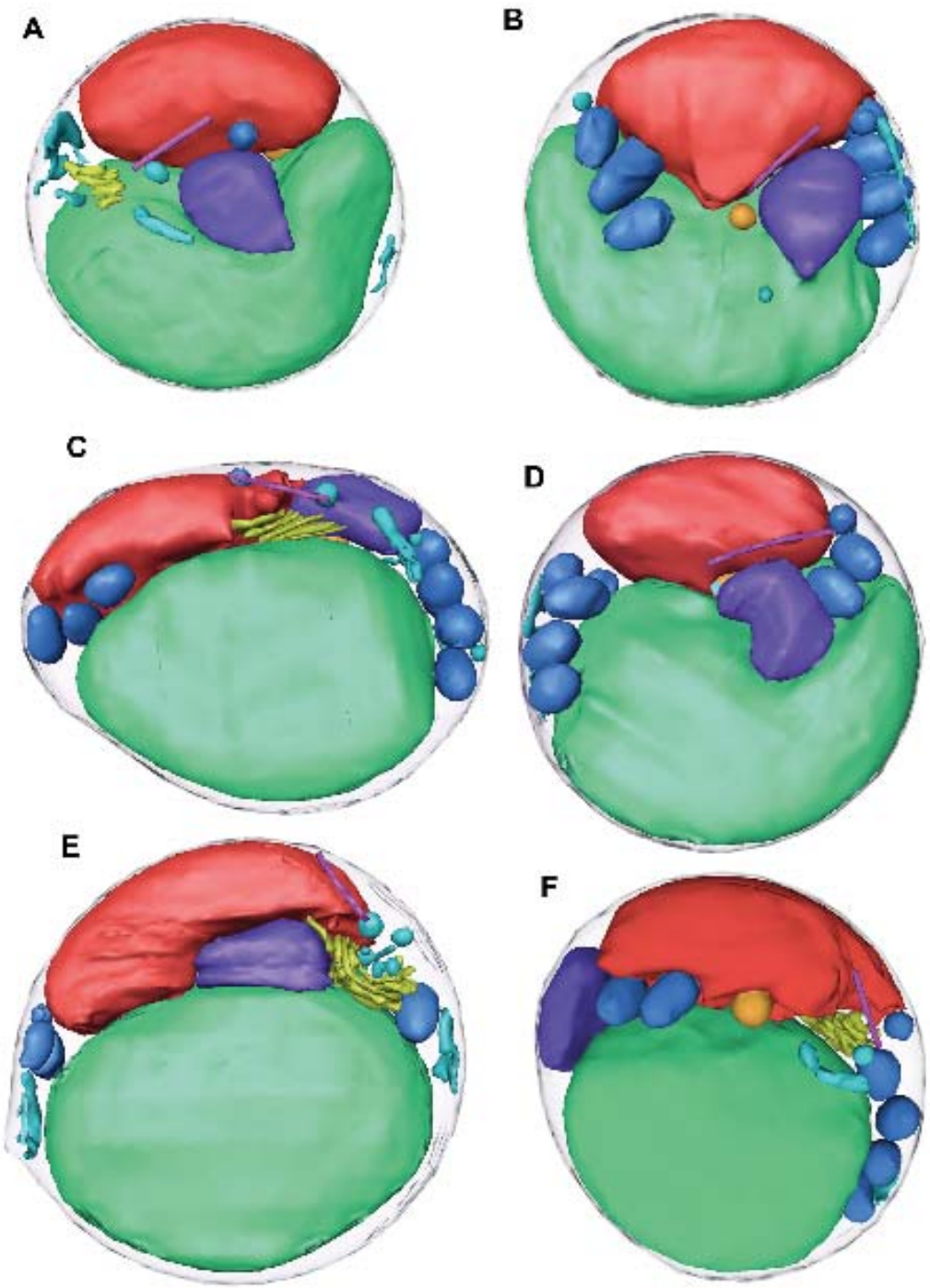

Figure III-3. 3-D segmentations of six cells imaged at the dark-to-light transition (mid G_1). The cell in panel F is the same as in Figure III-1A-B and 12. For scale, the diameter of the cell in panel D is approximately 1750 nm in diameter.

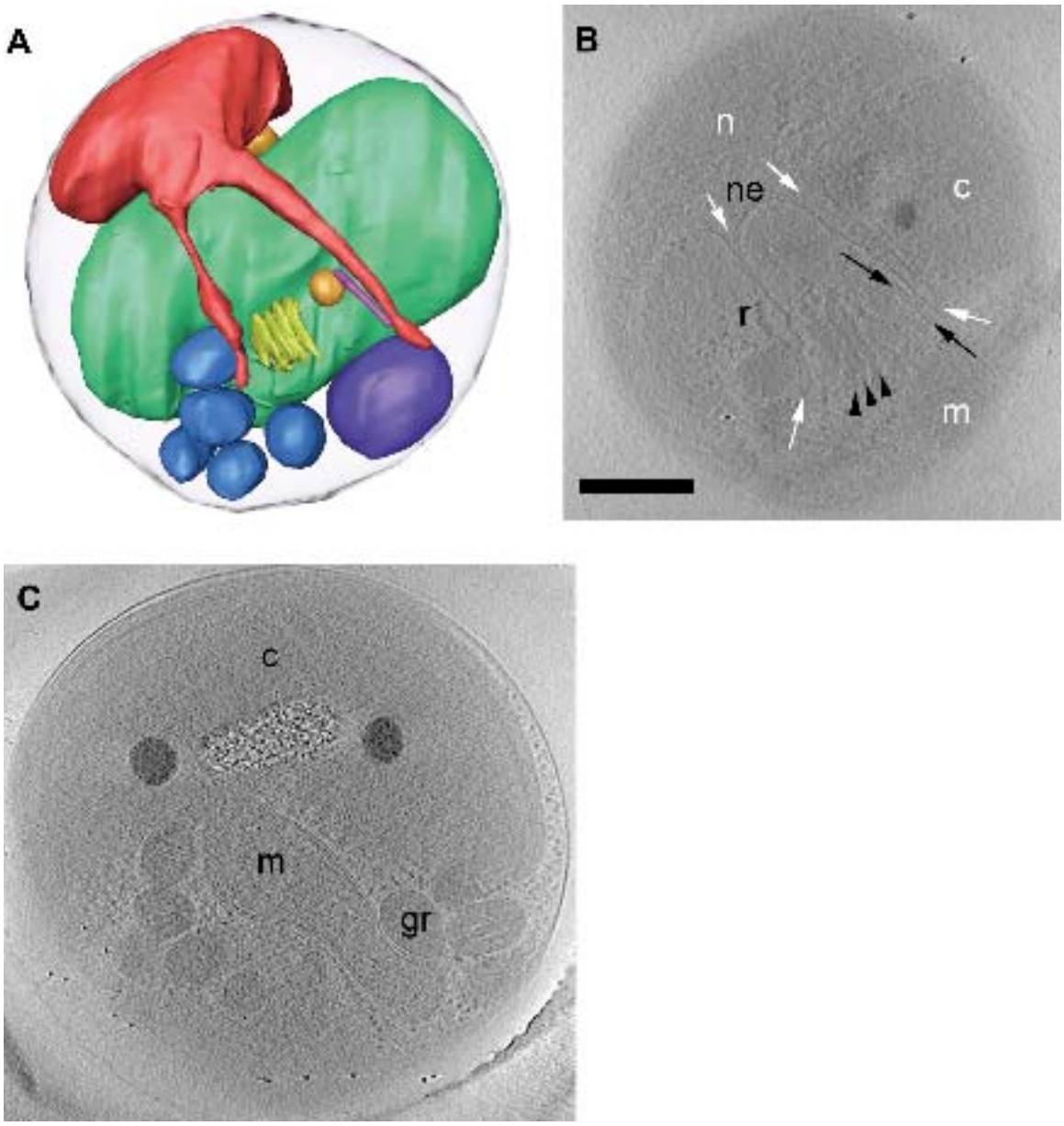

Figure III-4. Cells with dividing organelles. (A) Segmentation showing a portion of a NE streaming over the top of a chloroplast. Here the chloroplast is separated from the plasma membrane by the mitochondrion and several granules. (B) 36 nm thick slice near the top of the reconstruction of the same cell. The NE (white arrows) stretches towards the Golgi body (black arrowheads) and microtubule (black arrows). (C) 24 nm slice through a different cell, showing an elongated mitochondrion near the center of the cell and duplicating chloroplast granules. scale bar = 150 nm

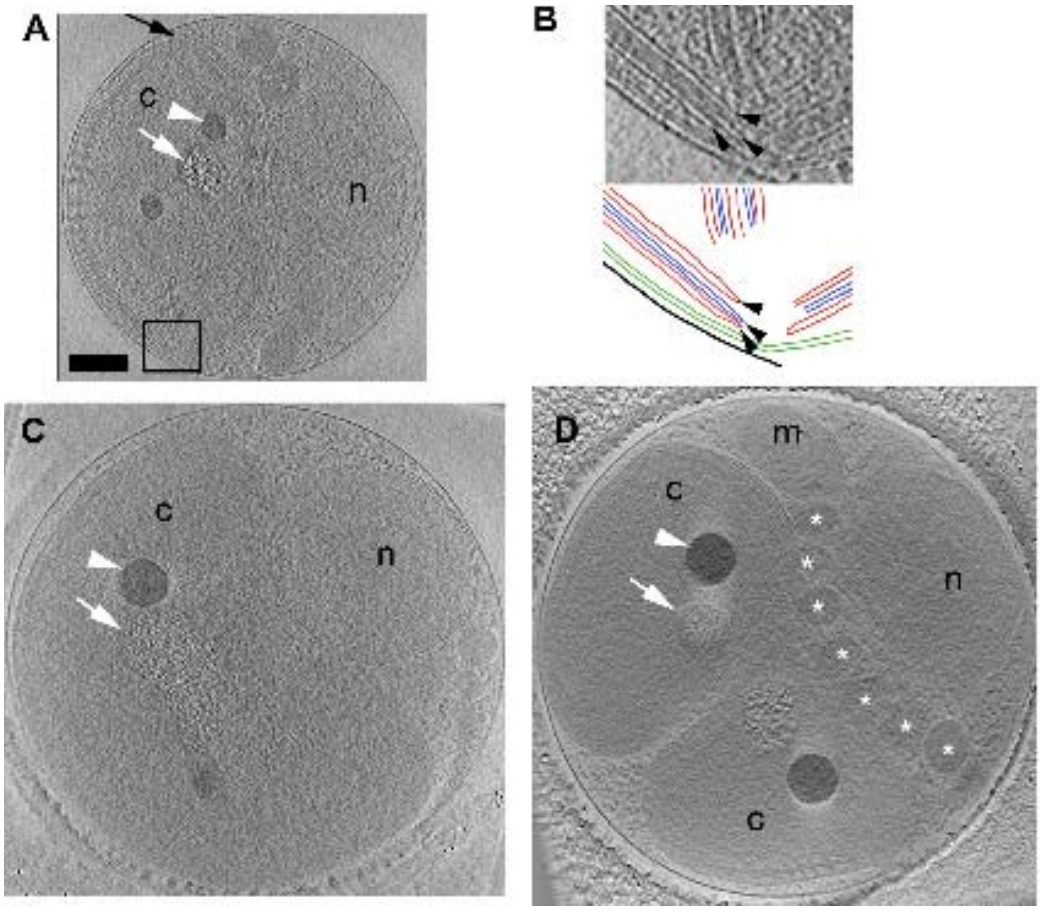

Figure III-5. Chloroplast. (A) 7.2 nm thick slice through a non-dividing cell. The starch granule (white arrow) has suffered damage from the electron beam. Beside it are two dark granules (white arrowhead). (B) Above: Enlarged view of the boxed area in panel A. The three thylakoid membranes (black arrowhead) can be seen forming a stack. Below: Schematic of above. Cell membrane (black), chloroplast membranes (green), outer thylakoid membrane (red), inner thylakoid membranes (blue). (C) 24 nm slice through an early predivisional cell, where the chloroplast is kidney-shaped rather than oval and the starch granule is elongated. (D) 36 nm thick slice through a late predivisional cell, where the chloroplast is deeply constricted and one dark and one starch granule is found in each side. Here the cytoplasmic granules (*) are arranged in a V-shape pointing to the division plane. scale bar 250 nm

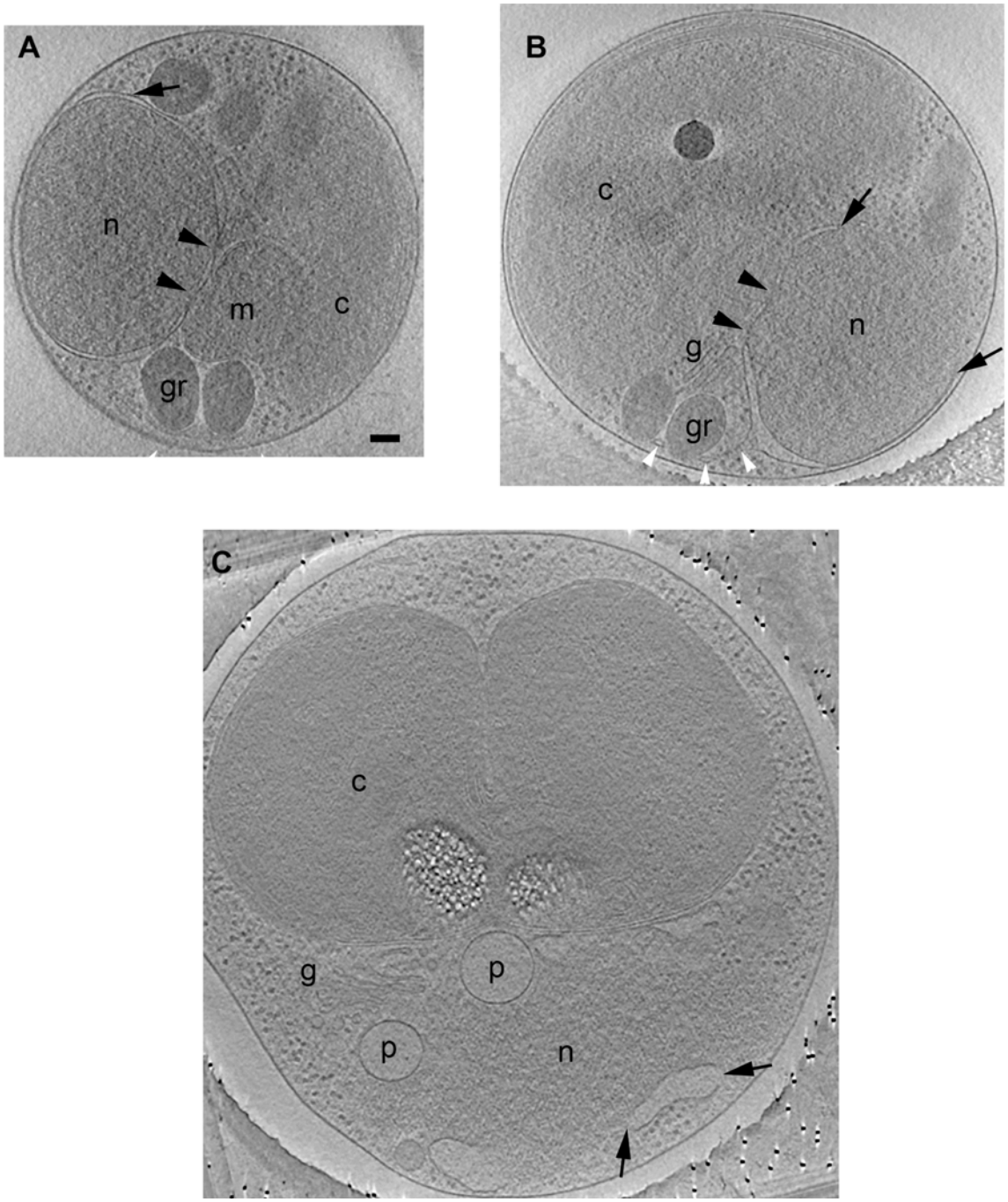
A
n
m
c
gr
B
c
g
n
gr
C
c
g
p
p
n

Figure III-6. Nuclear envelope. (A) 41 nm thick slice through a cell harvested at the light-to-dark transition with a completely closed NE (black arrow). The cell's small size and non-dividing organelles suggest the cell could have recently divided. Two NPCs (black arrowheads) are present. (B) 31 nm thick slice through a cell harvested at the dark-to-light transition. The NE only covers about three-fourths of the nucleus in this section (black arrows mark the tips). Again two NPCs (black arrowheads) are present, and at the bottom of the nucleus the ER branches off the NE (white arrowheads). (C) 19.2 nm thick slice through a large, late predivisional cell harvested at the light-to-dark transition exhibiting an almost completely open nucleus with only small patches of NE (black arrows). scale bar 100 nm

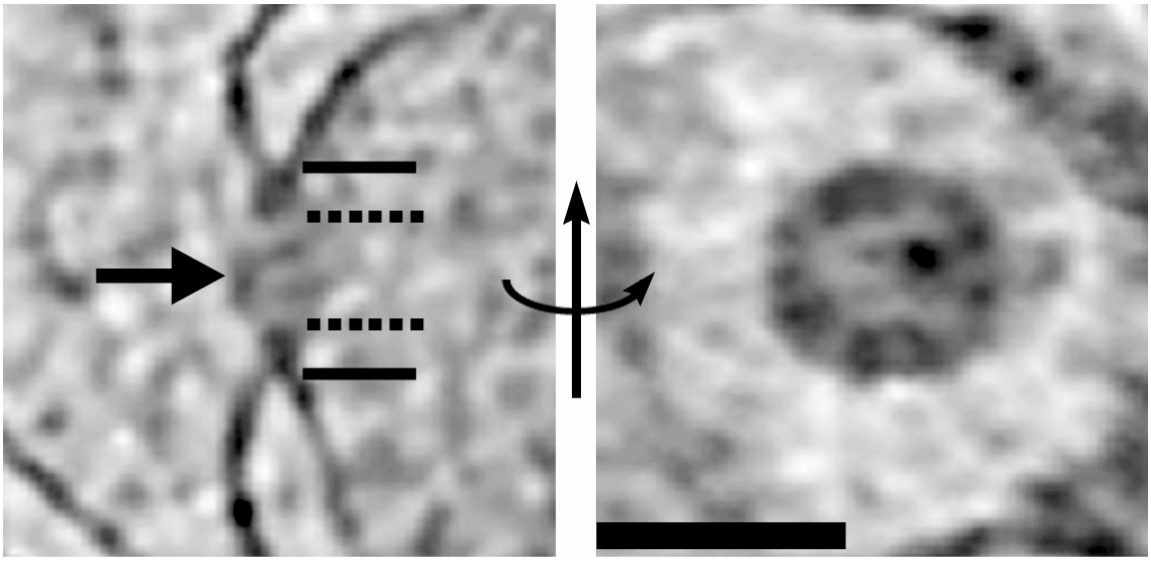

Figure III-7. Nuclear pore complex. 3.6 nm thick slices through the best-resolved NPC from the "side" (perpendicular to the NE, left) and "top" (in plane of NE, right). The approximate center, inner, and outer diameters are marked by the arrow, dashed, and solid lines, respectively. The region around the NPC in the right panel is low density (whiter) because it is inside the NE lumen; the dark crescent near the edge of the panel shows where the plane of the slice cuts through the NE. scale bar = 100 nm

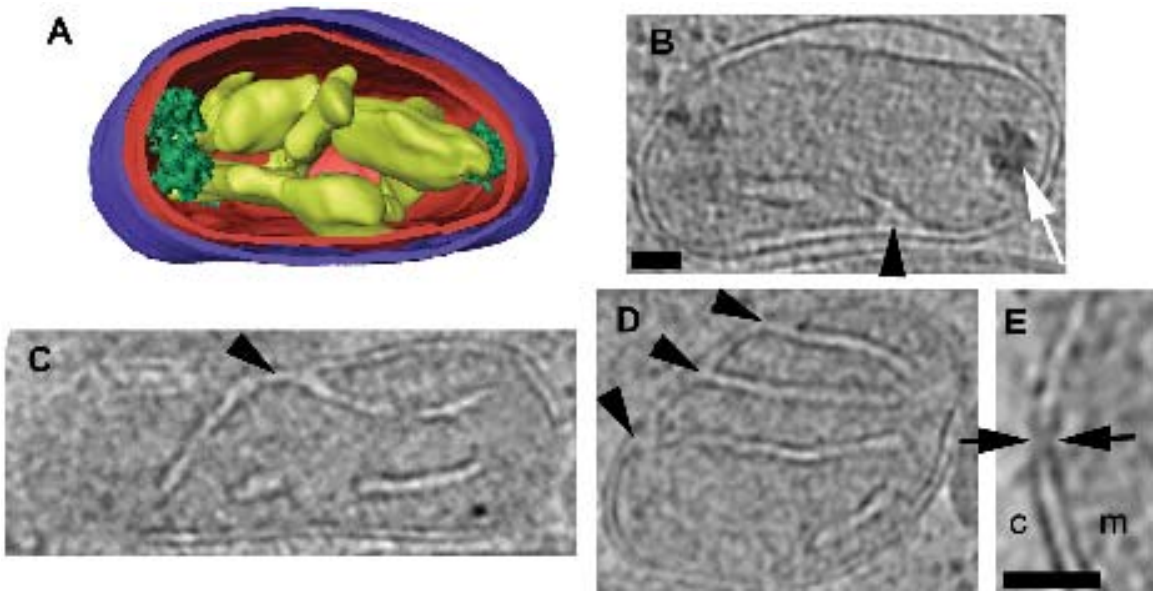

Figure III-8. Mitochondrion. (A) 3-D segmentation of the mitochondrion from the cell shown in Figure III-1E-F. Here, the membranes are colored purple (outer membrane), red (inner membrane), and yellow (cristae). Dense granules within the mitochondrial matrix are shown in green. (B-D) 15, 55, and 29 nm thick slices though three different mitochondria, showing crista junctions (arrowheads) and a dense granule (white arrow). Panel B is a slice through the cell shown in panel A. Scale bar 50 nm (for panels B-D). (E) 4.8 nm thick slice through a junction or channel (black arrows) connecting the outer and inner membranes. Here c-cytoplasm, m–mitochondrion. scale bar 50 nm

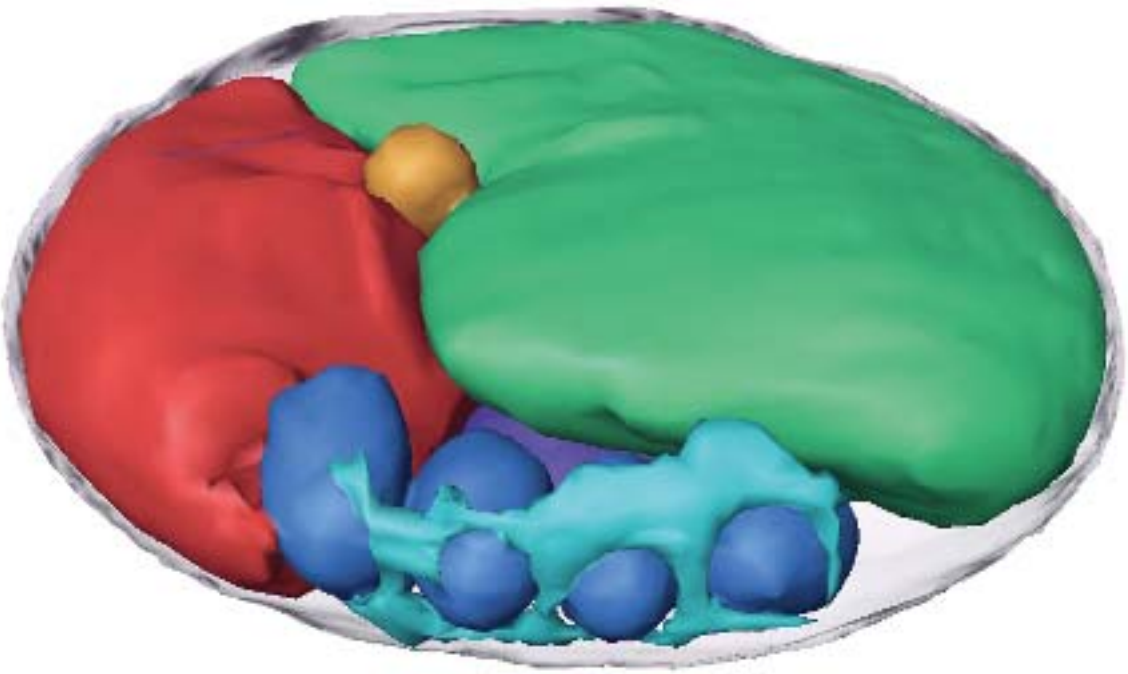

Figure III-9. Endoplasmic reticulum. 3-D segmentation of a cell harvested at the dark to light transition. ER (light blue) forms a sheet near the edge of the cell, perforated by four granules (dark blue).

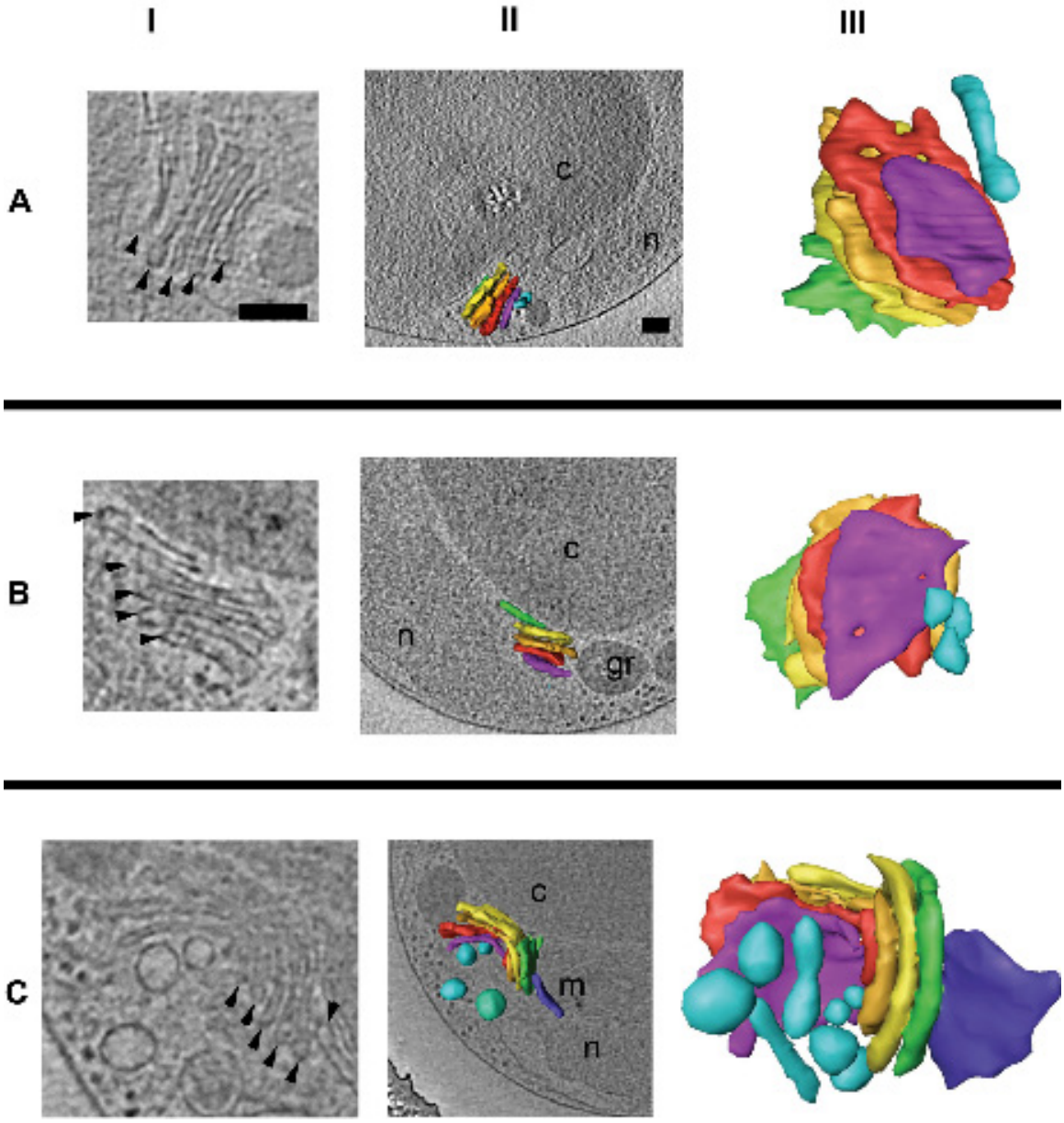
I
II
III
A
c
n
B
c
n
gr
C
c
m
n

Figure III-10. Golgi body. The Golgi bodies from three different cells are shown (rows A-C). In column I, slices through the reconstructions are shown, with cisternae marked by arrowheads. In column II, 3-D segmentations of the Golgi bodies are shown *in situ* within their cellular contexts. Column III shows the isolated 3-D segmentations from a view perpendicular to the one in column II. The five "core" cisternae common to all Golgi bodies seen here are colored purple, red, gold, yellow, and green (cis to trans). Surrounding vesicles are colored either light or dark blue. Some vesicles in column III do not appear in column II because they are "below" the cellular slice shown. The blue-green vesicle in IIC was removed from IIIC to create an unobstructed view of the Golgi body. scale bars 100 nm

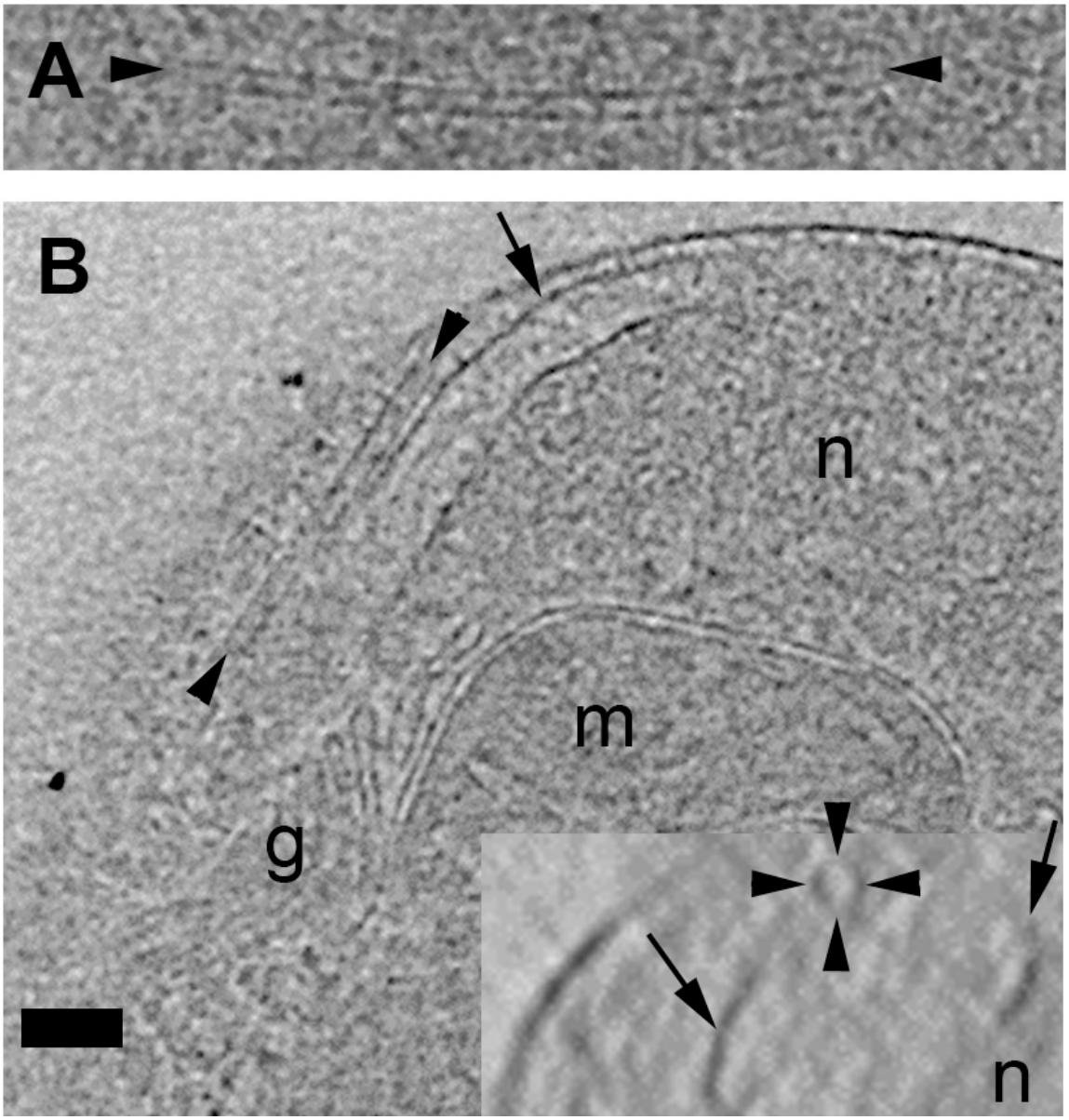

Figure III-11. Microtubule. (A) 9.6 nm slice through one particular microtubule (arrowheads) along most of its length, showing its uniform diameter and hollow nature. (B) 16.8 nm slice through a microtubule in its cellular context, showing its open, blunt ends (arrowheads) terminating between the NE (arrows) and plasma membrane. The insert shows a 2-fold enlarged, 38.4 nm thick slice through the microtubule perpendicular to its long axis, emphasizing its tubular shape (arrowheads). scale bar 100 nm

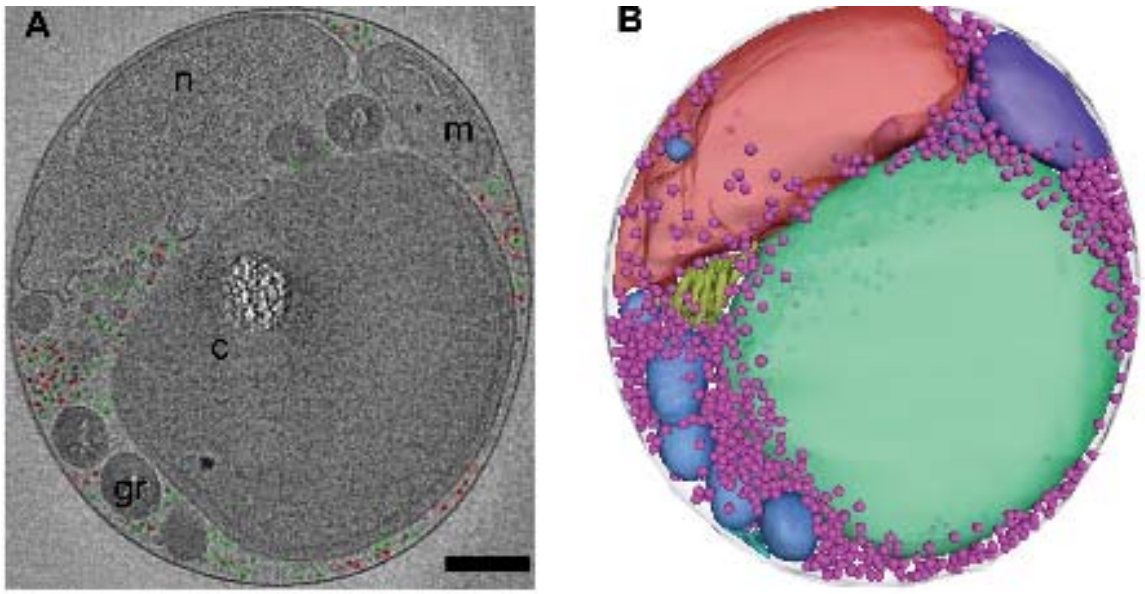

Figure III-12. Ribosome-like complexes. (A) 24 nm thick slice through a cell with the 500 (red) or 2000 (green) most ribosome-resembling objects in the cytoplasm circled, showing that these are reasonable under- and over-estimates of the total number. (B) 3-D positions of the 1250 most ribosome-resembling objects in the cytoplasm (light purple spheres), showing their close and even distribution. scale bar 250 nm

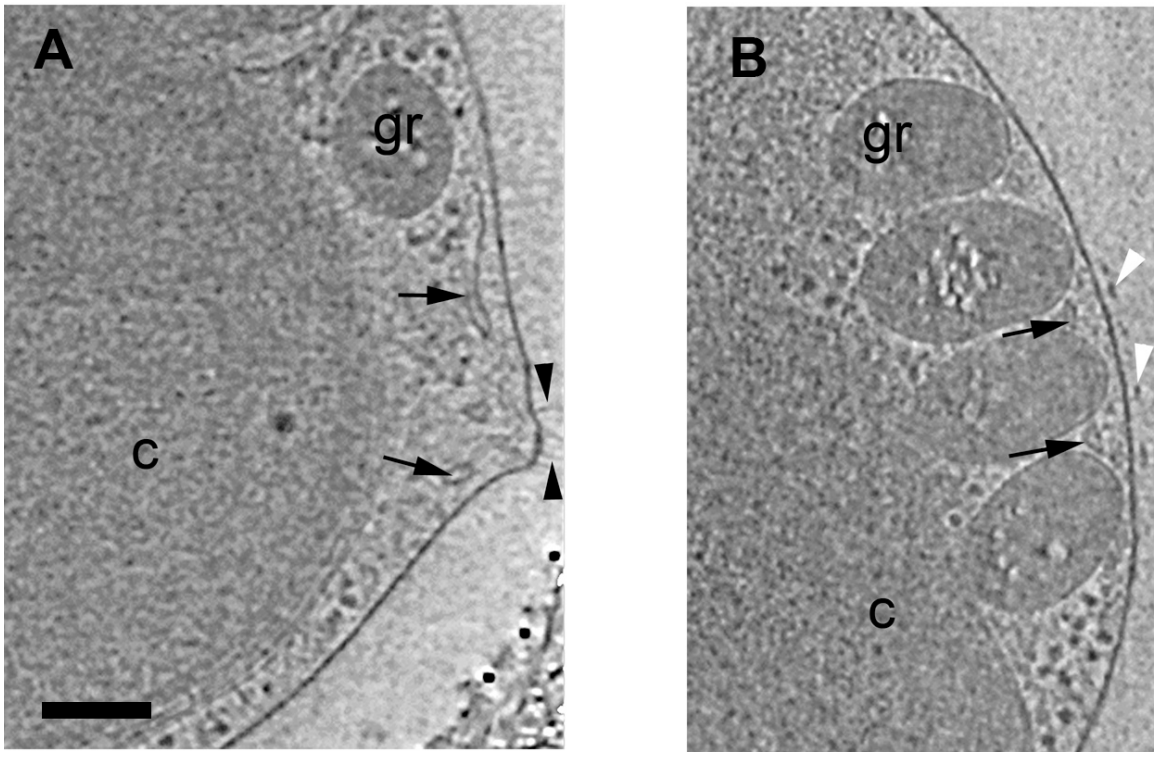

Figure III-13. External protein complexes. (A) 12 nm thick slice showing multiple filaments (black arrowheads) emerging from a cellular protuberance. Black arrows point to ER. (B) 12 nm thick slice showing protein complexes (white arrowheads) on the outer surface of the plasma membrane. scale bar 100 nm.

Supplementary Figures.

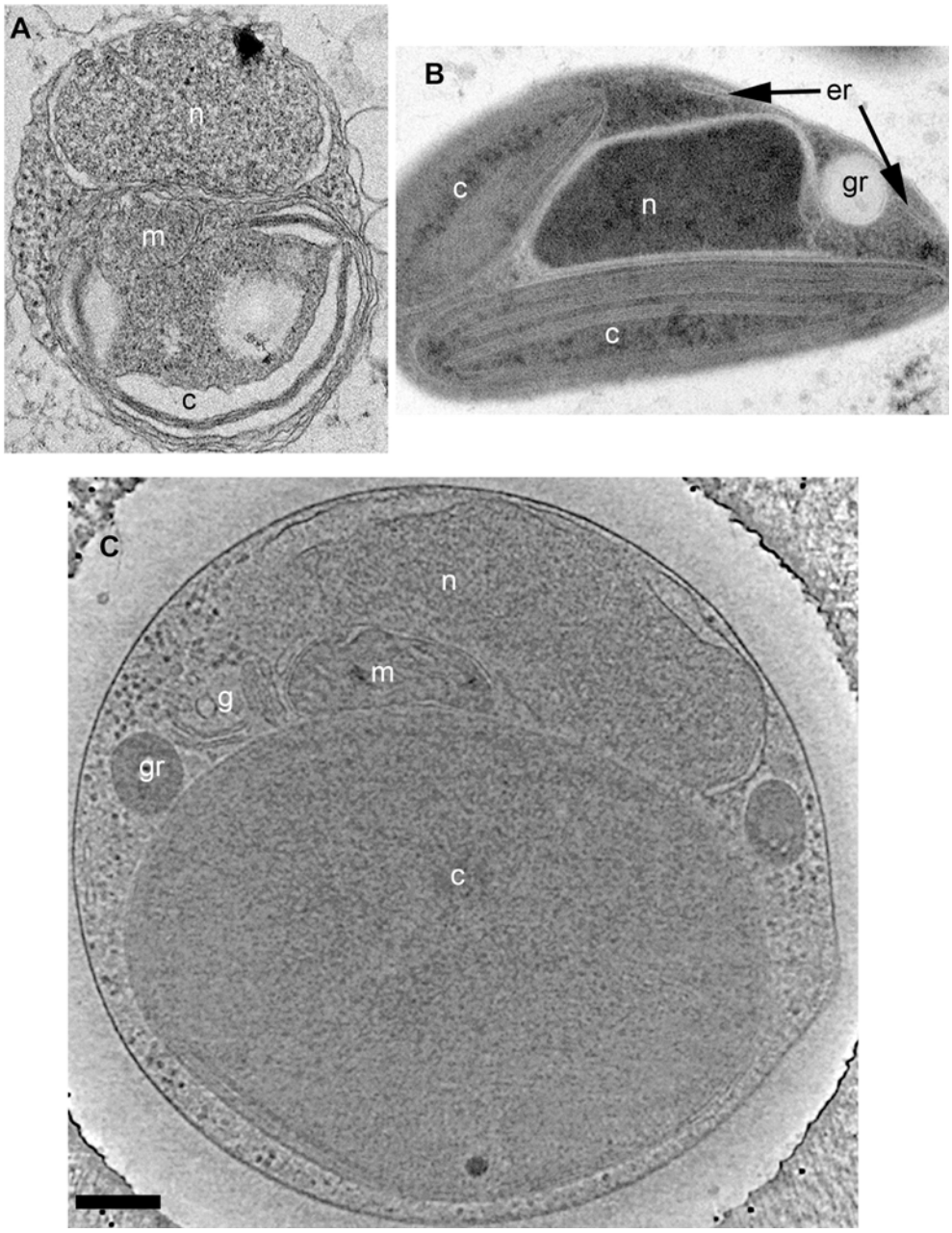

Figure III-S1. Preservation of *O. tauri*. (A) Projection image through a conventionally fixed, embedded, thin-sectioned cell. (B) Projection image through a high-pressure frozen, low-temperature embedded, thin-sectioned cell. (C) 28.8 nm thick slice through the 3-D electron cryotomographic reconstruction of an intact, frozen-hydrated cell. scale bar = 200 nm

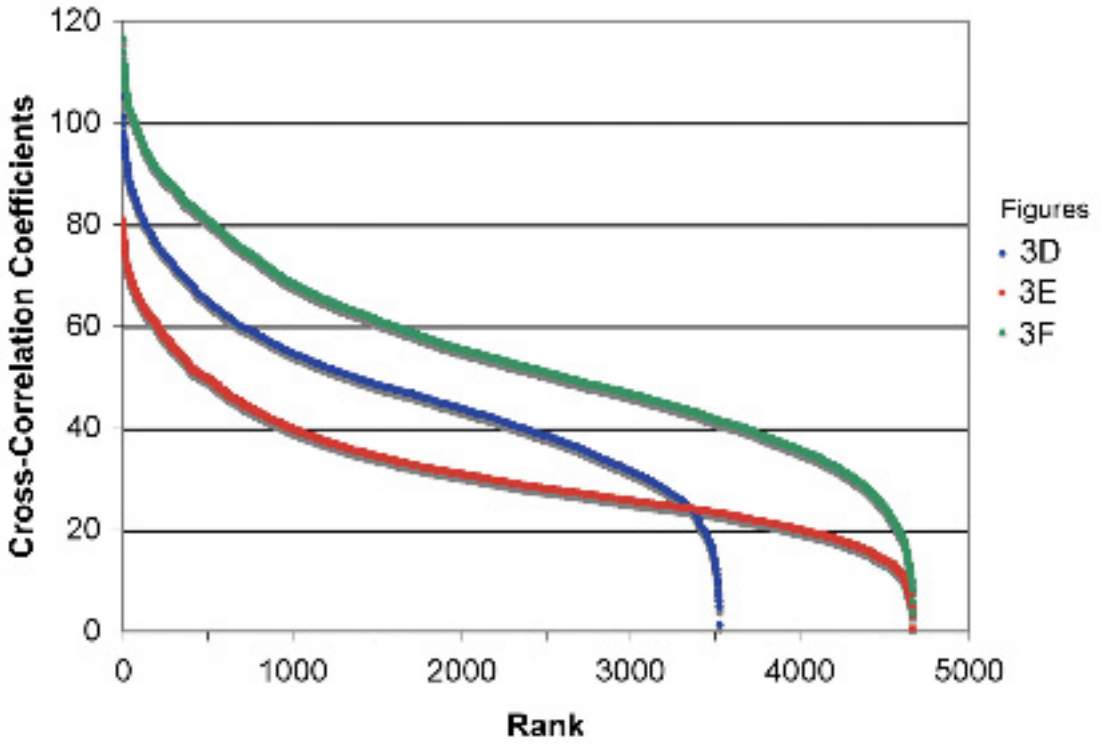

Figure III-S2. Ribosomal cross-correlation coefficients. Three cells (those shown in panels D-F of Figure 3) were searched for ribosome-like particles, and the resulting cross-correlation coefficients (arbitrary units) are plotted from best to worst from left to right. There were fewer total positions ranked in cell Figure III-3D because its cytoplasm was smaller.

Chapter 4: Conclusion

Mycoplasma pneumoniae and *Ostreococcus tauri* are model minimal cells, genomically and spatially, respectively. Whole cell electron cryotomography was used to identify and characterize the large protein motor inside of *M. pneumoniae*'s attachment organelle (Chapter 2) and show the organization of a eukaryotic cell throughout the cell cycle (Chapter 3). This work contributed to the development of techniques to prepare whole cells in a frozen hydrated state (Appendix).

The discovery of *M. pneumoniae*'s motor will drive future studies to identify the proteins that form the motor, and ultimately lead to an understanding of how the motor functions. This could lead to targeted drug therapy for *M. pneumoniae* infections. The identification of a new macromolecular motor will also add to a new tool for nanotechnology. Besides the flagellar motor, other large macromolecular motors have not been well characterized. A significant advantage of *M. pneumoniae*'s motor is that it has already been shown to function independent of the cell body (Hasselbring and Krause, 2007).

O. tauri showed many fundamental surprises that will lead to future work to completely understand their ramifications. 1) *O. tauri* has a simplified mechanism for mitosis. Chromosome segregation is unlikely to rely on a mitotic spindle and chromosome condensation. 2) The nuclear envelope has large gaps in it throughout much of the cell cycle. Despite this, the cell maintains a distinct nucleo-plasma and retains nuclear pore complexes. 3) The chloroplast creates its own internal division plane and segregates its granules and genome. 4) Without multiple copies of the mitochondria, one must expect controlled segregation of the mitochondrion genome. 5) *O. tauri*'s extremely simplified organelle structure, with one copy of each major organelle, showed that the division and segregation of

its organelles were never left to chance. One may speculate that the tight regulation of organelles is probably not unique to *O. tauri*. *O. tauri*'s simple structure makes obvious a phenomenon probably present in most eukaryotes. Together, these three papers have demonstrated how electron cryotomography will continue to dramatically alter the way we think about how cells are organized.

Reference

Hasselbring, B.M., and Krause, D.C. (2007) Cytoskeletal protein P41 is required to anchor the terminal organelle of the wall-less prokaryote Mycoplasma pneumoniae. *Mol Microbiol* **63**: 44-53.

Electron cryotomography sample preparation using the Vitrobot.

Cristina V. Iancu, William F. Tivol, Jordan B. Schooler, D. Prabha Dias, Gregory P. Henderson, Gavin E. Murphy, Elizabeth R. Wright, Zhuo Li, Zhiheng Yu, Ariane Briegel, Lu Gan, Yongning He, and Grant J. Jensen*

Division of Biology, California Institute of Technology, Pasadena, CA

*Corresponding Author. Mail address: Caltech Division of Biology, 1200 E. California Blvd., Pasadena, CA 91125. Phone: (626) 395-8827. Fax: (626) 395-5730. E-mail: jensen@caltech.edu.

Published in *Nature Protocols* 2007; 1: 2813-2819

doi:10.1038/nprot.2006.432

ABSTRACT

Electron cryotomography (ECT) is the highest resolution structural technique currently available that can be applied to unique objects such as flexible large protein complexes, irregular viruses, organelles, and small cells. Specimens are preserved in a near-native, "frozen-hydrated" state by vitrification. The thickness of the vitreous ice must be optimized for each specimen, and gold fiducials are typically added to facilitate image alignment. Here, we describe in detail our protocols for ECT sample preparation including (1) introduction of fiducial markers into the sample, and (2) sample vitrification. Because we almost exclusively use an automated, climate-controlled plunge freezing device (the FEI Vitrobot) to vitrify our samples, we discuss its operation and parameters in detail. A session in which 8 grids are prepared takes 1.5 to 2 hours.

INTRODUCTION

Electron cryotomography (ECT) is an increasingly important technique for determining the structure of unique objects such as flexible large protein complexes, irregular viruses, organelles, and small cells (Lucic et al., 2005; Nickell et al., 2006). Specimens preserved in a near-native, "frozen-hydrated" state are tilted incrementally around one or two (orthogonal) axes while being imaged in a transmission electron microscope (TEM). The resulting "tilt-series" of projections are aligned with respect to each other usually using fiducial markers (electron-dense reference objects such as colloidal gold) embedded with the sample in the ice. The aligned images are then computationally merged into a three-dimensional (3-D) reconstruction.

As in all types of microscopy, sample preparation is vital. Three factors are key: the sample itself must be maintained in as near a native state as possible, the vitreous ice must be thin and uniform, and the fiducial markers should be abundant and evenly distributed. To minimize artifacts and perturbations, samples can be plunge-frozen in complete growth media or physiologic buffers. Because the surrounding media or buffer produces background scattering that degrades the image, however, it is generally advantageous to thin the ice as much as possible, as long as the structure of the sample is not distorted. In extremely thin ice, even individual strands of duplex DNA have been seen in electron cryomicrographs (Adrian et al., 1990). Thicker ice seems to have improved mechanical stability, however, in other contexts (Li et al., 2002), so ice thickness must be optimized for every situation. The fiducial markers need to be abundant and distributed uniformly to ensure accurate image alignment.

ECT sample preparation typically comprises two major steps: (1) introduction of gold fiducial markers and (2) sample vitrification. In order to increase the chances of having uniformly distributed fiducials in any particular area, we apply colloidal gold to both the grids and the sample solutions before they are united. Aqueous solutions are vitrified by cooling them so quickly (~ 10^7 K/s) that individual water molecules do not have opportunity to move around and form an extended, hydrogen bond-mediated crystal lattice with long-range order. Rather, they become "trapped" in an amorphous state resembling liquid water (Angell, 2004). Using a strategy pioneered by Jacques Dubochet and his colleagues (Adrian et al., 1984; Dubochet and McDowall, 1981; Lepault et al., 1983), this can be accomplished in four steps: (1) applying the sample onto an electron microscopy grid; (2) blotting excess fluid to produce a thin film; (3) plunge-freezing the grid into liquid ethane or propane; and (4) transferring the grid to a storage box immersed in liquid nitrogen.

Today many labs have custom-made, "in-house" plunge-freezing devices where the sample is blotted manually (by hand with a filter paper) and the plunger is accelerated by gravity or air pressure. We are not aware of any that give robustly reproducible results, however, even for expert practitioners, because they depend on user dexterity, timing, and the local climate conditions. More recently, sophisticated commercial devices have become available that allow precise control of nearly all the parameters including the temperature and humidity of the blotting chamber; the frequency, duration, and pressure used for blotting; and the plunge velocity. In our lab we use the FEI Company's automatic plunge-freezer, which they named the "Vitrobot" (Frederik and Hubert, 2005). In addition to the aforementioned parameters, which are self-explanatory, a "blot offset" parameter controls the position of the grid between the blotting pads, which controls in part the pressure exerted by the filter paper

on the grid. "Drain time" is a surprisingly useful parameter that specifies an optional delay between blotting and plunging when the sample simply equilibrates in the blotting chamber ("drain time" is actually a misnomer, since no fluid is actually draining). In general, the blotting chamber is humidified to 100% to minimize potential imbalances in evaporation and condensation that might develop during the drain time, and the temperature is generally set to the preferred temperature of the sample (can be the incubation temperature of a cell culture, for instance).

Using the Vitrobot, we have successfully prepared a variety of samples for ECT including large protein complexes, viruses, organelles, and narrow whole cells (Benjamin et al., 2005; Briegel et al., 2006; Henderson and Jensen, 2006; Iancu et al., 2005; Iancu et al., 2006; Komeili et al., 2006; Murphy and Jensen, 2005; Murphy et al., 2006; Wright et al., 2006). The protocol and discussion presented here is the result of our laboratory members' collective experience with several different Vitrobots and in-house plunge freezing devices and will describe details of both the introduction of fiducial markers and the specific Vitrobot conditions used for different samples. (Additional information on the use and applications of the Vitrobot, including a video demonstration of its operation, can be found on the company website at www.vitrobot.com.)

MATERIALS

REAGENTS

- sample
- 10 nm (or 5 nm) colloidal gold (SPI Supplies, West Chester, PA, USA, www.2spi.com, or Sigma, St Louis, MO, USA, www.sigma.com)
- liquid nitrogen
- ethane
- bovine serum albumin (BSA)

CAUTION: Liquid nitrogen and ethane are cryogens and should be handled with care and appropriate personal protective equipment (goggles, gloves, lab coat). Additionally, ethane gas is flammable and along with nitrogen poses an asphyxiation hazard and should only be used in a well-ventilated, spark-free environment.

CRITICAL: Small gold fiducials can be more precisely localized and obscure fewer specimen details, but they can be difficult to see at high tilt angles in thick samples. For objects larger than ~ 30 nm, use 10 nm colloidal gold, but for smaller specimens (for example, protein complexes under 1 MDa), 5 nm colloidal gold will likely be better. Some batches of colloidal gold are prone to clumping. In some cases, coating these particles with BSA helps prevent their aggregation (see the reagent setup section). In our experience this property neither improves nor degrades with shelf life, so if a good batch is found it can be

used successfully for years. Store colloidal gold solution at 4 °C in 1 ml aliquots, in 1.5 ml centrifuge tubes in order to minimize repeated contact with air and, implicitly, variations in temperature and possible contamination that may cause further aggregation.

EQUIPMENT

- lacey carbon film on 200 mesh copper grids (Ted Pella, Redding, CA, USA, www.tedpella.com) or Quantifoil holey carbon films (various sizes) on 200 mesh copper/rhodium grids (Quantifoil Micro Tools, Jena, Germany, www.quantifoil.com)
- plasma cleaner (Harrick, Model PDC-32G)
- filter paper (pre-punched from FEI Co or Whatman #1)
- grid boxes (usually custom-made)
- anticapillary tweezers (SPI Supplies, West Chester, PA, USA, www.2spi.com)
- vortexer
- FEI Vitrobot (FEI Company, Hillsboro, OR, USA, www.vitrobot.com)
- forceps or long tweezers
- cryo-transfer dewars

CAUTION Any metallic tool such as a forceps or tweezer in contact with liquid nitrogen will be extremely cold and should be handled with care and appropriate personal protective equipment (gloves).

EQUIPMENT SETUP

Grids CRITICAL: Before starting, carefully choose which type of grid to use. In our experience, the carbon film of lacey grids is more sensitive to dose than that of Quantifoil grids. Therefore, if the intended total dose per tomogram exceeds ~ 60 electrons/Å^2, Quantifoil grids are a better choice. Furthermore, the selection of the type of Quantifoil film (hole size) depends on the type of sample and the targeted magnification (pixel size of the image). During data collection, successive tilts are correlated with each other to maintain tracking, and it is helpful to have contrast-rich features in the field of view. For small objects (10–100 nm) such as protein complexes or viruses that are imaged at 4–5 Å per pixel and have little contrast, Quantifoil holey film grids such as R 0.6/1 or R1.2/1.3 are most suitable because the holes are smaller and their edges guide the tracking. On the other hand, for cells that are around 2 μm in length, R 2/2 or R 2/1 grids are more appropriate because the entire cell can be housed within a hole. Although we have not tried this specifically, for much longer cells, we would predict that R 3.5/1 or S 7/2 grids would be even better.

In our experience, grids that are nominally identical but were manufactured on different days can behave quite differently with regards to dose (they may bubble earlier) or wetting (the ice distribution may be uneven). We think that grids bubble sooner if they are dirty and distribute ice more poorly as they age. Because of this we procure freshly manufactured grids. Our main grids supplier, Quantifoil, labels the batches of grids with the date on which the carbon film was applied. One way to clean the grids is to simply rinse them in methanol before glow-discharging. An easy way is to float them on a drop of methanol on parafilm for

30 seconds, then pick them up with anti-capillary tweezers, remove most of the methanol by touching the grid edge to filter paper, and then let them finish drying by evaporation.

Because the cooled freezing apparatus becomes increasingly contaminated with ice during the procedure, we recommend that only two boxes of grids (8 grids total) should be frozen per session.

Vibrobot Turn on the tank of compressed air ensuring that the proper air pressure (at least 6 bar) is applied to the Vitrobot. Fill the humidifier with distilled water using the special 60 ml syringe. Mount the filter paper on the blotting pads, securing them with the clip rings (it is better to do this while the Vitrobot is off because the plunger is not in the way). Turn on the Vitrobot and set the desired parameters in the Console and Options screens: temperature, humidity (100%), type of application (manual or automatic), the blotting time, blotting offset, drain time, wait time, etc.

REAGENT SETUP

Sample Depending on the molecular weight of a purified specimen, the concentration of the sample should be somewhere between 0.3–8 mg/ml. In our hands, saturated bacterial cultures produce well-populated grids when the cells are concentrated about 20 times by very gentle centrifugation. Care must be taken, however, because centrifugation or turbulent

ejection from a small-diameter syringe can shear off external structures such as pili or flagella and can distort cell shape. Likewise, extensive centrifugation may distort the shapes of viruses or cause other structural damage. Whenever possible, use buffers low in salt and without glycerol or sucrose to increase contrast.

Bovine serum albumin (BSA)-treated colloidal gold Coating the gold fiducials with BSA can help prevent clumping and promote even distribution on the grid. To do this, make a stock solution of 5% (w/v) BSA solution in distilled water. Using a tabletop centrifuge, pellet a volume of 10 nm colloidal gold for ~ 10 minutes at 18,000X gravity (25 minutes for 5 nm colloidal gold). Carefully remove the supernatant with a micropipette. Resusupend the pellet of colloidal gold in the same volume of 1 % (w/v) BSA solution and incubate at 4 °C or room temperature for 30 minutes. Centrifuge the colloidal gold-BSA solution again for 10 minutes at 18,000X gravity to pellet the gold. Remove the supernatant and resuspend the gold pellet in a large (~ 500 μl) volume of distilled water (rinse step). Centrifuge one more time as before to pellet the gold and finally resuspend in deionized water at the desired concentration (typically 5X) for the treatment of grids or resuspend in some volume of the sample solution. Note that excess BSA will, of course, contaminate the sample. If it dries on the grid in abundance it can interfere with vitrification. Note also that even when BSA-treated, gold will precipitate in sample solutions if the solute concentration is too high. If the gold precipitates, this is immediately visible because the normally red color of the gold solution turns purple.

PROCEDURE

First phase: Preparation of gold, grids, and the sample. Timing: 30–60 min

1. Briefly vortex (~ 10 s) a tube of 10 nm colloidal gold solution. (Two concentrations of colloidal gold solution will be prepared: a lower concentration to be applied to the grids [2X-concentrated] and a higher concentration to be mixed with the sample [4 to 7X-concentrated]. Expect to use 5 μl of each concentration of gold per grid.)
2. Pipette into one tube (tube "A," for grid treatment) 10 μl of unconcentrated gold per grid.
3. Pipette into a second tube (tube "B," for sample treatment) 30 μl of unconcentrated gold per grid.
4. Centrifuge the colloidal gold solutions using a tabletop microfuge at 18,000X gravity for 10 minutes to pellet the gold. If 5 nm colloidal gold solution is used, the centrifugation duration should be extended to 25 minutes.
5. Remove the supernatants, being careful to avoid losing gold.
6. Resuspend the pellet from tube A in 5 μl filtered deionized water per grid with a pipet.
7. Glow-discharge the grids in a plasma cleaner for between 30 seconds and 2 minutes, ensuring that the carbon film of the grids is exposed to the plasma.
8. Pick up the grids with anticapillary tweezers so that the carbon face is upward.
9. Vortex the tube of 2X-concentrated colloidal gold solution (tube A) at maximum speed for ~ 3 minutes and apply 5 μl of this solution onto the carbon side of the first 2–3 grids (part of the vortexing can be done while the grids are being glow-discharged). If more

than 3 grids are to be prepared, one may briefly vortex the 2X-concentrated gold solution after treating every 2–3 grids to decrease clumping.

10. Bake the grids in a 50 °C oven (drying will take less than 10 minutes) or let them air dry (drying may take 30 minutes or more).
11. Add an appropriate amount of sample to the gold pellet in tube B (see comments on ideal sample concentrations above). As soon as the grids have dried, be ready to proceed with the vitrification.

TROUBLESHOOTING

Second Phase: Cooling the Vitrobot cup. Timing: ~ 10 min

CAUTION This step should be done in a fume hood or a well-ventilated area, as a large amount of nitrogen and some ethane is released. Liquid nitrogen, liquid ethane, and cryogen-cooled metallic tools (such as forceps or tweezers) are extremely cold: be sure to wear appropriate personal protective equipment (gloves, goggles, lab coat, and closed-toe shoes) and be careful when handling these reagents and tools.

12. Start cooling the Vitrobot cup while the grids are drying. Fill both the central ethane cup and outer nitrogen ring initially with liquid nitrogen to cool them down quickly. (The Vitrobot cup is cylindrical and consists of a central cup for liquid ethane into which the grid is plunged and a larger peripheral ring for liquid nitrogen. Between these chambers

is a gap spanned by carefully designed thermal connectors that conduct just enough heat that the ethane will first liquefy and then very slowly freeze.) Grid boxes may be placed in their holders in the outer ring at this time and cooled along with the Vitrobot cup. Keep replenishing the liquid nitrogen in the outer ring so that it is at least 75% full at all times.

13. When vigorous liquid nitrogen bubbling has ceased, begin liquefying ethane in the central cup. To do this, open the ethane tank slightly to produce just a modest flow rate directed towards the bottom or side of the cold cup wall. (If the flow rate is too low, the ethane will solidify. If the flow rate is too fast, it will not liquefy and will blow out of the chamber. Holding the tip of the ethane supply tube against the inner wall of the ethane cup facilitates condensation.)
14. Continue filling the ethane cup until it is full.
15. Wait until a thin layer of solid ethane coats the inner walls of the ethane cup to ensure that the liquid ethane is cool enough. If too much of the ethane becomes solid, melt it by blowing in more warm ethane gas.
16. When necessary, refill the ethane cup to the brim. To avoid ice contamination, make sure that the tip of the ethane supply tube is dried completely each time you introduce it into the ethane cup.

    CRITICAL: The rate of heat transfer between the ethane cup and the outer nitrogen ring is important. If the heat transfer rate is slow, it takes a longer time to liquefy the ethane. If the heat transfer rate is too fast, the ethane may solidify too quickly. For the newest Vitrobot model (Mark III) there is a metal frame that should be placed over the ethane compartment during the liquefaction process. It helps to transfer heat and liquefy the

ethane more quickly. After filling the ethane compartment with liquid ethane, the metal frame should be removed to prevent the ethane from rapidly solidifying.

Third phase: Sample vitrification. Timing: 3–5 min

17. Pick up the edge of a grid with the Vitrobot tweezers (tweezers especially constructed for the Vitrobot so that the fixed end can be attached onto the Vitrobot plunger and the pincers can be closed or opened by changing the position of a black clamp ring) and secure their grip on the grid by sliding the black clamp ring into the first notch.
18. Gently tap the tweezers on a finger to ensure that the grid does not fall off.
19. Bring the plunger in the appropriate position and mount the tweezers onto the tip of the plunger. (The Vitrobot provides two ways to apply samples to the grid. In the "manual application" mode, the sample is applied to the grid by hand with a pipetman through a side port in the blotting chamber. In the "automatic application" mode, the sample is placed in a 1.5 mL tube and secured in a holder in the blotting chamber, and the Vitrobot dips the grid into the tube before blotting. The choice of manual or automatic sample application depends on the amount of sample available. The depth to which the grid is dipped in the sample tube can be set. To use the automatic application mode, at least 50 μl of the sample must be available, but with samples smaller than even 100 μl, the grid and tweezers are sometimes damaged by hitting the tube walls near the bottom.) If the manual application mode is to be used, be sure the carbon side of the grid faces the sideport.

20. Double-check the parameters in the Console and Option screens. Different blotting parameters are needed for different samples. Our most successful parameters are summarized in Table A-1.
21. Enable the humidifier to reach 100 % humidity.
22. Wait until the blotting chamber reaches the desired temperature and humidity.
23. Refill the nitrogen and ethane chambers of the Vitrobot cup as necessary.
24. Activate the plunger to bring the grid into the blotting chamber and enable the holder housing the Vitrobot cup to move it right under the blotting chamber.
25. If the “automatic application” mode has been selected, the grid will be automatically dipped in the sample tube, blotted, and plunged in the ethane. Skip to Phase Four, Placing the grid in the storage box. Otherwise proceed with the manual application as follows.

TROUBLESHOOTING

26. Mix the sample again with a pipet or briefly vortex it.
27. Draw 3–5 μl of the combined sample and colloidal gold into the pipet, insert it through the sideport of the blotting chamber and discharge the sample onto the grid.
28. Close the entry port and wait until 100% humidity is restored in the climate chamber, if opening the port reduced the humidity.
29. Press the button to initiate grid blotting and plunging.

TROUBLESHOOTING

Notes: When using the automatic application option, we found that protein orientations in the ice were more randomly distributed and, for the same concentration of protein, the particles were more numerous in a given area than in the case of manual application. The increased range of views is important for single particle analysis. If the sample is fairly dilute and for some reason cannot be further concentrated, one way we have been able to increase the number of objects per field of view is to use the sequential application option (which was not described earlier in the interest of simplicity). This allows for the sample to be applied and blotted several times before plunge freezing. We have used at most two sequential applications.

If no sample is seen on the grids, it may be preferentially adhering to the blot paper (see Troubleshooting table). In this case, the grid can be manually blotted from its edge (rather than "face on") with a small piece of blotting paper inserted through the side port with tweezers. This minimizes the contact area while maintaining the controlled environmental conditions.

The drain time may be adjusted to 1 s to increase the likelihood of thin ice and/or to get more uniform ice (instead of the typical gradient), in cases where the increment in the blotting time (0.5 s) is insufficient to define optimal sample preparation conditions. For example, in the case of *Caulobacter crescentus* cells, 2 seconds of blotting is too long, and 1.5 seconds without drain time is too short, so we use 1.5 seconds with a 1 second

drain time. Additionally, using a drain time of 1 s or more may also avoid formation of non-vitreous ice with samples where this may be a problem.

There is an optional wait time between the application of the sample to the grid and blotting, during which time the sample solution may reach equilibrium with its environment. For some of our protein complexes, a 15–30 second wait time resulted in grids with more randomly distributed and numerous particles in a given area than 0 seconds waiting. In the case of some of our viral samples, a 15 second wait time increased the number of viral particles present. Presumably this is because some samples adhere to the grid in time and remain throughout the blotting process.

Fourth phase: Placing the grid in the storage box. Timing: 1–2 min

30. Slide the Vitrobot tweezers off the tip of the plunger while keeping the grid submerged within the liquid ethane.
31. Support the tweezers on the edge of the ethane cup, again keeping the grid completely immersed in liquid ethane, and stabilize your hand against the side of the Vitrobot cup.
32. Using both hands, move the cryogen cup from the Vitrobot to the bench so that there is more room to maneuver the grid and tweezers.
33. In one swift motion transfer the grid from the ethane to the liquid nitrogen ring.

    Alternatively, with the latest model of the Vitrobot (Mark III), the transfer of the tweezers from the ethane cup to the liquid nitrogen ring can be done automatically. Before doing this, fill the nitrogen reservoir again after its descent and before activating the movement.

34. Slide the black clamp ring off the tweezers while keeping them pinched closed with your fingers.
35. Gently move the tweezers close to the grid box and place the grid in the desired slot.

TROUBLESHOOTING

Fifth phase: Iterations. Timing: 4–6 min per grid

36. Before proceeding with the next grid, if there is any condensation on the outside bottom part of the climate chamber resulting from the contact of the chamber with the cold Vitrobot cup, wipe it off with a paper towel and/or warm it with a heat gun.
37. Dry the Vitrobot tweezers with a Kim wipe.
38. Repeat steps 17–37 for each new grid.

Sixth phase: Sample storage. Timing: 2–3 min

39. When all the grids have been frozen and placed in the grid boxes, cool the grid box lids in liquid nitrogen and secure them on top of the grid boxes. (If the lids are fastened by screws, pre-cool the screwdriver before touching it to the grid boxes.)
40. Cool a pair of forceps or long tweezers in liquid nitrogen and use them to move the grid box into a liquid-nitrogen-filled transfer dewar.
41. Store the grid box under liquid nitrogen until ready for observation.

PAUSE POINT: If the grids will not be used immediately, the grid box can be stored essentially indefinitely in a 50 ml screw-cap conical tube. We typically punch two holes on opposite sides of the tube, approximately 1 cm below the bottom thread, and loop an ~ 4 ft long labeled nylon or polyester string through the holes. We then fill the 50 ml tube with liquid nitrogen, drop the grid storage boxes into it, and place the tube in a cane which is finally lowered into a large nitrogen cryostorage dewar with the labeled string hanging out of the top.

TIMING

Steps 1–11 (Preparation of gold, grids, and the sample) take 30–60 minutes depending on which method is used to dry the gold solution onto the grids. Steps 12–16 (Cooling the Vitrobot cup) take about 10 minutes. Steps 17–29 (Sample vitrification) take 3–5 minutes. Steps 30-35 (Placing the grid in the storage box) take 1–2 minutes. Steps 36–38 (Iterations) take 4–6 minutes per grid. Finally, steps 39–41 (Sample storage) take 2–3 minutes.

ANTICIPATED RESULTS

This protocol typically produces plunge-frozen electron cryomicroscopy grids with suitably thick ice covering most of the grid (~ 70% or more) and a uniform gold distribution (see Fig. A-1 for an example). The preparation of 8 grids takes less than 2 hours and most of these grids are suitable for single- or dual-tilt tomography data collection.

References

Adrian, M., Dubochet, J., Lepault, J., and McDowall, A.W. (1984) Cryo-electron microscopy of viruses. *Nature* **308**: 32-36.

Adrian, M., ten Heggeler-Bordier, B., Wahli, W., Stasiak, A.Z., Stasiak, A., and Dubochet, J. (1990) Direct visualization of supercoiled DNA molecules in solution. *Embo J* **9**: 4551-4554.

Angell, C.A. (2004) Amorphous water. *Annu Rev Phys Chem* **55**: 559-583.

Benjamin, J., Ganser-Pornillos, B.K., Tivol, W.F., Sundquist, W.I., and Jensen, G.J. (2005) Three-dimensional structure of HIV-1 virus-like particles by electron cryotomography. *J Mol Biol* **346**: 577-588.

Briegel, A., Dias, D.P., Li, Z., Jensen, R.B., Frangakis, A.S., and Jensen, G.J. (2006) Multiple large filament bundles observed in Caulobacter crescentus by electron cryotomography. *Mol Microbiol* **62**: 5-14.

Dubochet, J., and McDowall, A.W. (1981) Vitrification of pure water for electron microscopy. *J. Microsc.* **124**: RP3-4.

Frederik, P.M., and Hubert, D.H. (2005) Cryoelectron microscopy of liposomes. *Methods Enzymol* **391**: 431-448.

Henderson, G.P., and Jensen, G.J. (2006) Three-dimensional structure of Mycoplasma pneumoniae's attachment organelle and a model for its role in gliding motility. *Mol Microbiol* **60**: 376-385.

Iancu, C.V., Wright, E.R., Benjamin, J., Tivol, W.F., Dias, D.P., Murphy, G.E., Morrison, R.C., Heymann, J.B., and Jensen, G.J. (2005) A "flip-flop" rotation stage for routine dual-axis electron cryotomography. *J Struct Biol* **151**: 288-297.

Iancu, C.V., Wright, E.R., Heymann, J.B., and Jensen, G.J. (2006) A comparison of liquid nitrogen and liquid helium as cryogens for electron cryotomography. *J Struct Biol* **153**: 231-240.

Komeili, A., Li, Z., Newman, D.K., and Jensen, G.J. (2006) Magnetosomes are cell membrane invaginations organized by the actin-like protein MamK. *Science* **311**: 242-245.

Lepault, J., Booy, F.P., and Dubochet, J. (1983) Electron microscopy of frozen biological suspensions. *J Microsc* **129**: 89-102.

Li, H., DeRosier, D.J., Nicholson, W.V., Nogales, E., and Downing, K.H. (2002) Microtubule structure at 8 A resolution. *Structure* **10**: 1317-1328.

Lucic, V., Forster, F., and Baumeister, W. (2005) Structural studies by electron tomography: from cells to molecules. *Annu Rev Biochem* **74**: 833-865.

Murphy, G.E., and Jensen, G.J. (2005) Electron cryotomography of the E. coli pyruvate and 2-oxoglutarate dehydrogenase complexes. *Structure* **13**: 1765-1773.

Murphy, G.E., Leadbetter, J.R., and Jensen, G.J. (2006) In situ structure of the complete Treponema primitia flagellar motor. *Nature* **442**: 1062-1064.

Nickell, S., Kofler, C., Leis, A.P., and Baumeister, W. (2006) A visual approach to proteomics. *Nat Rev Mol Cell Biol* **7**: 225-230.

Wright, E.R., Iancu, C.V., Tivol, W.F., and Jensen, G.J. (2006) Observations on the behavior of vitreous ice at approximately 82 and approximately 12 K. *J Struct Biol* **153**: 241-252.

Figures and Tables

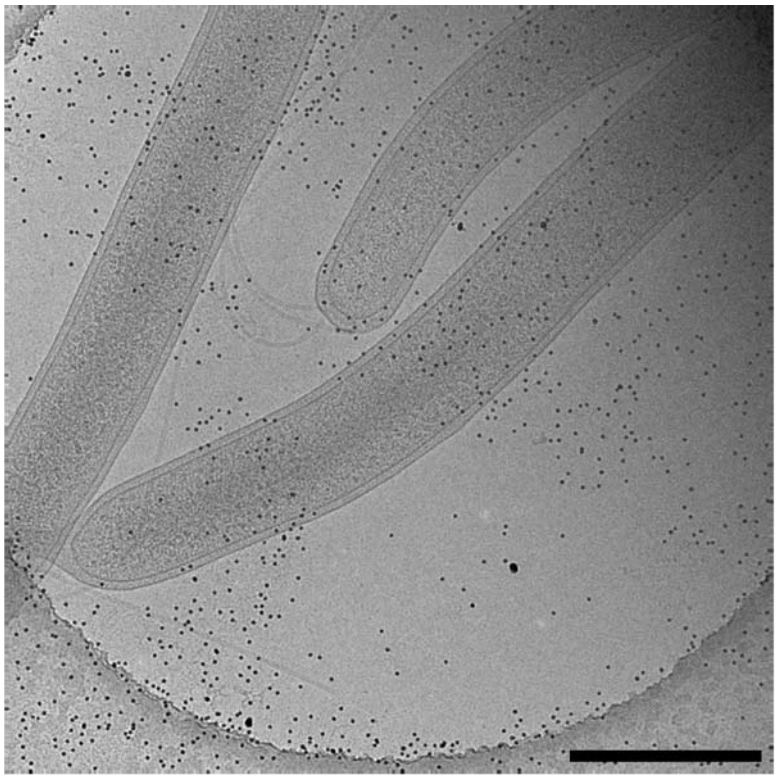

Figure A-1. Example image showing well-preserved bacterial cells, a good distribution of gold fiducials, and thin ice. Energy filtered (20 eV slit) image collected on a 300 kV FEG "G2 Polara" TEM (FEI Company), using a 2048 x 2048 GIF CCD (Gatan, UK), and a pixel size of 0.98 nm. Scale bar is 500 nm

Sample	Blot time (s)	Blot offset (mm)
Large protein complexes	3-4	2-3
Viruses	2-3 + drain time 0.5-1 s	2
Organelles	1-2	1-2
Cells	1-2 + drain time 1 s	1-2

Table A-1. Vitrobot blotting parameters for different samples. "Blot time" is the period that the blot pads are pressed against the sample. "Blot offset" describes the position of the grid between the blot pads and partially controls the pressure exerted by the blotting paper on the grid. Larger absolute values of the blot offset produce a steeper ice thickness gradient on the grid. Blot offset values in the table are negative numbers. "Drain time" is the delay between blotting and plunging.

Table A-2. Troubleshooting.

Problem	*Possible reason*	*Solution*
Steps 1-11. Non-uniform dispersion of colloidal gold (associated with massive aggregation of gold particles)	The buffer is potassium phosphate or has high concentrations of salt or other additives promoting the aggregation of gold. If the gold solution changes color (like from pink or red to purple), this indicates it has precipitated.	Try to minimize salts and additives. Otherwise, apply gold only on the grids, avoid combining gold with the sample, or treat the gold with BSA.
Steps 12-35. Formation of non-vitreous ice on the grids	Humidity in the climate chamber may not have reached 100% in the blotting chamber.	Double-check that the humidity sensor is working properly.
	The transfer of the grid from the ethane cup to the liquid nitrogen ring was too slow.	Accelerate the transfer. If the Vitrobot Mark III model is available, use the automatic transfer option.
	The ethane may not have been cold enough.	Check that there is a thin film of solid ethane on the sides of the cup at all times and that the liquid nitrogen level is maintained throughout the freezing session.
Steps 25 or 29. Damaged grids (some of the carbon film gets stuck on the blotting paper)	The blotting pressure is too high.	Reconsider the blotting offset or ensure that the blotting pads function properly. The springs of the blotting pads may need to be adjusted or replaced.
	If, after the blotting, the wet spots on the blotting paper are significantly different in size for the two pads, the blotting mechanism is probably not centered correctly with respect to the plunger.	Recenter the blotting mechanism relative to the plunger.
Steps 25 or 29. No sample is visible on the grid	The sample is sticking to the filter paper.	Blot manually from the edge of the grid.